Dissertation
submitted to the
Combined Faculty of Mathematics, Engineering and Natural Sciences
of Heidelberg University, Germany
for the degree of
Doctor of Natural Sciences

Put forward by
Vimal, Vijayan
born in: Kuniyamuthur, Tamilnadu, India
Oral examination: 07.02.2024

Systematic study of binary neutron star mergers with neutrinos and pions

Referees: Priv.-Doz. Dr. Andreas Bauswein
Prof. Dr. Cornelis P. Dullemond

Zusammenfassung

Im ersten Teil der Arbeit führen wir eine relativistische hydrodynamische Simulation einer 1,35-1,35$M_\odot$ Doppelneutronenstern-Verschmelzung (DNS-Verschmelzung) mit Neutrinos durch. Wir untersuchen den dynamische Massenauswurf sowie die Eigenschaften der ungebundenen Materie und führen Nukleosynthese-Rechnungen durch. Anschließend diskutieren wir eine systematische Studie von DNS-Verschmelzungen mit verschiedenen Zustandsgleichungen (EOS) und Neutronensternmassen. Bei einer gegebenen Gesamtmasse beobachten wir für asymmetrisch Systeme mit ungleichen Neutronensternmassen eine systematische Abnahme der dominanten Oszillationsfrequenzen des Gravitationswellensignals. Zusätzlich erzeugen diese asymmetrischen Verschmelzungen höhere Temperaturen, Elektronenanteile und Neutrino-Leuchtkräfte in ihren Verschmelzungsüberresten. Die Simulationen zeigen insgesamt eine Zunahme der ungebundenen Masse, der Durchschnittstemperaturen und eine sphärischere Verteilung des Auswurfs. Trotz höhrer Temperaturen des ungebundenen Materials ist dieses bei asymmetrischen Verschmelzungen neutronenreicher als bei symmetrischen Verschmelzungen. Insbesondere wird bei asymmetrischen Verschmelzungen mehr Material bei größeren Radiien ausgestoßen, die weniger Neutrino-Bestrahlung erfahren.

Im zweiten Teil der Arbeit untersuchen wir die Auswirkungen von Pionen auf Simulationen von Neutronenstern-Verschmelzungen und Gravitationswellen. Im Vergleich zu Modellen ohne Pionen beobachten wir Veränderungen in den Eigenschaften nicht-rotierender Neutronensterne, wie eine Reduzierung der maximalen Masse, des Radius und der “tidal deformability”. Simulationen mit Pionen zeigen eine erhöhte Gravitationswellenfrequenz nach der Verschmelzung und eine reduzierte kritische Masse für die prompte Bildung eines Schwarzen Lochs. Empirische Beziehungen zwischen dieser Schwelle oder der Gravitationswellenfrequenz und stellaren Parametern bleiben nahezu unbeeinflusst. Die Einbeziehung von Pionen führt zudem zu einer moderaten Erhöhung der ungebundenen Materie bei Neutronenstern-Verschmelzungen.

Abstract

In the first part of the thesis, we perform a relativistic hydrodynamical simulation of a 1.35-1.35$M_\odot$ binary neutron star (BNS) merger with neutrinos and investigate in detail dynamical mass ejection, ejecta properties and the associated nucleosynthesis calculations. We conduct a systematic study of BNS merger simulations considering different equations of state (EOSs), different total masses, and mass ratios. For a given total mass, comparing the dynamics of postmerger evolution, we observe a systematic decrease in the dominant oscillation frequencies and a relatively quick approximate plateau of maximum densities in the remnants of asymmetric mergers. Additionally, these asymmetric mergers produce higher temperatures, higher average electron fractions, and higher neutrino luminosities in their remnants. Considering ejecta properties, we notice an overall increase in the ejecta mass, the average ejecta temperatures, and a more spherical distribution of the ejecta mass per angular bin. Despite the higher ejecta temperatures, the neutron-richness of the dynamically ejected material from asymmetric mergers is relatively higher than that of symmetric mergers. Specifically, asymmetric mergers are found to produce a larger amount of material ejected from a larger radii of the central remnant that undergo less neutrino irradiation.

In the second part of the thesis, we investigate the impact of pions on simulations of neutron star mergers and explore their effects on gravitational wave observables. Compared to models without pions, we observe changes in the properties of cold, non-rotating neutron stars, including reductions in maximum mass, radius, and tidal deformability. From simulations with pions, we find an increase in the dominant post-merger gravitational wave frequency and a reduction of the threshold binary mass for prompt black hole formation. We find empirical relations that correlate the threshold mass or the dominant post-merger gravitational wave frequency to the stellar parameters of nonrotating neutron stars are found to remain valid to good accuracy. Additionally, we also address the mass ejection by neutron star mergers and observe a moderate enhancement of the ejecta mass by the inclusion of pions.

To Aravind, Jacob and Selva

Nomenclature

List of acronyms

BNS	binary neutron star
NS	neutron star
BH	black hole
GW	gravitational wave
EOS	equation of state
sGRB	short gamma-ray burst
TOV	Tolman–Oppenheimer–Volkoff
3D	three-dimensional
SPH	smoothed particle hydrodynamics
RK	Runge-Kutta
CFC	conformal flatness condition
ADM	Arnowitt-Deser-Misner
ILEAS	improved leakage-equilibration-absorption scheme
HMNS	hyper massive neutron star

List of constants

c	speed of light
G	gravitational constant
$M_\odot$	solar mass

Contents

1. Introduction

"Where do all the heavy elements in the universe from iron to uranium come from?", one of the long-standing questions in physics with its most evident candidate, binary neutron star (BNS) mergers, unambiguously detected for the first time in 2017. This question about the origin of heavy elements is the main motivation for our study.

Neutron stars (NSs) are the final remnant product of the collapsed core of a massive star formed in a core-collapse supernova explosion when it does not undergo a collapse into a black hole (BH). They are one of the most compact objects found in the universe, with a typical mass of 1-2 $M_\odot$ and a radius of about 10-15 km [277]. As a result, it gives rise to densities in the core that can exceed several times the nuclear saturation density ($\rho_{\rm sat} \sim 2.7 \times 10^{14}\, g/cm^3$). These extreme conditions make NSs one of the best tools to probe the physics of high-density matter, for which several efforts are being made to study these properties in a laboratory, e.g. GSI-FAIR [90, 250, 73].

A BNS system consists of two neutron stars that long orbit each other for millions of years (inspiral phase). These binaries radiate away energy and angular momentum in the form of gravitational waves (GWs), shrinking their orbit, and eventually merge within a timescale of a few milliseconds (merger phase). The structure, composition, and properties of NS matter at high densities are governed by the so-called equation of state (EOS) [140] which is not precisely known since the fundamental constituents of high-density matter and their interactions are not known. The EOS determines the outcome and observables of a BNS merger. Depending on the EOS, the remnant of the merger can either promptly collapse into a BH or become a massive differentially rotating NS [78, 21, 160, 255, 214, 252, 29, 39, 177, 206, 116, 234].

The ejecta material expelled from the collision generally has a very complex structure and mass ejection occurs through different channels over various timescales. "Dynamical" ejecta are defined as the material that is ejected on dynamical timescales of tens of milliseconds from tidal interactions and shock heating exerted on the NSs. These typically consist of a mass range within 10^{-4}–$10^{-2} M_\odot$ and ejecta velocities within 0.2c–0.3c [230, 239, 193, 134, 24, 109, 217, 16, 55]. "Secular" ejecta are the material which gets unbounded on longer timescales of about tens of milliseconds to few seconds (mainly from the disk surrounding the central remnant) through different outflow components such as magnetically driven, neutrino driven, and viscously driven. They typically consist of more massive

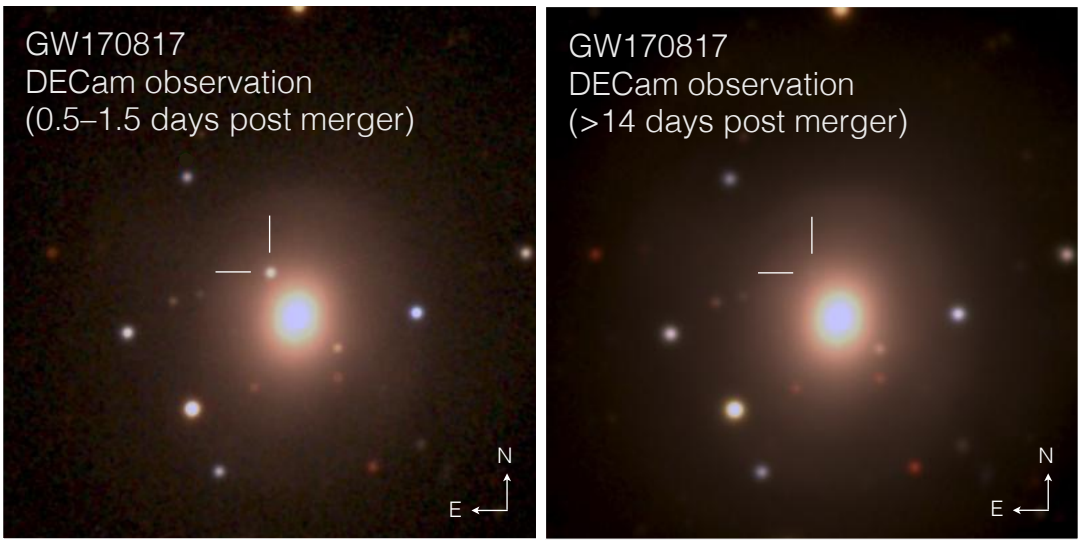

Figure 1.1: The time evolution of the GW170817 discovered on August 18, 2017 in NGC4993. The following are the detection images within the first 0.5-1.5 days after the merger (left column) and 14 days after the merger (right column). Credit: The image was taken from [261].

ejecta with a mass range of 10^{-2}–$10^{-1}M_{\odot}$ and lower velocities $\lesssim$ 0.2c [77, 205, 118, 91, 256, 122]. Each of these ejecta components creates favourable conditions for the rapid neutron capture process (r-process) [49, 51, 138, 139, 260, 60], which is responsible for the formation of approximately half of all heavy nuclei in the universe, from [55, 277].

1.1. Observational evidence and insights

On 17 August 2017, the first unambiguous multi-messenger detection of a BNS merger took place, dubbed GW170817 [4, 1, 6]. The source was found to be comprised of two neutron stars with masses of approximately $1.35M_{\odot}$ and the merger occurring at a distance of approximately 40 Mpc from Earth [52]. A weak short gamma-ray burst (sGRB) was detected 1.74 seconds after the GW signal was measured, along with additional X-ray and radio signals [3, 98, 241, 174, 273, 102, 103, 155]. Within 11 hours after the GW trigger, an associated electromagnetic transient, known as the kilonova [146, 158] AT2017gfo was detected across a broad range of the electromagnetic spectrum, including ultraviolet, optical and infrared emissions [14, 261, 59, 185, 126, 258, 279, 178], all from the same location in the sky. The location in the sky where the event occurred was identified as close to the galaxy NGC4993. An image showing the evolution of the kilonova by comparing the images within the first 0.5-1.5 days after the merger and 14 days after the merger is shown in Fig. 1.1, where a bright spot is seen near the marked position and is seen to fade away within a timescale of two weeks. The observed spectrum showed a peak emission shift from blue to red on this timescale.

On 25 April 2019, a second signal was detected (as a single detector event),

likely emitted during the merger of two binary neutron stars, dubbed GW190425 [7]. But, compared to GW170817, this event was much weaker due to its larger distance (approximately greater than 100 Mpc) and no kilonova was found in the aftermath from optical and infrared surveys [58].

Several insights were obtained from the observations mentioned above: The GW signal and the subsequent electromagnetic counterparts carry information about the cold properties of neutron stars (e.g. masses of NSs, radii of NSs, etc.) involved in the merger [5, 6, 35, 251, 154, 76, 218, 240, 222, 130, 215]. In addition to EOS constraints, the gravitational and electromagnetic data are also used to determine the Hubble constant [2]. The discovery of sGRB confirms the idea that BNS systems could be the source of sGRBs, which had been previously suggested but not proven [74, 181, 176, 38]. The rapidly evolving emission in the optical and infrared is in very good agreement with an expanding ejecta cloud (with a mass of about a few $0.01 M_{\odot}$) undergoing the r-process, where the radioactive decays of the r-process heat the ejecta producing quasi-thermal radiation. The detailed properties and evolution of the light curve thus provide very strong evidence that heavy elements were created in the ejecta of this NS merger [124, 265, 61, 267, 72, 162, 159]. The spectrum of the kilonova which was later found to exhibit broad absorption features, one of them being associated with strontium [282]. Strontium is an element produced through the r-process, offering compelling evidence that this nucleosynthesis process occurred in the ejecta of GW170817. Considering the estimated merger rates and the estimated ejecta mass of GW170817, it appears that BNS mergers likely are one of the major sources of heavy element production in the Universe. So far, they are the only confirmed astrophysical sites to date where r-process nucleosynthesis takes place [60, 116], from [277].

Despite the insights obtained from these events, models still encounter difficulties in explaining certain aspects and details of the associated kilonova [283, 54, 120]. The combination of theoretical modelling, nuclear experiments, GW detections, and electromagnetic observations continues to give more insights on the nature of neutron stars and our understanding of the EOS of nuclear matter at extreme densities. In this chapter, we describe the basics of the r-process nucleosynthesis, kilonova, importance of neutrinos and EOS closely following the cited works [116, 252, 97, 96, 17, 16, 277, 278].

1.2. R-process nucleosynthesis

In dense neutron-rich conditions, where the neutron densities ($n_{\rm n}$) are greater than about $10^{20}\,{\rm cm}^{-3}$, i.e. $n_{\rm n} > 10^{20}\,{\rm cm}^{-3}$, and the neutron capture timescales ($\tau_{\rm n}$) are shorter than the β-decay timescales (τ_{β}), i.e. $\tau_{\rm n} << \tau_{\beta}$, the ejecta can synthesise heavy elements beyond iron through rapid neutron captures [49, 51, 138, 139, 260, 60, 116].

When the ejecta material expelled from the merger expands and the temperature drops below 1 MeV (10^{10}K), protons and neutrons combine to form the initial seed nuclei. The lack of Coulomb repulsion and the abundance of neutrons make neutron captures the dominant channel. Through a series of neutron captures, the

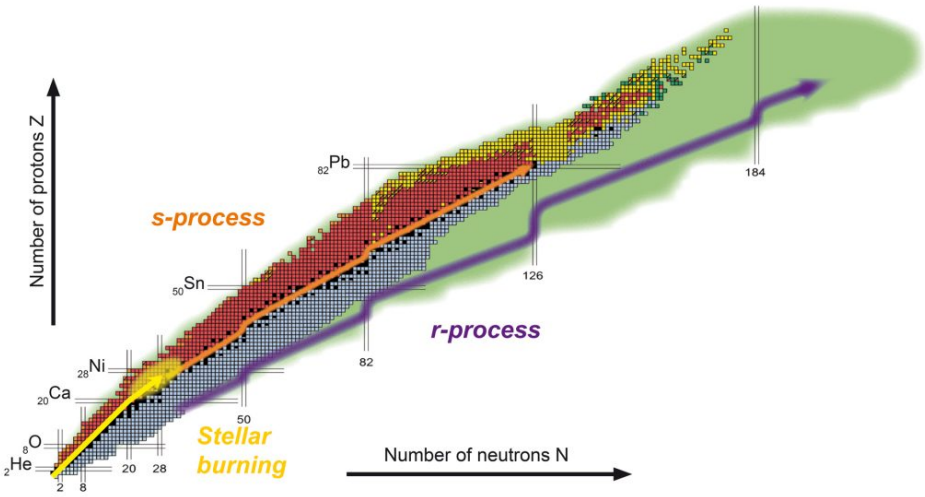

Figure 1.2: Nuclear chart showing different nucleosynthesis processes.,The stellar burning path is shown in yellow colour and the so called s-process [260] path is shown in orange colour. The topic of our interest for this study, the r-process, is shown in violet colour. credit: EMMI, GSI.

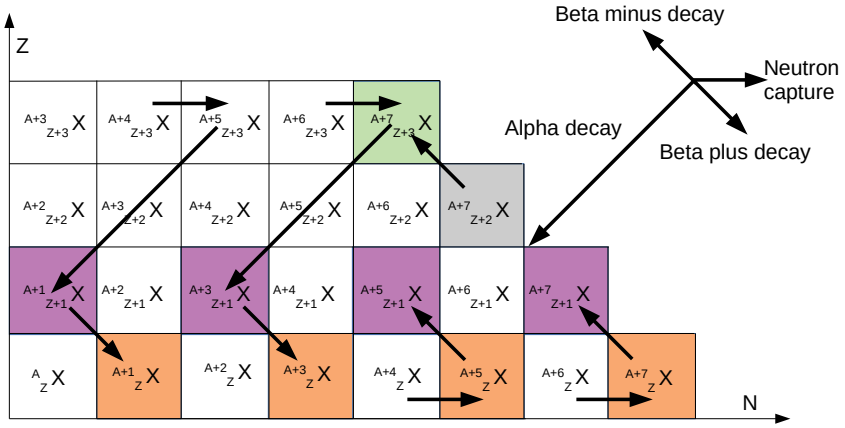

Figure 1.3: Visualisation of the radioactive beta decay, alpha decay and neutron capture channels in a sample region of the nuclear chart.

seed nuclei can move away from the valley of stability and reach to the far right of the nuclear chart (see Fig. 1.2), resulting in the production of neutron-rich heavy nuclei. This process leads to the creation of elements that are far from stability in highly radioactive and neutron-rich areas. The abundance of these elements is determined by the balance between photodisintegration and neutron captures, which are in a state of chemical equilibrium. Nevertheless, even though the environment is neutron-rich, these nuclei cannot become excessively neutron-rich because the neutron capture process cannot take place when the nuclei reach a certain point called the "neutron drip line" beyond which the nuclei cannot exist.

The nuclei located near the neutron drip line are extremely unstable and decay through β^- emission, causing the nuclei to move away from the drip line. However, moving away from the neutron drip line allows neutron captures to take place again, returning the nucleus to the drip. As long as there is a sufficient number of neutrons available for recurring captures, the seed nuclei will progress along the neutron drip line and continue to achieve a higher mass number through a series of neutron captures and β^--decays.

As the density decreases and the neutrons have been used up (which happens after about a second and indicates the end of the r-process), the rate of neutron captures decreases. At this stage, β-decay becomes the dominant decay channel and the collection of all nuclei that had been produced along the neutron drip line decays through β-decay, α-decay, and fission channels, to the valley of stability. Refer to Figs. 1.2 and 1.3, for a visualisation of the r-process in the nuclear chart, and radioactive β-decay, α-decay, and neutron capture channels in a sample region of the nuclear chart.

Taking into account the large number of nuclei moving along this r-process path, the seed nuclei will pass through points with closed neutron shells (magic numbers) which are comparatively more stable. As a result, the reaction rates slow down at these points, leading to accumulation, which causes an increase in the abundance of these nuclei. As a result, these points are carried along the r-process path, and the final abundance of elements shows an imprint of these nuclei with closed neutron-shells. The points at which these accumulations occur are approximately at A = 80, A = 130 and A = 195 with the corresponding peaks in the abundance distribution, commonly known as the first, second, and third r-process peak (see Fig. 3.4). Approaching the valley of stability, the nuclear half-lives progressively extend, resulting in a freeze-out that happens over a wide range of timescales and includes the abundances obtained from extremely long-lived nuclei that take billions of years to complete, adapted from [116, 60].

Some of the key quantities that characterise r-process nucleosynthesis are entropy, expansion timescale, and Y_e of the ejecta [211, 15, 150]. Among these, Y_e, i.e. the electron fraction, which determines the neutron richness or the neutron to seed ratio is one of the crucial parameters in BNS mergers. Y_e is defined as the ratio of the number of charged leptons to the total number of baryons, i.e. $Y_\mathrm{e} = (n_\mathrm{e}^- - n_\mathrm{e}^+)/n_B$, where $n_{e^\pm}$ are the number densities of electrons and positrons, n_B is the baryon number density [121].

Numerical simulations with detailed nuclear network calculations [100, 134, 281, 150] demonstrates that elements of the r-process with a mass number greater

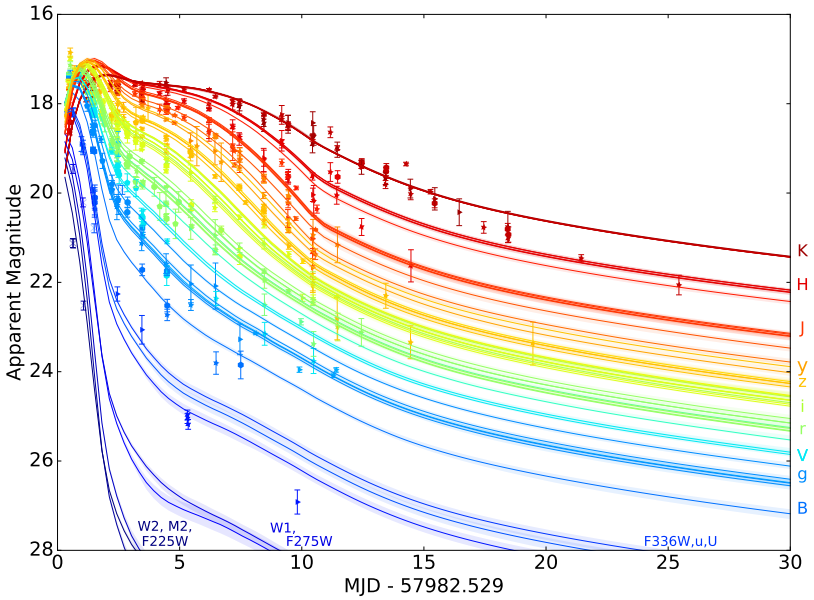

Figure 1.4: UVOIR (ultraviolet-optical-infrared) light curves of kilonova AT2017gfo obtained from the combined datasets from various sources listed in [279]. Credit: Image taken from [279].

than 120, such as the second and third r-process peak elements, are robustly produced for neutron-rich ejecta with $Y_e \leq 0.1$. Under these conditions, the production of lighter r-process elements is found to be significantly reduced. Whereas, it is also observed that for ejecta with $Y_e \geq 0.25$, heavy elements, such as lanthanides, are not widely produced when there is not enough neutron abundance [252]. BNS merger, owing to the wider range of Y_e values in its ejecta components, from its original cold β-equilibrium values to 0.5 and above, hosts ideal conditions for the production of elements in a wider mass range of the nuclear chart (see Fig. 4.7 for a typical range of cold β-equilibrium values of Y_e involved in the mergers).

1.3. Electromagnetic transient (kilonova)

The primary mechanism that powers a kilonova is the radioactive decay of elements freshly produced in the merger ejecta through the r-process nucleosynthesis. As discussed in the previous section, the neutron-rich, unstable nuclei produced from r-process generally decay and reach stability within a few seconds through a combination of β-decay, α-decay (as shown in Fig. 1.3) and fission. These decays release significant amounts of energy in the form of high-energy charged particles, including electrons, photons, α particles, and fission products. The produced particles further transfer their kinetic energy into thermal energy within the merger ejecta and result in an electromagnetic emission [252, 60, 116]. In particular, the specific heating rates of β-decay and γ-ray emission are one of the dominant heating sources of kilonovae. The β-decay channel generally loses energy in terms of β-particles and neutrinos, and is primarily accompanied by γ-ray emission. The

decay channels such as α decay and fission also contribute to the heating, but they depend sensitively on the amount of heavier nuclei produced. When considering together all decay channels, it becomes apparent that r-process heating involves various decay channels occurring across different timescales. The combination involves numerous exponential decays with varying half-lives, leading to an overall power-law decay [284, 158, 134, 116, 252]. This power-law heating from r-process elements is also found to be consistent with the observations of AT2017gfo.

We note that in addition to radioactive decay, both the thermalisation efficiency and the atomic opacities play an essential role in determining the light curves and spectra of kilonovae. In the early hours following the merger, the density of the ejecta is so high that a large portion of the expanding outflow is optically thick, and the radiation escapes only from the outer layers. During expansion, the density decreases and eventually the optical depth becomes thin enough for a large part of the outflow to become optically transparent [116]. This transition from an initial opaque state to a transparent one essentially depends on the opacity of the material, which gives a measure of photons interacting with matter. Primarily, absorption through bound-bound transitions of heavy elements affects opacity, and, in particular, open f-shell elements, such as lanthanides and actinides, have a large number of excited levels with low excitation energy, leading to a large number of transition lines in the optical and infrared ranges [252]. From atomic structure calculations, the mean opacity of lanthanide rich ejecta is approximately 10 $\mathrm{cm}^2\ \mathrm{g}^{-1}$ and above, compared to 0.1 $\mathrm{cm}^2\ \mathrm{g}^{-1}$ for lanthanide-free ejecta [252, 23, 266, 123]. Inferring from these results, depending on the presence of lanthanides/actinides, low opacities are produced in the early emission (lanthanide-free) from hot material, and light is emitted at shorter wavelengths (blue colour). Higher opacities are produced in the late emission (lanthanide-rich) from colder material, and light is emitted at longer wavelengths (red colour). Fig. 1.4 shows the evolution of the light curve from blue to red across different electromagnetic spectra, taken from [279].

In conclusion, it is evident that the ejecta mass, the ejecta velocity, the Y_e distribution of the ejected material and the abundance of heavy elements produced by the r-process are the primary determinants of the properties of the kilonovae. One of the fundamental tasks of BNS merger modelling involves the accurate prediction of these properties through reliable, self-consistent models and a comprehensive understanding of the underlying physics [97].

1.4. Neutrinos

A key parameter in determining the abundance of elements synthesised by r-process nucleosynthesis and to quantify the amount of neutrons present in the system is the electron fraction Y_e. In neutron star mergers, we start with an initial configuration that corresponds to a cold neutron-rich neutron star (see Fig. 4.7). During the merger, the remnant heats up to large temperatures, leading to weak interactions producing neutrinos in copious amounts. These neutrinos interact with free protons and free neutrons to change a significant amount of the com-

position of the ejecta. In particular, high temperatures favour the production of numerous electron-positron pairs and lead to positron captures on neutrons, which increase Y_e towards new equilibrium values [277, 60, 252]. The most important of them are beta reactions,

$$\nu_e + n \leftrightarrow p + e^-, \tag{1.1}$$
$$\bar{\nu}_e + p \leftrightarrow n + e^+. \tag{1.2}$$

Neutrino Schemes

All these considerations exemplify the importance of including neutrino-matter interactions in hydrodynamical merger simulations. Properly accounting for neutrino-matter interactions in neutron star mergers remains a difficult problem, since the evolution of the neutrino phase-space distribution function for each neutrino species is governed by the Boltzmann transport equation, which involves a six-dimensional (three spatial and three momentum directions) time-dependent problem [147], from [17]. As a result, historically, various approximations and schemes have been developed to deal with the neutrino transport in numerical simulations. These can be broadly classified into three groups: Monte-Carlo methods, moment schemes, and leakage methods (see [16, 17, 96, 97] for more details and [85] for a review on different schemes).

Monte-Carlo methods: The fundamental concept underlying Monte-Carlo methods for radiation transport involves discretising the neutrino distribution function through the utilisation of the so called Monte-Carlo packets, where each of these packets represents a substantial amount of neutrinos [85]. Although Monte-Carlo methods serve as a viable approach to solving the Boltzmann equation and offer an accurate solution to the neutrino transport, they intrinsically produce sampling noise, which vanishes only in the case where the number of packets used in the simulation becomes infinite. The requirement of a large number of packets to maintain this noise at a minimum level makes them computationally more expensive [96]. There exist a few Monte-Carlo methods in literature used in the study of core-collapse supernovae [112, 113, 114, 128, 8] and BNS mergers [224, 84, 87].

Moment schemes: A moment scheme is an approximation to the full Boltzmann neutrino transport where the angular dependence in the equation is removed by the well-defined moments of the neutrino distribution function, and only these moments are evolved in time [147, 268, 48, 47, 163, 253]. The first n moment equations contain all moments through order $n+1$. In order to achieve an approximate solution, it is necessary to truncate the series of moments at a specific order. This truncation requires a closure relation that typically expresses the highest employed moment as a function of all preceding moments in the form of an analytical relation [145, 169, 259, 210]. The commonly used M1 scheme represents a multi-dimensional, energy-dependent (spectral) approach where the truncation is done after the first-order in which only the zeroth and first moments are evolved [96]. These moments correspond to the neutrino energy density and the energy flux density. The M1 scheme has been extensively used in many applications, including simulations of core-collapse supernovae [188, 192, 191, 187, 257, 202, 50, 189],

in simulations of BNS mergers, with an energy-dependent form where the neutrino energy space is discretised into energy bins with approximate logarithmic intervals between 0 and 400 MeV [121], or in a gray form where the energy dependence is eliminated by integrating the quantities over all energy bin values in the evolution equations [89, 84]. Despite their widespread use in characterising neutrino transport, M1 schemes can become computationally expensive, particularly when considering energy dependence. Furthermore, inherent approximations and the use of closure relations in M1 schemes prevent them from converging to the exact solution of the Boltzmann equations, even in the case of infinite resolution [85].

Leakage schemes: Leakage schemes are some of the simplest and widely used approximations for addressing neutrino effects. The basic idea of leakage schemes involves solving the local effective rates for neutrino number and energy through local source terms integrated into the hydrodynamical equations, based on whether neutrinos are completely trapped or free streaming, which is determined by optically thick and thin conditions [16, 17]. This approach follows the original implementations described in [236] and [229], used in Newtonian merger models [236, 237, 238, 239, 229, 235, 134, 228, 231], in relativistic BNS merger simulations [245, 244, 131, 66, 86, 83, 184, 201, 142, 144, 42], where, in some cases, the fundamental functionality is enhanced through the incorporation of hybrid treatments. These hybrid methods combine the features of both the leakage and moment schemes depending on different neutrino conditions [246, 247, 248, 93, 251, 137, 216, 212, 213, 218, 288]. Taking into account the energy dependence of neutrino transport, there also exists an advanced spectral leakage scheme [205, 204, 96, 97] employed for computationally efficient, multidimensional hydrodynamic simulations. In this study, we exclusively use an advanced leakage treatment with leakage, equilibration and absorption (ILEAS), from [16]. A detailed discussion on the different components of ILEAS with further improvements will be presented in Sec. 2.2.

1.5. EOS on merger dynamics and NS structure

Merger dynamics: The EOS for high-density matter plays a crucial role in determining the structure of NSs and influencing the dynamics, the evolution, and the observable properties of BNS mergers along with their outcomes. The GW signal emitted from BNS merger reflects the dynamical evolution and carries an imprint of the EOS. In merger remnants that do not collapse into a BH, this signal can last for several tens of milliseconds before it diminishes from dampening effects. During this period, the GW emission from the BNS merger remnant is dominated by a primary oscillation mode of the central remnant, with a single distinct frequency, $f_{\rm peak}$. Extensive studies of various BNS merger simulations employing different EOSs have shown that this dominant oscillation mode $f_{\rm peak}$ is closely related to the radius and fundamental cold properties of the NS [27, 26, 108, 30, 264, 41, 29, 223, 143, 46, 274, 43, 280]. Despite the low sensitivity of current detectors within this frequency range, a measurement of $f_{\rm peak}$ can provide a number of significant constraints on the EOS for high-density matter.

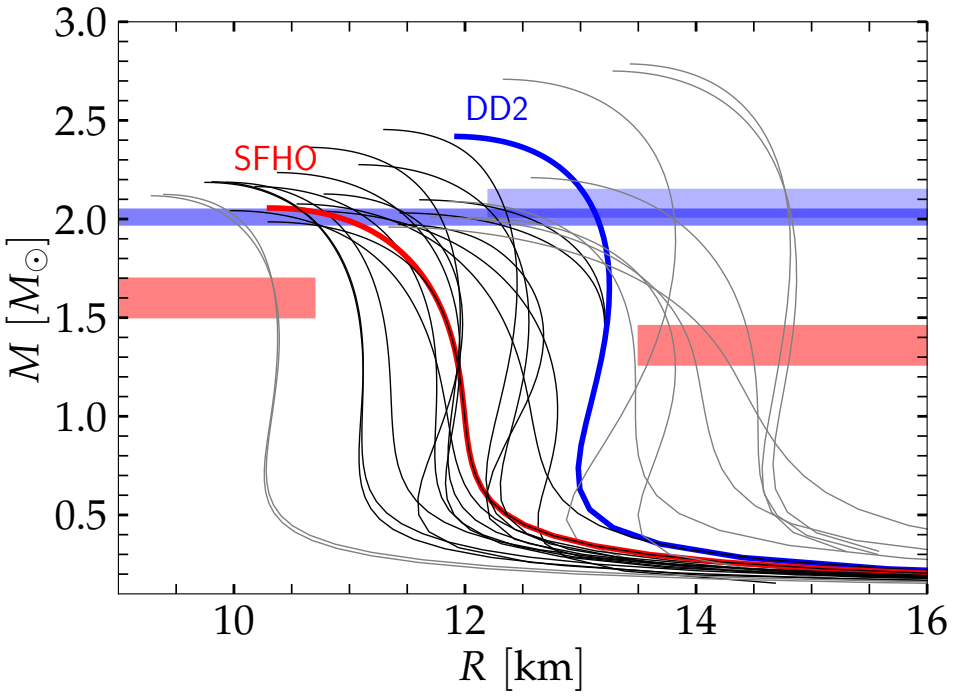

Figure 1.5: Mass-radius relations of different candidate EOS models available in the literature. Throughout this thesis, we exclusively use SFHo and DD2 EOS, which are shown in red and blue. The blue-coloured areas indicate the most massive pulsar measurements and the red-coloured areas provide lower and upper bounds on the NS radii based on GW170817 analysis, which exclude very stiff EOSs and some very soft EOSs [168, 225, 5, 4, 35]. Credit: Andreas Bauswein.

Depending on the total mass, when the binary mass exceeds a certain threshold value $M_{\rm thres}$ [24, 34, 33], the final remnant of the merger can promptly collapse to a BH or otherwise become a massive rotating NS until it goes through a delayed collapse. The magnitude of $M_{\rm thres}$ is significantly influenced by the underlying EOS, which dictates the stability of the merger remnant, i.e. the EOS determines whether, for a specific binary mass configuration, the outcome leads to the formation of a NS remnant or a BH torus system. This significantly have an impact on the ejecta properties since it directly affects the early-stage dynamical mass ejection and leads to a substantial reduction in the total ejecta mass from various outflows. Therefore, a comprehensive understanding of the EOS is essential for interpreting GW emission, nucleosynthesis, and the generation of electromagnetic radiation during merger events [116, 278].

EOS composition: Several theoretical models have been put forward in the literature to describe the EOS of neutron star matter based on nuclear physics, quantum chromodynamics, and effective field theories [140, 196, 37, 220, 209, 219, 129]. In general, an EOS model includes neutrons (n), protons (p), nuclei ($^A_Z X$),

electrons (e^-), positrons (e^+) and photons (γ) as its constituents. Apart from these particles, theoretically, NS matter can also include pions, muons, quarks, hyperons, deconfined quarks, and kaons.

One of those particles of particular interest are pions, which for decades have been speculated that they could exist in the cores of NSs [242, 164, 36, 285, 20, 165, 75, 166, 10]. Despite speculation, there do not exist many BNS merger simulations in the literature where they properly take into account the effects from the inclusion of pions. The presence of pions has been widely neglected in most of the currently available EOSs. Specifically, from previous discussions, there exist relations that connect the stellar properties of NSs to the dominant oscillation mode $f_{\rm peak}$ and the threshold mass $M_{\rm thres}$ of the binary system. These relations have been formulated based on calculations that neglect pions and, to some extent, might be used or are already used in interpreting observations to infer EOS properties. One of the main motivations for the second part of this thesis is to investigate to what extent neglecting pions in existing previous studies could affect these empirical relations and whether it introduces any systematic bias [278].

NS structure: An EOS establishes a unique relationship between different thermodynamic variables such as pressure, density, temperature, etc. The equations describing relativistic hydrostatic equilibrium, commonly referred to as the Tolman–Oppenheimer–Volkoff (TOV) equations [269, 197] connect the cold stellar properties of static NSs to the zero-temperature slice of the EOS models. For each distinct EOS, the TOV equations can be solved by obtaining a specific value of central density and the stellar configuration characterised by different parameters (mass, radius, moment of inertia, etc.) [148]. Depending on different EOSs, the TOV equations producing distinct stellar configurations produce the mass-radius relations, see Fig. 1.5.

One of the ways of testing nuclear EOS models is by means of astrophysical observations of the stellar parameters of static NSs, which allow us to constrain both the mass and the radius [140, 199]. Inferring properties such as the radius of the NS through X-ray pulsar observations is more challenging. Before GW observations became available, very important constraints on the EOS were obtained from mass measurements of various radio pulsars. This offers lower bounds on the maximum mass of the NS. Some of the currently available lower bounds on the maximum mass of a NS (about $2M_\odot$) can be found in [67, 13, 62, 19, 226, 227].

Specifically, a crucial parameter that can be constrained through GWs is tidal deformability [106, 79, 107, 69]. This parameter expresses the quadrupole deformation of the star caused by the tidal field of the companion star [107]. It is defined as,

$$\Lambda = \frac{2}{3} k_2 \left(\frac{R}{M}\right)^5 , \tag{1.3}$$

for each individual star in the BNS system. M and R are the gravitational mass and the radius of the individual non-rotating NSs, k_2 is the tidal Love number [106]. In a binary system, the combined tidal deformability of two stars "1" and "2" is

defined by [106, 79, 107],

$$\tilde{\Lambda} = \frac{16}{13}\frac{(M_1 + 12M_2)M_1^4\Lambda_1 + (M_2 + 12M_1)M_2^4\Lambda_2}{(M_1 + M_2)^5}. \tag{1.4}$$

The event GW170817 allowed us to constrain for the first time the combined tidal deformability $\tilde{\Lambda}$ of the BNS system to be within the range of $100 < \tilde{\Lambda} < 700$ [5, 116]. Specifically, the upper bound of $\tilde{\Lambda}$ which tightly scales with the radius of the NS (from Eq. 1.4 and 1.3) also provides an upper bound on the NS radii, and provides important constraints on the EOS of high-density matter [5, 65]. For instance, the upper bounds of $\tilde{\Lambda}$ inferred from the inspiral GW signal of GW170817 alone constrain the radius of a $1.4M_\odot$ NS to be not more than ~ 13.5 km and exclude any EOS that violates this constraint [4, 5, 76].

Figure 1.5 shows a number of available candidate EOSs used in BNS merger simulations with constraints obtained from various measurements [168, 225, 5, 4, 35]. The tabulated Steiner, Fischer, and Hempel (SFHo) EOS [105, 104, 262] and the DD2 EOS [275, 105, 276] are shown in red and blue to distinguish them from other EOSs. SFHo and DD2 EOSs are among the most widely used EOSs in BNS merger simulations. Throughout this thesis, we exclusively use these two EOSs for all of our merger simulations. From Fig. 1.5, SFHo EOS is softer than DD2 EOS, that is, SFHo EOS produces a comparatively lower pressure support than DD2 EOS. This leads to a higher compactness with lower maximum mass and smaller radii in the mass-radius relationship. As a result, we note that SFHo EOS produces more compact merger remnants than DD2 EOS.

1.6. Goals and structure of the thesis

This thesis is structured in a way to explore two main goals.

Systematic study of BNS mergers with neutrinos (Ch. 3)

Steps toward any realistic kilonova modelling require a proper theoretical understanding of the ejected material and the heating produced from BNS merger simulations, along with a reliable treatment of neutrinos. In pursuit of this objective, we first simulate a 1.35-1.35$M_\odot$ BNS merger using the SFHo EOS and exclusively discuss the impact of neutrinos, mass ejection, and the nucleosynthesis yields from this simulation.

We note that this simulation is used as a starting point for several kilonova modelling, such as the one presented in [55] which presents a 3D radiative transfer kilonova modelling of a BNS merger, and a self-consistent 3D radiative transfer for kilonovae and directional spectra from a merger simulation in [254] and towards inferring the geometry of kilonovae in [56].

In addition, we also conduct several systematic simulations of BNS mergers considering different total masses and mass ratios, in which a set of fewer simulations with a similar setup is used for a complete end-to-end kilonova modelling of neutron-star mergers with delayed BH formation presented in [122]. Based on the data from all these simulations, we aim to address a number of questions.

- What is the distribution of ejecta quantities, such as mass, electron fraction, average velocities, and temperatures, in binary neutron star mergers?
- How does the typical abundance pattern of the elements produced in the BNS merger through the r-process nucleosynthesis look?
- What are the systematics observed in BNS merger simulations when considering different total binary masses, different EOSs, and different mass ratios?

Systematic study of BNS mergers with pions (Ch. 4)

In the second part of the thesis, towards the goal of understanding the composition of NS matter at high-densities, we explicitly introduce the contribution of pions in two candidate EOSs and perform several systematic simulations of BNS mergers using these incorporated pionic EOSs, as presented in [278]. We aim to understand the impact of pions on the outcome of merger simulations and try to gain more insight into a number of questions.

- What are the basic components of NS matter, other than n, p, ${}^{A}_{Z}X$,e^-, e^+,γ? Do pions exist in the interior of the NS?
- If pions exist, what is the impact of pions on observables such as GWs and kilonovae?

- Is the inference of these observables biased by neglecting pions in the currently employed empirical relations for observables?

Unless otherwise stated, throughout this thesis, we adopt the units where $G = \mathrm{c} = 1$, Greek indices denote time and space components (ranging from 0 to 3), Latin indices represent spatial components (ranging from 1 to 3), Einstein summation notation is used, and we adhere to the metric signature $(-,+,+,+)$. Differential operators such as ∇ and ∂_i are defined with respect to a three-dimensional flat metric. In systematic simulations with neutrinos (Ch. 3), when we discuss binary systems where the two NSs have different masses, we define the mass ratio as $q = \frac{M_1}{M_2} \leq 1$, where M_1 and M_2 are the lighter and the heavier partner in the binary system, respectively.

Declaration

The bulk of this chapter follows, **"Improved leakage-equilibration-absorption scheme (ILEAS) for neutrino physics in compact object mergers"**, R. Ardevol-Pulpillo, H-T. Janka, O. Just, A. Bauswein, *Monthly Notices of the Royal Astronomical Society*, Volume 485, Issue 4, June 2019, where the text, figures, and tables have been modified and adapted to suit this thesis.

My contribution of this chapter only includes the implementation of a deterministic version of the code and the hybrid MPI parallelisation of the neutrino scheme.

2. Numerical simulation tool

2.1. Relativistic smoothed particle hydrodynamics

All the compact binary neutron star merger simulations presented in this thesis are simulated using the smoothed particle hydrodynamics (SPH) approach [153, 95, 172] that was described in [194, 193, 28]. The hydrodynamical evolution of the system is computed using the three-dimensional (3D) relativistic Euler equations. The solution to the Einstein field equations is solved on an overlaid 3D Cartesian grid using the CFC approximation [110, 286]. A Lagrangian formalism, i.e. derivatives are evaluated in a comoving reference frame attached to a moving fluid element [194, 232], is employed, with an additional time-dependent artificial viscosity scheme [173, 233] to deal with hydrodynamical shocks and discontinuities. A backreaction scheme [193] is implemented to simulate the loss of energy and angular momentum carried away due to GWs.

Similar to the Eulerian relativistic schemes used in grid codes, the hydrodynamical solver within SPH evolves "conserved" quantities $\rho^*, \hat{u}_i, \tau$, namely the conserved rest-mass density, conserved specific momentum and conserved energy density. They relate to their "primitive" variables, rest mass ρ, velocity v^i, specific internal energy ϵ, through,

$$\rho^* = \rho\alpha u^0 \psi^6, \tag{2.1}$$

$$\hat{u}_i = h u_i = h(v^i + \beta^i)\psi^4 u^0, \tag{2.2}$$

$$\tau = hW - \frac{p}{\rho W} - \sqrt{1 + \frac{\hat{u}_i \hat{u}_j \delta^{ij}}{\psi^4}}, \tag{2.3}$$

where $W = \alpha u^0 = \sqrt{1 + \gamma^{ij} u_i u_j}$ is the Lorentz factor. $\gamma_{ij} = \psi^4 \delta_{ij}$ is the spatial part of the spacetime metric with the Kronecker delta δ_{ij}, u^0 and u_i are the time and spatial components of eigenvelocity, $h = 1 + \epsilon + \frac{p}{\rho}$ is the relativistic specific enthalpy, p is the pressure and α,ψ,β^i are the metric potentials.

The hydrodynamical evolution of the system is described using the relativistic Euler equations with the inclusion of neutrino source terms, $Q_{\rm tot}$, in the momentum and energy equations,

$$\frac{d}{dt}\rho^* = -\rho^* \partial_i v^i, \tag{2.4}$$

$$\frac{d}{dt}\hat{u}_i = -\frac{1}{\rho^*}\alpha\psi^6\partial_i p - \alpha\hat{u}^0\partial_i\alpha + \hat{u}_j\partial_i\beta^j + \frac{2\hat{u}_k\hat{u}_k}{\psi^5\hat{u}^0}\partial_i\psi + \frac{Q_{\rm tot}\alpha\hat{u}_i}{\rho hW}, \tag{2.5}$$

$$\begin{aligned}\frac{d}{dt}\tau = &-\frac{\psi^6}{\rho^*}(v^i+\beta^i)\left(1-\frac{hW}{\omega}\right)(\partial_i p) - \psi^6\frac{p}{\rho^*}\partial_i(v^i+\beta^i) \\ &- 6\psi^5\frac{p}{\rho^*}(v^i+\beta^i)(\partial_i\psi) - \frac{\hat{u}_i}{\psi^4}\left(1-\frac{hW}{\omega}\right)(\partial_i\alpha) \\ &+ \frac{1}{\psi^4}\left(\frac{1}{hW}-\frac{1}{\omega}\right)\left[\hat{u}_i\hat{u}_j\partial_j\beta^i - \frac{1}{3}\hat{u}_i\hat{u}_i\partial_j\beta^j\right] \\ &+ \frac{Q_{\rm tot}\alpha}{\rho}\left[1-\frac{\hat{u}_i\hat{u}_j\delta^{ij}}{\psi^4 hW\omega}\right],\end{aligned} \tag{2.6}$$

where $\frac{d}{dt} = \partial_t + v^i\partial_i$ and $\omega = \sqrt{1+\frac{\hat{u}_i\hat{u}_j\delta^{ij}}{\psi^4}}$.

Within the SPH formalism, the fluid is represented by a number of SPH particles, each having a constant rest mass m_i and a coordinate position r_i. Unlike classical point particles, these SPH particles are spread out in space characterised by the so-called kernel function $W(|\boldsymbol{r}-\boldsymbol{r}_i|, h_i)$. The kernel functions are chosen such that it is normalised, continuous, differentiable, and peaks at the position of the particle, r_i and gradually decreases to zero within a specific spatial range that is determined by the smoothing length, h_i. We note that, unless otherwise stated, this smoothing length is restricted to a maximum length of ~ 150km, in all our simulations. For the kernel, we use a spherically symmetric cubic spline kernel,

$$W(\boldsymbol{r}-\boldsymbol{r}_i, h_i) = \frac{1}{\pi h_i^3}\begin{cases}1-\frac{3}{2}d^2+\frac{3}{4}d^3, & \text{for } 0\le d\le 1\\ \frac{1}{4}(2-d)^3, & \text{for } 1<d\le 2\\ 0, & \text{for } d>2\end{cases} \tag{2.7}$$

where, $d = |\boldsymbol{r}-\boldsymbol{r}_i|/h_i$. Using the kernel, any function can be expressed using a smoothing operator [28],

$$\langle A(\boldsymbol{r})\rangle = \int_{\mathbb{R}^3} A(\boldsymbol{r}')W(|\boldsymbol{r}-\boldsymbol{r}'|, h_i)d^3r'. \tag{2.8}$$

where $\boldsymbol{r}'$ is the integration variable. In terms of SPH particle discretisation,

$$\langle A(\boldsymbol{r})\rangle \simeq \sum_i V_i A(\boldsymbol{r}_i)W(|\boldsymbol{r}-\boldsymbol{r}_i|, h_i), \tag{2.9}$$

where V_i is the particle volume. Using the rest mass of the particles m_i which are fixed, the above expression can be rewritten as,

$$\langle A(\boldsymbol{r})\rangle \simeq \sum_i \frac{m_i}{\rho_i^*}A(\boldsymbol{r}_i)W(|\boldsymbol{r}-\boldsymbol{r}_i|, h_i). \tag{2.10}$$

Using SPH discretisation, the hydrodynamical equations result in a set of ordinary differential equations which are evolved in time with a 4th-order Runge-Kutta (RK) method. The system is closed with a microphysical EOS which is generally provided in the form $p(\rho, \epsilon, Y_e)$ that describes the thermodynamic properties of the stellar fluid. In the case without neutrinos, where the neutrino source terms become zero, the initial electron fraction Y_e of the particles is obtained by solving for the beta-equilibrium condition of the cold stars and advected with the fluid, i.e. $\frac{dY_e}{dt} = 0$. This approximation is used in the simulations discussed in chapter 4, where we only consider pions, and neutrinos are not taken into account. However, for BNS merger simulations with neutrinos (see all the simulations discussed in chapter 3), the inclusion of neutrinos introduces a source term for Y_e which is evolved together with the hydrodynamical equations. See Sec. 2.2 for more details.

The metric potentials are obtained by solving the Einstein field equations in the 3+1 formalism (also known as the ADM formalism) [18] within the conformal flatness condition (CFC) [110, 286] on the spatial metric. Within this approximation, the metric is written as,

$$ds^2 = (-\alpha^2 + \beta_i\beta^i)dt^2 + 2\beta_i dx^i dt + \psi^4 \delta_{ij} dx^i dx^j, \tag{2.11}$$

where ψ is the conformal factor and δ_{ij} is the Kronecker delta. α is the lapse function and β^i is the shift vector. By employing the maximum slicing gauge condition, $K = tr(K_{ij}) = K^i_i = 0$, the Einstein field equations reduce to,

$$\Delta\psi = -2\pi\psi^5 E - \frac{1}{8}\psi^5 K_{ij}K^{ij}, \tag{2.12}$$

$$\Delta(\alpha\psi) = 2\pi\alpha\psi^5(E + 2S) + \frac{7}{8}\alpha\psi^5 K_{ij}K^{ij}, \tag{2.13}$$

$$\Delta\beta^i + \frac{1}{3}\partial^i\partial_j\beta^j = 16\pi\alpha\rho W\hat{u}_i + 2\psi^{10}K^{ij}\partial_j\left(\frac{\alpha}{\psi^6}\right) \equiv S_\beta, \tag{2.14}$$

where E is defined as $E = \rho h W^2 - p$, $S = \rho h(W^2 - 1) + 3p$ and the extrinsic curvature is,

$$K_{ij} = \frac{\psi^4}{2\alpha}\left(\delta_{il}\partial_j\beta^l + \delta_{jl}\partial_i\beta^l - \frac{2}{3}\delta_{ij}\partial_k\beta^k\right). \tag{2.15}$$

These equations are then discretised on a 3D Cartesian grid that encompasses the size of the binary system. The outer boundary conditions are determined by a multipole expansion of the source terms up to second order [17]. The system is evolved in time by solving the hydrodynamical equations through the SPH scheme using the RK method.

In numerical simulations, full 3D general relativistic studies commonly require solving elliptic equations to determine initial data and hyperbolic equations to determine the evolution. Within our SPH simulations, at each timestep, the matter distribution is mapped onto the metric grid and the metric is solved through iterative solutions of the above given elliptic partial differential equations without explicit time dependence until convergence is achieved. The newly acquired metric potentials are then mapped again back to the SPH particles. Compared

to full GR schemes, in our SPH approach with the CFC approximation, we only need to solve the initial value problem repeatedly rather than dealing with the hyperbolic equations. The loss of energy and angular momentum due to gravitational radiation drives the binary system to inspiral and eventually merge. By construction, gravitational radiation is not included in the CFC approximation. In order to simulate mergers, an additional GW backreaction scheme [193] within a post-Newtonian framework is included that provides corrections to the metric potentials [17].

In the SPH method, we also employ an artificial viscosity scheme ([173, 233], with additional modifications from [22] in simulations without neutrinos) to account for the hydrodynamical shocks that can be produced during the merger. The initial data for the simulations are constructed by creating two NSs from zero temperature[1] neutrinoless beta-equilibrium slices of the EOS models and by solving the Tolman–Oppenheimer–Volkoff (TOV) equations [270, 198] for these barotropic relations. The stars are assumed not to have any intrinsic rotation and are placed at an orbital separation chosen such that the merger takes place after a few revolutions. The system is then relaxed without any GW backreaction force until a quasi-circular equilibrium orbit is obtained with a modified orbital angular velocities. This relaxation procedure is carried out using a damping force during this initial phase.

2.2. Modelling of neutrinos with ILEAS

Neutrinos are included in the simulations using the advanced leakage scheme ILEAS [16], which is implemented on a 3D Cartesian grid. Throughout this thesis, we note that we use the same prescriptions given in [16] with an additional implementation of MPI parallelisation in certain modules. ILEAS consists of three main modules to model the various aspects of neutrino transport, namely, leakage, absorption and equilibration. The leakage module calculates the local number and energy rates of the escaping neutrinos by making use of an interpolation between the trapping conditions and free streaming conditions. The absorption module uses a ray-tracing algorithm to determine the number and energy deposition rates of neutrinos that interact with matter in optically thin regions. Meanwhile, at high optical depths, neutrinos equilibrate with matter and can be treated as part of the fluid contributions to its total energy and pressure. This is taken into account separately with an equilibration module.

We incorporate three distinct types of neutrino species in our simulations: electron neutrinos ($\nu_{\rm e}$), electron antineutrinos ($\bar{\nu}_{\rm e}$) and heavy lepton neutrinos (ν_x) to account for both μ and τ neutrinos and their antiparticles. All three species are included in the neutrino leakage. Since we do not explicitly include muons or taons in our simulation, only the interactions of electron neutrinos ($\nu_{\rm e}$) and electron antineutrinos ($\bar{\nu}_{\rm e}$) are considered in the absorption module. All neutrinos are assumed to be massless, given that the energy scales are several MeVs, which are

[1]For simplicity, we use the term "zero temperature" despite the lowest temperature listed in the EOS tables is 0.1 MeV, as same as in [278].

orders of magnitude larger than the neutrino rest mass values. Neutrino flavour oscillations are ignored. Since leakage and absorption involve energy emission and absorption, they provide neutrino cooling rates $Q^{-}_{\nu_i}$ and heating rates $Q^{+}_{\nu_i}$, respectively. The total energy source term described in the hydrodynamical evolution equations in Sec. 2.1 (equations 2.5, 2.6), is calculated as,

$$Q_{\rm tot} = \sum_{i=\nu_{\rm e},\bar{\nu}_{\rm e}} Q^{+}_{\nu_i} - \sum_{i=\nu_{\rm e},\bar{\nu}_{\rm e},\nu_x} Q^{-}_{\nu_i}. \tag{2.16}$$

Similarly, the total electron flavour lepton change rate is calculated from,

$$R_{\rm tot} = R^{+}_{\nu_{\rm e}} - R^{+}_{\bar{\nu}_{\rm e}} - R^{-}_{\nu_{\rm e}} + R^{-}_{\bar{\nu}_{\rm e}}. \tag{2.17}$$

In simulations where the weak interactions are not included, the net electron fraction $Y_{\rm e}$ is normally advected with the fluid ($\frac{dY_{\rm e}}{dt} = 0$). However, in the presence of neutrinos, total electron flavour lepton change rate provides a source term for the evolution equation for $Y_{\rm e}$,

$$\frac{dY_{\rm e}}{dt} = \frac{R_{\rm tot}\alpha}{A\rho W}, \tag{2.18}$$

where A is Avogadro's constant, written in CGS units $A = \frac{1}{m_b}$ and m_b is the atomic mass unit.

Under trapping conditions, in addition to $Y_{\rm e}$, we also advect the fractions of trapped electron neutrinos ($\nu_{\rm e}$) and electron antineutrinos ($\bar{\nu}_{\rm e}$),

$$\frac{dY^{\rm trap}_{\nu_{\rm e}}}{dt} = 0, \tag{2.19}$$

$$\frac{dY^{\rm trap}_{\bar{\nu}_{\rm e}}}{dt} = 0. \tag{2.20}$$

At the end of every timestep, the final value of trapped lepton fraction is obtained using,

$$Y_{\rm lep} = Y_{\rm e} + Y^{\rm trap}_{\nu_{\rm e}} - Y^{\rm trap}_{\bar{\nu}_{\rm e}}. \tag{2.21}$$

From this $Y_{\rm lep}$, at the end of each time step, the equilibration module computes the new equilibrium values for $Y_{\rm e}$, $Y^{\rm trap}_{\nu_{\rm e}}$ and $Y^{\rm trap}_{\bar{\nu}_{\rm e}}$ through an inversion from the constructed set of EOS tables $f(\rho, \epsilon, Y_{\rm lep})$ which takes into account the contribution of the energy and pressure of trapped neutrinos and antineutrinos.

As the main components of ILEAS operates on a 3D Cartesian grid, weak interactions are computed at the grid level, necessitating the mapping of evolved thermodynamic quantities and metric potentials from SPH particles to the grid [17]. After calculating neutrino source terms, these values are remapped from the grid back to SPH particles at the end of each time step. To reduce the computational cost, in simulations involving MPI parallelisation, we skip every second timestep by keeping the values obtained in the previous step constant when calculating the neutrino source terms. Unless explicitly stated otherwise, throughout the thesis, all simulations maintain a standard grid resolution of 0.738 km and a grid size of approximately 225 km for the ILEAS scheme. The components of the ILEAS scheme from [16] is shown in Fig. 2.1. We also show the additional implementation of the MPI parallelisation in the absorption module and in the calculation of diffusion timescales in Fig. 2.1.

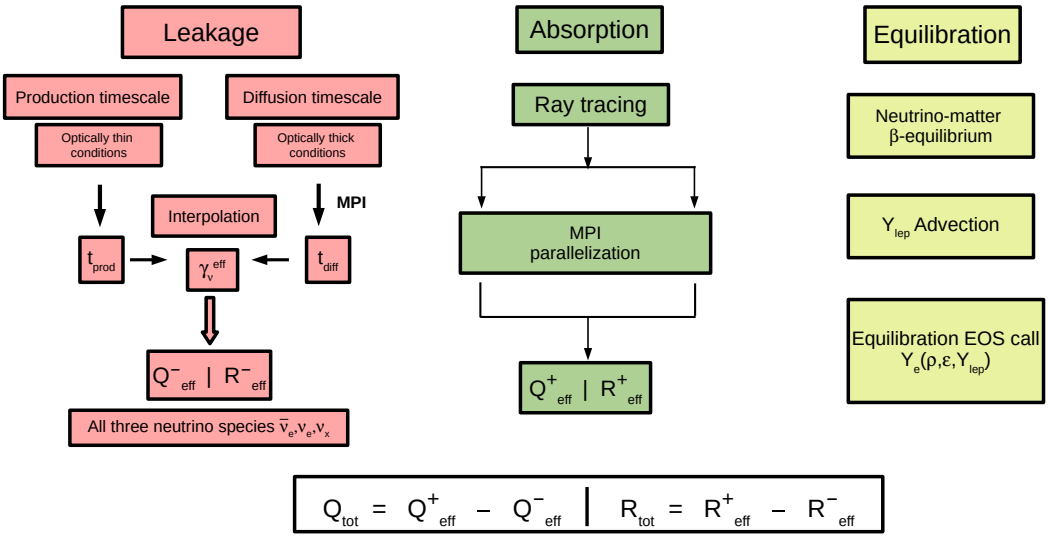

Figure 2.1: The components of ILEAS scheme is illustrated from [16]. It is also shown, the additional implementation of hybrid MPI parallelization in both the absorption module and in the calculation of diffusion timescales.

2.2.1. The neutrino leakage

The leakage part of the code is based on [236]. It calculates the number of produced neutrinos with an effective neutrino production rates by means of an interpolation between the production timescales (optically thin, free streaming regimes), $t^{\rm prod}_{\nu_i}$ and diffusion timescales (optically thick regimes), $t^{\rm diff}_{\nu_i}$. Given the local neutrino production rates for number and energy, R_{ν_i} and Q_{ν_i} respectively, the effective neutrino production rates are given by,

$$R^-_{\nu_i} = R_{\nu_i}\gamma^{\rm eff}_{\nu_i,{\rm num}}, \tag{2.22}$$

$$Q^-_{\nu_i} = Q_{\nu_i}\gamma^{\rm eff}_{\nu_i,{\rm en}}, \tag{2.23}$$

where,

$$\gamma^{\rm eff}_{\nu_i,j} = \left(1 + \frac{t^{\rm diff}_{\nu_i,j}}{t^{\rm prod}_{\nu_i,j}}\right)^{-1}. \tag{2.24}$$

We use the notation $j = 0$ to denote the neutrino number, and $j = 1$ to denote the neutrino energy density.

Production time scale

Assuming that the neutrino spectrum can be modeled using a Fermi-Dirac distribution with temperature, T (expressed in energy units), and neutrino energy, ϵ, we have,

$$f(\epsilon; T, \eta_{\nu_i}) = \frac{1}{1 + e^{(\epsilon/T - \eta_{\nu_i})}}. \tag{2.25}$$

The neutrino degeneracy parameter, $\eta_{\nu_i} = \mu_{\nu_i}/T$, is chosen to be,

$$\eta_{\nu_i} = \eta^{\rm eq}_{\nu_i}(1 - e^{-\tau_{\nu_i}}), \tag{2.26}$$

where μ_{ν_i} is the chemical potential of neutrinos and $\eta^{\rm eq}_{\nu_i}$ is the degeneracy parameter calculated at equilibrium condition. The degeneracy parameter reaches equilibrium values at high optical depths and approaches extremely low values at low optical depths.

The equilibrium degeneracy $\eta^{\rm eq}_{\nu_i}$ for electron neutrinos is determined by the chemical equilibrium condition,

$$\eta^{\rm eq}_{\nu_{\rm e}} = \eta_{\rm e} + \eta_{\rm p} - \eta_{\rm n} - \frac{Q}{T}, \tag{2.27}$$

where $\eta_{\rm e}$ is the electron degeneracy including electron rest mass contributions, while $\eta_{\rm p}$ and $\eta_{\rm n}$ are the proton and neutron degeneracies without including their rest masses. $Q = m_{\rm n}c^2 - m_{\rm p}c^2 = 1.2935$MeV is the neutron and proton rest mass energy difference. The equilibrium degeneracy of electron antineutrinos is assumed to be, $\eta^{\rm eq}_{\bar{\nu}_{\rm e}} = -\eta^{\rm eq}_{\nu_{\rm e}}$, and for heavy lepton neutrinos it is assumed to be zero, $\eta_{\nu_x} = 0$. Assuming neutrinos will follow the paths with minimal interactions, it is fair to assume that they typically travel along directions characterised by the lowest optical depth values. Under this assumption, the optical depth, τ_{ν_i} for neutrino species ν_i, is computed as the minimum value among the optical depths calculated in the six Cartesian directions $(\pm x, \pm y, \pm z)$ using,

$$\tau_{\nu_i} = \int_r^\infty \bar{\kappa}^{j=1}_{\nu_i}(r')dr', \tag{2.28}$$

where $\bar{\kappa}^j_{\nu_i}$ is the spectrally averaged total neutrino opacity. We consider the absorption of electron neutrinos on neutrons, electron antineutrinos on protons, the scattering of all neutrino species on nucleons, alpha particles, and nuclei as the source terms for opacity calculations. The complete details on the calculation of opacities is given in the Appendix in [16]. Since η_{ν_i} is already necessary for the calculation of the opacities, we perform one iteration step by assuming the optical depth to be a function of the density, $\tau_{\nu_i} \propto (10^{11}/\rho)^2$ where ρ is given in g/cm^3. As the results converge very quickly, we do not go for multiple iterations. Once we obtain the neutrino degeneracies, we calculate the neutrino number and energy production rates, R_{ν_i} and Q_{ν_i} for different neutrino interactions. All neutrino interactions considered in the calculation of neutrino production rates are provided in Tab: 2.1. Detailed explanations of these interactions can be found in the reference [16].

As a final step, we define the energy dependent neutrino number and energy density,

$$E^j_{\nu_i}(\epsilon) = g_{\nu_i}\frac{4\pi}{(hc)^3}\epsilon^{2+j}f(\epsilon; T, \eta_{\nu_i}), \tag{2.29}$$

where g_{ν_i} is the multiplicity factor, which is equal to unity for $\nu_{\rm e}$ and $\bar{\nu}_{\rm e}$, and 4 for ν_x. When integrated over the neutrino spectrum, Eq. 2.29 yields,

$$\bar{E}^j_{\nu_i} = g_{\nu_i}\frac{4\pi}{(hc)^3}T^{3+j}F_{2+j}(\eta_{\nu_i}), \tag{2.30}$$

Table 2.1: Neutrino interactions implemented in the calculation of neutrino production rates, from [16]. We denote nucleons, encompassing both neutrons and protons, using $N = \mathrm{p}, \mathrm{n}$. While scattering through alpha particles and nuclei is implemented, it is important to note that the EOSs employed in our simulations consist only of nucleons, electrons, positrons, neutrinos, and photons.

Name	Interactions	ν species
β-react. for ν_e	$\mathrm{p} + \mathrm{e}^- \leftrightarrow \mathrm{n} + \nu_\mathrm{e}$	ν_e
β-react. for $\bar{\nu}_\mathrm{e}$	$\mathrm{n} + \mathrm{e}^+ \leftrightarrow \mathrm{p} + \bar{\nu}_\mathrm{e}$	$\bar{\nu}_\mathrm{e}$
$\mathrm{e}^-\mathrm{e}^+$ annihil.	$\mathrm{e}^- + \mathrm{e}^+ \rightarrow \nu_i + \bar{\nu}_i$	ν_e, $\bar{\nu}_\mathrm{e}$, ν_x
Plasmon decay	$\gamma_\mathrm{trans} \rightarrow \nu_i + \bar{\nu}_i$	ν_e, $\bar{\nu}_\mathrm{e}$, ν_x
N-N bremsstr.	$N + N \rightarrow N + N + \nu_i + \bar{\nu}_i$	ν_x
Nucleon scatt.	$N + \nu_i \rightarrow N + \nu_i$	ν_e, $\bar{\nu}_\mathrm{e}$, ν_x
α part. scatt.	$\alpha + \nu_i \rightarrow \alpha + \nu_i$	ν_e, $\bar{\nu}_\mathrm{e}$, ν_x
Nuclei scatt.	$(A, Z) + \nu_i \rightarrow (A, Z) + \nu_i$	ν_e, $\bar{\nu}_\mathrm{e}$, ν_x

where $F_k = \int_0^\infty x^k f(x; T, \eta_{\nu_i})\, dx$ are the relativistic Fermi integrals of order k. From this, we obtain the production time scales for number and energy as,

$$t^{\mathrm{prod}}_{\nu_i,\mathrm{num}} = \frac{\bar{E}^{j=0}_{\nu_i}}{R_{\nu_i}}, \tag{2.31}$$

$$t^{\mathrm{prod}}_{\nu_i,\mathrm{en}} = \frac{\bar{E}^{j=1}_{\nu_i}}{Q_{\nu_i}}. \tag{2.32}$$

Diffusion time scale

When neutrinos are at high optical depths, they become trapped and diffuse slowly through the medium over longer time scales, $t^{\mathrm{diff}}_{\nu_i}$, similar to a random walk process. By neglecting the neutrino source terms and assuming a static background medium, an energy diffusion equation with energy dependence is derived as,

$$\frac{\partial E_{\nu_i}(\epsilon)}{\partial t} = -\boldsymbol{\nabla} \cdot \boldsymbol{F}_{\nu_i}(\epsilon), \tag{2.33}$$

where $E_{\nu_i}(\epsilon)$ is the neutrino energy density. Assuming an isotropic neutrino distribution, the neutrino flux $\boldsymbol{F}_{\nu_i}(\epsilon)$ is obtained from Fick's law for diffusion (refer [167]) as,

$$\boldsymbol{F}_{\nu_i}(\epsilon) = \frac{-c}{3\kappa_{\nu_i}(\epsilon)} \boldsymbol{\nabla} \boldsymbol{E}_{\nu_i}(\epsilon). \tag{2.34}$$

Since neutrinos with different energies have different diffusion rates, and affect the spectrally averaged diffusion time scale, we keep the energy dependence and integrate Eq. 2.33 to obtain the diffusion timescale,

$$t^{j,\mathrm{diff}}_{\nu_i} = \frac{\bar{E}^{j}_{\nu_i}}{\boldsymbol{\nabla} \cdot \int_0^\infty \frac{-c}{3\kappa_{\nu_i}(\epsilon)} \Lambda^j_{\nu_i}(\epsilon)\, \boldsymbol{\nabla} \boldsymbol{E}^j_{\nu_i}(\epsilon)\, d\epsilon}. \tag{2.35}$$

The details on the calculation of the energy-dependent total opacities can be found in the Appendix of [16], where the energy integration is performed by dividing it into 15 energy bins in logarithmic spacing ranging up to 400 MeV. In (semi)transparent regions where $\kappa \to 0$, to maintain causality, a flux limiter $\Lambda^j_{\nu_i}(\epsilon)$ is used to ensure the appropriate limits on diffusion. For each energy bin, we use a flux limiter from [287, 145] with energy dependence,

$$\Lambda^j_{\nu_i}(\epsilon) = \left(1 + \frac{|\boldsymbol{\nabla} \boldsymbol{E}^j_{\nu_i}(\epsilon)|}{3\kappa_{\nu_i}(\epsilon) E^j_{\nu_i}(\epsilon)}\right)^{-1} \tag{2.36}$$

With relativistic corrections from [253] for an asymptotically flat space-time, we obtain for the diffusion timescale,

$$t^{j,\mathrm{diff}}_{\nu_i} = \frac{\psi^2 \bar{E}^j_{\nu_i}}{\boldsymbol{\nabla} \cdot \left(\alpha \psi^2 \int_0^\infty \frac{-c}{3\kappa_{\nu_i}(\epsilon)} \Lambda^j_{\nu_i}(\epsilon)\, \boldsymbol{\nabla} \boldsymbol{E}^j_{\nu_i}(\epsilon)\, d\epsilon\right)}, \tag{2.37}$$

for $j = 0$ number and $j = 1$ energy density. We note that in order to reduce the time spent by the code in the calculations of the diffusion time scale, we implement a hybrid MPI [94] parallelisation (coupled to OpenMP [64]). This involves splitting the grid cells across different MPI tasks. A comprehensive explanation of this hybrid MPI parallelisation approach is provided in the absorption module (Sec. 2.2.2). The interdependencies among the components of the leakage module from [16] are illustrated in Fig. 2.2. It is also shown in Fig. 2.2, the additional implementation of hybrid MPI parallelisation in the calculation of diffusion timescales.

2.2.2. The neutrino absorption

The neutrinos decoupled from matter typically escape at low optical depths, and depending on the thermodynamical conditions, a considerable fraction of these neutrinos can interact and be re-absorbed from the expanding ejecta. The number and energy of neutrinos absorbed in semi-transparent conditions can have a major impact on the composition of the material that is expelled, and thus on the results of various astrophysical scenarios. This is especially relevant in situations like the shock revival of supernovae, neutrino-driven winds, the composition of ejecta in mergers and the characteristics of kilonovae, from [16]. Traditional leakage schemes generally do not account for the transfer of energy, momentum, and lepton number due to the re-absorption of neutrinos in the ejecta. In these schemes, neutrinos are assumed to either leave the system or become completely trapped, but the interactions between emitted neutrinos and surrounding matter do not influence the evolution of the stellar fluid [85]. Therefore, an absorption scheme is essential for any reliable modelling of compact object mergers. In this study, we use a simple ray-tracing algorithm presented in [16], that is based on the one-dimensional formulation of radiation attenuation by [115]. The approach is expanded to accommodate any 3D geometry, ensuring a more comprehensive treatment of neutrino interactions with the surrounding matter.

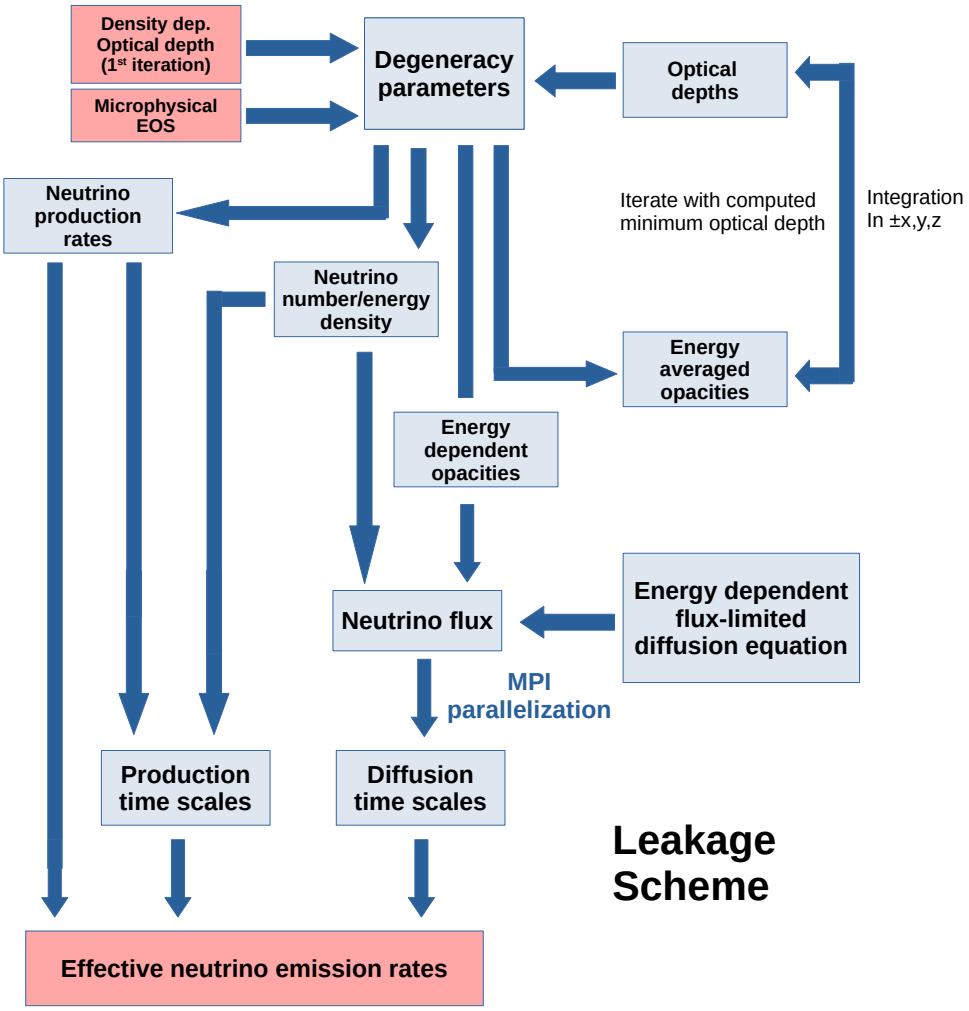

Figure 2.2: Components of Leakage module and their mutual interdependencies, from [16], with an additional implementation of hybrid MPI parallelisation in the calculation of diffusion time scales.

As a first-order approximation, the absorption module assumes that neutrinos emitted from the centre of a given cell escape roughly in the direction of the gradient of the neutrino energy density, $-\boldsymbol{\nabla}\bar{\boldsymbol{E}}_{\nu_i}^{j=1}$, following a straight path. For a given ray, we use a 3D slab formalism from [127] to find the crossing cells. Depending on the distance travelled by the ray, the luminosity of the neutrino is reduced along the path and the deposited energy is estimated. Using a ray coordinate s to describe the position along the rays and the Cartesian coordinates, $\boldsymbol{x}$, to define the centre of the cell, we have for a ray emitted from the centre of a cell, $s = 0$ corresponds to the Cartesian coordinate, $\boldsymbol{x}$, of the cell. And, for the path of the ray which crosses an absorbing cell at $\boldsymbol{x_2}$, the boundaries of the cell which is intersected by the emitted ray are denoted by s_2^- and s_2^+. It should be noted that the re-absorption of neutrinos by the emitted cell itself is included considering a path from the centre, $s_1^- = 0$ to the boundary of the cell, s_1^+ [16].

The luminosity emitted from a cell at the position $\boldsymbol{x_1}$ is estimated as,

$$L_{\nu_i}^{\mathrm{ray}}(\boldsymbol{x_1}) \approx Q_{\nu_i}^{-}(\psi^6 V)_{\mathrm{cell,em}}, \tag{2.38}$$

with the respective metric corrections to the volume of the cell. For a ray that travels along the path from s_2^- to s_2^+, the amount of energy transferred to the absorbing cell per unit volume at position $\boldsymbol{x_2}$ is calculated to be [115],

$$\begin{aligned}[L_{\nu_i}^{\mathrm{ray}}(s_2^+) - L_{\nu_i}^{\mathrm{ray}}(s_2^-)](\psi^6 V)_{\mathrm{cell,ab}}^{-1} = \\ L_{\nu_i}^{\mathrm{ray}}(s_2^-)\left[1 - \exp\left(-\int_{s_2^-}^{s_2^+} \frac{\bar{\kappa}_{\nu_i,a}(\boldsymbol{x_2})}{\langle\chi_{\nu_i}(\boldsymbol{x_2})\rangle}\, ds'\right)\right](\psi^6 V)_{\mathrm{cell,ab}}^{-1},\end{aligned} \tag{2.39}$$

where $L_{\nu_i}^{\mathrm{ray}}(s_2^-)$, $L_{\nu_i}^{\mathrm{ray}}(s_2^+)$ are the neutrino luminosities when a ray enters and leaves an absorbing cell. $\bar{\kappa}_{\nu_i,a}$ denotes the spectrally averaged value of the absorption opacity and $\langle\chi_{\nu_i}(\boldsymbol{x_2})\rangle$ is the energy averaged value of the flux factor. The attenuation of neutrino luminosity is calculated along the path of a given ray, where all relevant thermodynamic and metric quantities are assumed to be uniform within each cell, e.g. $a(s_j^-) = a(s_j^+) = a(\boldsymbol{x_j})$. In addition, the luminosity value at the absorbing cell can be related to the luminosity value of the originating cell through the formula,

$$L_{\nu_i}^{\mathrm{ray}}(s_2^-) = L_{\nu_i}^{\mathrm{ray}}(s_1^-)\exp\left(-\int_{s_1^-}^{s_2^-} \frac{\bar{\kappa}_{\nu_i,a}(\boldsymbol{x_j})}{\langle\chi_{\nu_i}(\boldsymbol{x_j})\rangle}\, ds'\right)\frac{\alpha(\boldsymbol{x_1})^2}{\alpha(\boldsymbol{x_2})^2} \tag{2.40}$$

where $L_{\nu_i}^{\mathrm{ray}}(s_1^-) = L_{\nu_i}^{\mathrm{ray}}(\boldsymbol{x_1})$ and j runs over cells crossed by the originating ray before it reaching the absorbing cell at $\boldsymbol{x_2}$, i.e. s_2^-. It should be noted that the gravitational red-shift of the originating and absorbing cells is taken into account following [190] and Doppler effects are neglected.

The energy averaged neutrino flux factor $\langle\chi_{\nu_i}\rangle$ is defined to be proportional to the ratio between the neutrino flux and the neutrino energy density. Outside the diffusive regime, this definition of local neutrino number or local neutrino energy density becomes invalid, and rather an approximation is necessary to make an estimation. Apart from the two extremes of the flux factor, where it approaches

towards the value 1 in the free streaming conditions and very low values at high optical depths, the flux factor also strongly depends on the geometry. In our BNS merger scenarios with complex 3D geometries, we use the interpolation given in [190],

$$\langle \chi_{\nu_i} \rangle^{-1} = 4.275 \tau_{\nu_i} + 1.15. \tag{2.41}$$

Combining everything, we obtain for the absorption rate, $Q^{+}_{\nu_i}$ of an absorbing cell at position $\boldsymbol{x_2}$ as,

$$Q^{+}_{\nu_i}(\boldsymbol{x_2}) = \gamma^{\text{eff}}_{\nu_i,\text{en}} \sum_{\text{rays}} \frac{L^{\text{ray}}_{\nu_i}(s^-)}{(\psi^6 V)_{\text{cell,ab}}} \left[1 - \exp\left(\frac{-\bar{\kappa}_{\nu_i,\text{a}}(\boldsymbol{x_2})(s^+ - s^-)_{\text{ray}}}{\langle \chi_{\nu_i}(\boldsymbol{x_2}) \rangle}\right)\right], \tag{2.42}$$

where the summation runs over all the rays crossing the absorbing cell and which deposits energy according to Eq. 2.39. The factor $\gamma^{\text{eff}}_{\nu_i,\text{en}}$ is used to ensure that absorption is applied only in the optically thin regions and $(s^+ - s^-)_{\text{ray}}$ is used to restrict the path of each ray within the boundaries of the absorbing cell. The mean absorption opacity of a given cell, $\bar{\kappa}_{\nu_i,\text{a}}$, is calculated with the respective neutrino spectra at a given position in the reference frame of the fluid.

We examine the spectrum of the produced number of neutrinos which slowly diffuse from the hot merger remnant and thermalise the medium (until the optical depth becomes low enough for them to escape) by differentiating distinct cases. We define the neutrinosphere at an optical depth, $\tau_{\nu_i} = 2/3$. For neutrinos produced from a cell at any position s_1 and re-absorbed by cells at s_2 which are inside the neutrinosphere ($\tau_{\nu_i} > 2/3$), we characterise the neutrino spectrum with a Fermi spectrum based on the local temperature and neutrino degeneracy of the absorbing cell, i.e. thermal spectrum, $f(\epsilon; T_{s_2}, \eta_{\nu_i,s_2})$. For neutrinos produced from the inside of the neutrinosphere ($\tau_{\nu_i} > 2/3$) and re-absorbed by cells which are outside the neutrinosphere ($\tau_{\nu_i} < 2/3$), we characterise the spectrum with a Fermi spectrum based on the fluid temperature and the neutrino degeneracy of the last cell crossed by the emitted ray within the neutrinosphere, i.e. neutrinospheric spectrum, $f(\epsilon; T_{\tau_{\nu_i}=2/3}, \eta_{\nu_i,\tau_{\nu_i}=2/3})$. Finally, for neutrinos that are produced outside the neutrinosphere ($\tau_{\nu_i} < 2/3$) and also re-absorbed by the cells outside the neutrinosphere ($\tau_{\nu_i} < 2/3$), we use the same Fermi spectrum of the emitting cell that is described by the fluid temperature and the neutrino degeneracy of the production cell, i.e. production spectrum, $f(\epsilon; T_{s_1}, \eta_{\nu_i,s_1})$, from [16]. Once we obtain the absorption rate, the deposition rate of the lepton number is calculated similar to those presented in the gray absorption schemes [190].

In terms of computational resources, the absorption module appears to be the bottleneck of the simulation, demanding the highest computational cost, which is almost equivalent to 90% of the total computation period. The absorption module determines the total absorption rate by tracing rays emitted from each grid cell in the neutrino grid and calculating their absorption on every other possible cells. For simplicity, rays are not tracked in any random direction like a vector but all the vector quantities are decomposed into different Cartesian components and the absorption is calculated for each of these component. In the end, the

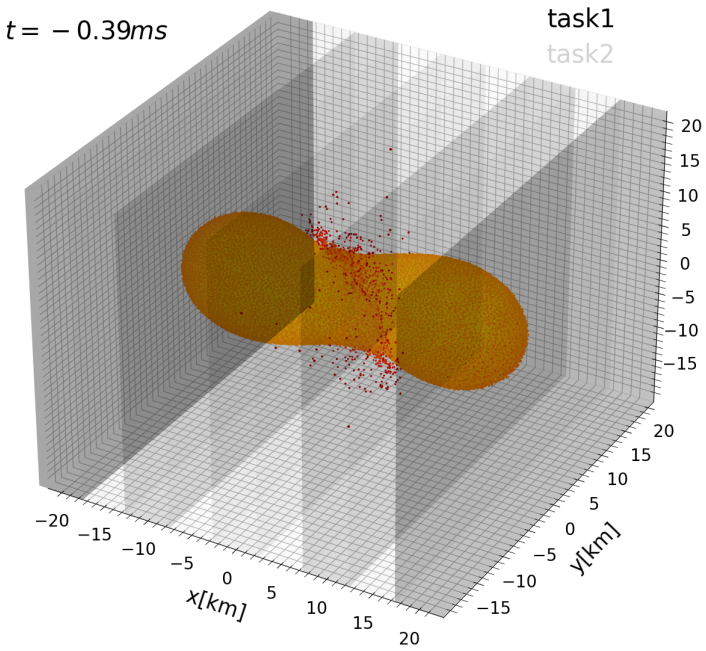

(a) 3D

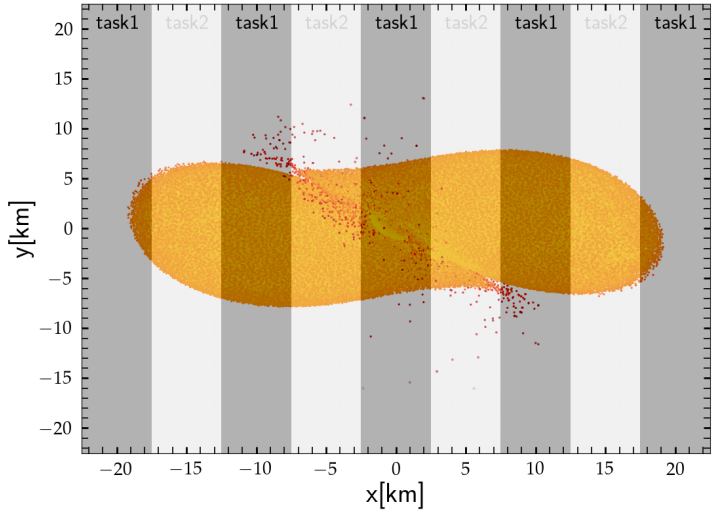

(b) X-Y plane projection

Figure 2.3: A qualitative 3D and a X-Y plane projected visualisation of the MPI hybrid parallelisation implemented in the neutrino absorption and in the calculation of diffusion time scale of ILEAS-SPH code. As an example, we depict the scenario where only two MPI tasks are used and a BNS snapshot is taken about 0.39ms before the merger.

total absorption rate is determined by summing the contribution from all these components and from each individual cell across the entire neutrino grid.

We employ a hybrid MPI parallelisation by dividing the total number of neutrino grid cells into different sections, based on the desired number of MPI tasks (nodes, when each MPI task is split into a different node) used in the computation. Each of these MPI tasks computes the total absorption from all the grid cells contained in that corresponding MPI task. The distribution of grid cells for a specific MPI task is grouped on the basis of a set of planes containing a fixed number of grid cells, separated from each other in a cyclic manner (cyclic block distribution of a do loop). As an example, for a simple case with two MPI tasks split in two different nodes, we provide a qualitative visualisation of the cyclic block division of the grid cells, in Fig. 2.3, both in 3D and in projection on the equatorial plane. We used a snapshot of the BNS system taken approximately 0.39 ms before the merging takes place. The cyclic block distribution of neutrino grid cells into different MPI tasks facilitates an evenly allocated allocation of SPH particles among different MPI tasks. This ensures a balanced distribution of the computational workload among different MPI tasks and promotes efficient parallel processing. Additionally, the MPI tasks are also divided in such a way as to contain a set of planes along the z-direction, perpendicular to the dominant matter ejection direction. This helps, in addition to parallel processing, an evenly spread of the workload from different cells, since the BNS merger remnant structure along the equatorial plane is spread out more than in polar directions.

In the end, the absorption rates from all these neutrino grid cells are computed within their respective MPI tasks and then summed at the end of each absorption call during the evolution. To ensure the consistency of simulations with hybrid MPI parallelisation compared to simulations without parallelization, a comparison of all relevant hydrodynamical and thermodynamical quantities is made between these two setups. This comparison is presented in Appendix A. We find a good agreement between the results obtained from the simulation that uses MPI parallelisation and the one without MPI parallelisation. We note that apart from MPI parallelisation, a deterministic version is also implemented in the code. Additionally, a small resolution study based on the neutrino grid cell size is carried out in Appendix B.

Extraction of the final luminosity and mean energy

From the obtained neutrino emission and absorption rates, the combined total neutrino luminosity that reaches a distant observer in the centre of mass reference frame of the source can be approximated as [16],

$$L^{\rm en}_{\nu_i}(\boldsymbol{x_{obs}}) = \int (Q^-_{\nu_i}(\boldsymbol{x}) - Q^+_{\nu_i}(\boldsymbol{x})) \frac{\alpha(\boldsymbol{x})^2}{\alpha(\boldsymbol{x_{obs}})^2} \psi(x)^6 \, dV, \tag{2.43}$$

for energy, and,

$$L^{\rm num}_{\nu_i}(\boldsymbol{x_{obs}}) = \int (R^-_{\nu_i}(\boldsymbol{x}) - R^+_{\nu_i}(\boldsymbol{x})) \frac{\alpha(\boldsymbol{x})}{\alpha(\boldsymbol{x_{obs}})} \psi(x)^6 \, dV, \tag{2.44}$$

for number. The integral runs over all cells of our assumed neutrino grid. $\boldsymbol{x}$ and $\boldsymbol{x}_{\mathbf{obs}}$ are the respective positions of the last interacting cell and the observer. In the rest frame of an observer at an infinite distance, $\alpha(\boldsymbol{x}_{\mathbf{obs}}) = \alpha(\infty) = 1$.

Unlike traditional leakage schemes, in ILEAS, the mean energy of the neutrinos cannot be directly calculated from the neutrino energy and number luminosity. This is due to the fact that ILEAS modifies the neutrino spectra depending on the optical depth values and requires a different description at optically thick and thin regions. Recalling the definition of neutrinosphere at $\tau_{\nu_i} = 2/3$, in optically thin regions,

$$\langle \epsilon^{\rm thin}_{\nu_i} \rangle (\boldsymbol{x}_{\mathbf{obs}}) = \frac{Q^-_{\nu_i}(\boldsymbol{x}_{\mathbf{1}}) \exp\left(-2\int_{s_1^-}^{s_1^+} \bar{\kappa}^{j=1}_{\nu_i,\rm a}(\boldsymbol{x}_{\mathbf{1}})/\langle\chi_{\nu_i}(\boldsymbol{x}_{\mathbf{1}})ds'\rangle\right)\alpha(\boldsymbol{x}_{\mathbf{1}})}{R^-_{\nu_i}(\boldsymbol{x}_{\mathbf{1}}) \exp\left(-2\int_{s_1^-}^{s_1^+} \bar{\kappa}^{j=0}_{\nu_i,\rm a}(\boldsymbol{x}_{\mathbf{1}})/\langle\chi_{\nu_i}(\boldsymbol{x}_{\mathbf{1}})ds'\rangle\right)\alpha(\boldsymbol{x}_{\mathbf{obs}})}, \tag{2.45}$$

where the spectrally averaged values of opacities for energy and number, $\bar{\kappa}^{j=1}_{\nu_i,\rm a}$ and $\bar{\kappa}^{j=0}_{\nu_i,\rm a}$ are calculated in the same way as in [16].

While considering neutrinos from optically thick conditions i.e. inside the neutrinosphere, and their mean energy, we define an absorption correction factor,

$$c_{\rm abs} = \left[\frac{\exp\left(-\int_{s^-}^{s^+} \bar{\kappa}^{j=1}_{\nu_i,\rm a}(\boldsymbol{x})/\langle\chi_{\nu_i}(\boldsymbol{x})ds'\rangle\right)}{\exp\left(-\int_{s^-}^{s^+} \bar{\kappa}^{j=0}_{\nu_i,\rm a}(\boldsymbol{x})/\langle\chi_{\nu_i}(\boldsymbol{x})ds'\rangle\right)}\right]_{\tau_{\nu_i}=2/3}, \tag{2.46}$$

and calculate their mean energy to be,

$$\langle \epsilon^{\rm thick}_{\nu_i} \rangle (\boldsymbol{x}_{\mathbf{obs}}) = \left[c_{\rm abs} T \frac{F_3(\eta_{\nu_i})}{F_2(\eta_{\nu_i})}\right]_{\tau_{\nu_i}=2/3} \frac{\alpha(\boldsymbol{x}_{\tau_{\nu_i}=2/3})}{\alpha(\boldsymbol{x}_{\rm obs})}. \tag{2.47}$$

The final total mean energy of the emitted neutrinos are then obtained by taking a weighted average over rays emitted from everywhere, both optically thick and thin regions,

$$\langle \epsilon^{\rm tot}_{\nu_i} \rangle = \frac{\sum_{k,\tau_{\nu_i}>2/3} \langle \epsilon^{\rm thick}_{\nu_i,k} \rangle \Delta L_{\nu_i,k}(\boldsymbol{x})}{\sum_{k\in V} \Delta L_{\nu_i,k}(\boldsymbol{x})} + \frac{\sum_{k,\tau_{\nu_i}<2/3} \langle \epsilon^{\rm thin}_{\nu_i,k} \rangle \Delta L_{\nu_i,k}(\boldsymbol{x})}{\sum_{k\in V} \Delta L_{\nu_i,k}(\boldsymbol{x})} \tag{2.48}$$

where the summation runs over all the rays, k, from both inside and outside the neutrinosphere. The denominator runs over the entire grid volume.

2.2.3. The neutrino equilibration

In a NS merger remnant at very high densities and high optical depth conditions, the neutrino diffusion time scales are long enough to safely assume that the neutrinos are trapped in these regions within the typical dynamical timescales. Under these conditions, the trapped neutrinos attain a state of local beta equilibrium with the surrounding matter and contribute to the energy and pressure of the stellar fluid. To close the set of evolution equations in these regions, i.e. hydrodynamical evolution, given in Sec. 2.1, we construct an additional set of EOS tables

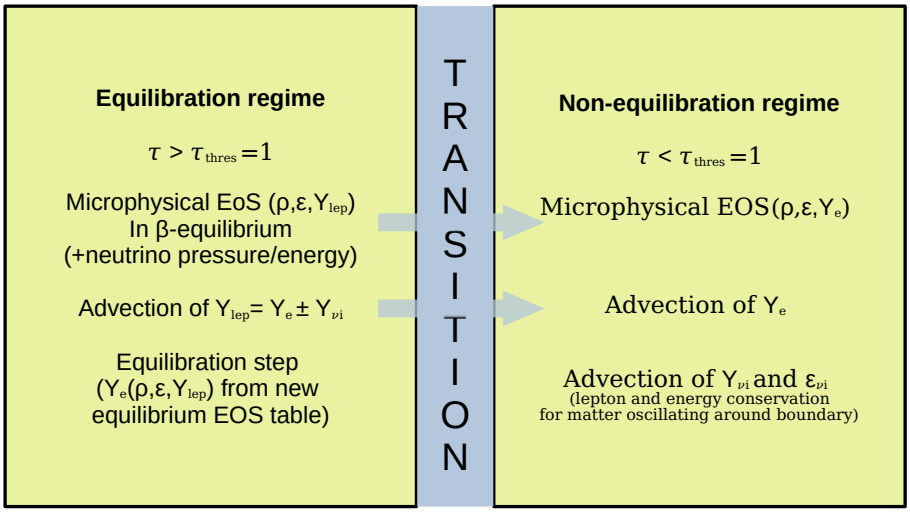

Figure 2.4: The illustration of the functions of the neutrino equilibration treatment in ILEAS, from [16].

which incorporate the contributions of the trapped neutrino species. After each hydro step, we carry out an equilibration step where the total lepton fraction, $Y_{\rm lep}$, is advected and the fraction of the different leptons is recovered from the new equilibrium values of the respective thermodynamic conditions [16].

Neutrino species are treated separately, which requires the construction of additional EOS tables for each possible combination of overlapping equilibration regions of different neutrino species. For example, if in a cell only neutrinos and antineutrinos are trapped and equilibrated, it is necessary to have an EOS table where the total energy and pressure values include only the contributions of energy and pressure from neutrinos and antineutrinos. Depending on the combination of the trapped neutrino species, there exist several possible equilibration regions. Therefore, with the three different neutrino species $\nu_{\rm e}$, $\bar{\nu}_{\rm e}$ and ν_x, we have in total eight different possible combinations, listed in Tab. 2.2. Each of these equilibration regions employs a different EOS table that provides the relevant thermodynamical quantities as a function of density, ρ, the specific internal energy of the fluid with the corresponding contribution of the trapped neutrinos, ϵ, and the trapped lepton fraction, $Y_{\rm lep}$. Since ν_x are produced in pairs and do not carry any electron flavour, only $\nu_{\rm e}$ and $\bar{\nu}_{\rm e}$ does affect the trapped lepton fraction.

During the evolution, depending on the thermodynamical conditions, the SPH particles may transition between various equilibration regions and, correspondingly, the grid cells. To avoid violation of energy conservation, in each timestep, we retrieve the specific energy of neutrinos, ϵ_{ν_i}, from the EOS tables and add or subtract the respective contribution of neutrinos to the internal energy of the fluid. Since the ϵ_{ν_i} values are only updated inside the equilibration regions (optically thick) of ν_i, outside the equilibration, we advect the ϵ_{ν_i} values by assuming that they are not in equilibrium with the surrounding matter. Likewise, the individual neutrino fractions, Y_{ν_i} are advected in the whole region according to Eq. 2.19 and 2.20 instead of the respective trapping regions, to avoid the non-physical be-

haviour of energy or lepton loss by fluid elements oscillating around the boundary between equilibration and non-equilibration regimes.

Table 2.2: Equilibration regions employed in ILEAS from different possible combinations of trapped neutrino species, from [16].

Equilibration regions	Trapped ν species
1	$\nu_{\rm e}$, $\bar{\nu}_{\rm e}$, ν_x
2	$\nu_{\rm e}$, $\bar{\nu}_{\rm e}$
3	$\nu_{\rm e}$, ν_x
4	$\bar{\nu}_{\rm e}$, ν_x
5	$\nu_{\rm e}$
6	$\bar{\nu}_{\rm e}$
7	ν_x
8	none

The tabulated quantities in our new EOS table are the fluid pressure with the included contributions from the trapped neutrinos, p, the temperature, T, the chemical potentials of neutron, proton and electron, $\mu_{\rm n}$, $\mu_{\rm p}$ and $\mu_{\rm e}$, individual lepton fractions, $Y_{\rm e}$, $Y^{\rm trap}_{\nu_{\rm e}}$, $Y^{\rm trap}_{\bar{\nu}_{\rm e}}$ and the neutrino specific energy contributions, $\epsilon_{\nu_{\rm e}}$, $\epsilon_{\bar{\nu}_{\rm e}}$,$\epsilon_{\nu_{\rm x}}$. The pressure of each of these neutrino species is calculated from the neutrino equilibrium energy density ($j = 1$) (Eq. 2.30) as,

$$p_{\nu_i} = \frac{\bar{E}^1_{\nu_i}}{3}, \tag{2.49}$$

and, the trapped neutrino fraction is obtained from the equilibrium number density of neutrinos $j = 0$ as,

$$Y^{\rm trap}_{\nu_i} = \frac{\bar{E}^0_{\nu_i}}{\rho A}. \tag{2.50}$$

Finally, the specific internal energy of each neutrino species is obtained from the equilibrium energy density of neutrinos as,

$$\epsilon_{\nu_i} = \frac{\bar{E}^1_{\nu_i}}{\rho c^2}. \tag{2.51}$$

We note that an analytical approximation is used for the Fermi integrals from [263] and the equilibrium energy density contribution for $\nu_x\bar{\nu}_x$ pairs is calculated from the analytical expressions given in [44]. The diagram illustrating the functions of the neutrino equilibration scheme is given in Fig. 2.4.

Declaration

The parts of this chapter are based on the works, **"Neutrinos and their impact on the nucleosynthesis in binary neutron star mergers"**, Vimal Vijayan, Andreas Bauswein, Gabriel Martinez-Pinedo, *PoS* FAIRness2022, 061, June 2023, and,
"3D radiative transfer kilonova modelling for binary neutron star merger simulations", Christine E. Collins, Andreas Bauswein, Stuart A. Sim, Vimal Vijayan, Gabriel Martínez-Pinedo, Oliver Just, Luke J. Shingles, Markus Kromer, *Monthly Notices of the Royal Astronomical Society*, Volume 521, Issue 2, May 2023. The text and illustrations have been modified and adapted to suit this thesis.

3. Binary neutron star merger simulations with neutrinos

In this chapter, we investigate in detail the dynamical mass ejection from BNS merger simulations including neutrinos. The hydrodynamic evolution of the merger is described by a 3D relativistic smoothed particle hydrodynamics (SPH) code [193, 28] with an improved leakage plus absorption scheme [16] to describe neutrino cooling and heating. Throughout, we consistently use this state-of-the art ILEAS scheme (see Sec. 2.2) for the treatment of neutrinos. The numerical settings adopted in the SPH simulations are the same as detailed in [16, 136, 55, 277, 122, 254, 56], and the initial data are constructed as discussed in Sec. 2.1. For all simulations, we use a total number of about 300000 SPH particles, and the neutrino source terms are computed on a uniform three-dimensional Cartesian grid having 305 cells of size 738 m along each dimension.

In the first part of this chapter, we simulate a 1.35-1.35$M_\odot$ BNS merger using the SFHo EOS and exclusively discuss the impact of neutrinos, mass ejection, and the nucleosynthesis yields from this simulation. Recalling the importance of the electron fraction Y_e in ejecta properties and in determining the amount of elements created by r-process nucleosynthesis, we find that the distribution of Y_e and most of the properties of the ejecta are consistent with existing simulations [248, 217, 136, 96, 92, 182, 40, 207, 42, 63]. We calculate the nucleosynthesis yields for the dynamical ejecta and observe that the second and third r-process peaks are robustly generated with isotopic abundances that closely resemble the solar abundance [99]. Contrary to many simulations in the literature, we do not find a collapse of our simulation into a BH at the end of the simulation. We observe relatively higher temperatures in our ejecta composition and consequently larger Y_e values that span a wider range.

In the second part of this chapter, we conduct a systematic study of BNS merger simulations with neutrinos based on SFHo and DD2 EOS considering different total masses and mass ratios. We focus on the merger dynamics and assess the correlation between the mass of the dynamical ejecta and its properties, taking into account variations in the binary parameters and the NS EOS.

When comparing the postmerger evolution of symmetric binaries to their asymmetric counterparts with the same total mass, we observe a systematic decrease in the dominant GW oscillation frequencies and a relatively quick approximate plateau of the maximum densities for a larger asymmetry of the binary mass. Additionally, the merger remnants of asymmetric mergers produce higher tempera-

tures, higher average electron fractions, and higher neutrino luminosities following a hierarchy $L_{\bar{\nu}_e} > L_{\nu_x} \geq L_{\nu_e}$, which is consistent with the results of [16].

Looking at the ejecta properties, we notice an overall increase in the mass of the ejecta for simulations that feature higher total masses and larger binary mass asymmetry. For a given total mass, we also observe higher temperatures generated within the ejecta of asymmetric merger, and a more spherical distribution of the ejecta mass per unit solid angle. Despite these higher temperatures produced within the ejected particles, we find that the typical neutron-richness of the dynamical ejecta in asymmetric mergers tends to be relatively higher compared to their corresponding symmetric counterparts [248, 92, 136, 120, 183, 40]. Specifically, we find a relatively larger number of particles ejected from the larger radii of the central remnant compared to symmetric mergers. These particles which are ejected from larger radii experience less neutrino irradiation, and the Y_e value of these particles does not evolve much (from Eq. 2.18). This results in the ejecta particles being close to their β-equilibrium values (see Fig. 4.7), preserving the neutron-richness of the material, and contributing less to the increase in the average Y_e value of the ejecta.

3.1. A 1.35-1.35$M_\odot$ BNS merger simulation with neutrinos

Motivated by the inferred mass range of GW170817 [53], we simulate a BNS system with 1.35-1.35$M_\odot$ using the SFHo EOS as our first model. The simulation is run until approximately $\sim$ 20 ms after the merger, and during this simulation period, we do not find a collapse to a BH. We find that quantities such as the minimum of the lapse function, the maximum density, the quadrupole moment, and $f_{\rm peak}$, which are mainly dependent on the high-density part of the central remnant, are minimally affected by the inclusion of neutrinos. The neutrino production has only mild softening effects, but has an overall negligible impact on the dynamics of the central remnant. However, ejecta properties such as the mass of the ejecta, the temperature distribution, the distribution of Y_e and the velocity distribution, are considerably affected by the inclusion of neutrinos. In order to estimate the importance of including neutrinos in BNS merger simulations, we also simulate a BNS merger with the same initial setup but by turning off neutrinos after the merger when the minimum of the lapse function occurs (similar to the setup "without neutrinos" in [136]). Here, we denote this simulation by "ν turn off". Note that it is possible to run the entire simulation without including neutrinos, as in [28, 24, 43, 278] where the values of Y_e are just advected throughout the simulation. However, the magnitude of Y_e distribution in these simulations remains low and narrow ($Y_e \lesssim 0.1$), since they correspond to the initial Y_e values obtained from neutrinoless beta-equilibrium condition (see Fig. 4.7). Hence, for better visualisation purposes and to evolve the electron fractions of the particles to higher values from their original β-equilibrium values, we stick to this prescription in which the neutrinos are turned off after the merger.

3.1.1. Distribution of the ejecta

Clearly, a key quantity of interest is the mass of the ejecta $M_{\rm ej}$, which determines the overall production of heavy elements and the properties of the electromagnetic transient. The mass ejection of BNS mergers includes several phases, as discussed in chapter 1. Here, we focus mainly on the properties of the ejected SPH particles only during the first 20 milliseconds after merging, since the simulations used in this study can only assess the dynamical ejecta. These ejecta particles are identified by considering an energy criterion which compares kinetic, thermal, and gravitational energy to check which fluid elements become gravitationally unbound [193].

The initial data for kilonova calculations (used in [55, 254, 56]) are obtained using homologous expansion of the ejected trajectories up to a few hundreds of milliseconds (~ 0.5s). It is a reasonable approximation to assume that within this time period, the position of the particle moves along the direction of its velocity such that the angular dependence of the particles is purely determined by the angle of the velocity vectors. For this reason, in all of our figures where we show the angular distribution, we use the angles subtended by the velocity vectors as our polar angles instead of the angles based on the position of the particles at the end of the simulation. Angle binning is made relative to the positive z-axis with the angle subtending from 0° to 180° in small intervals of 10 degrees, as shown in Fig. 3.1.

In Fig. 3.1(a), we compare the angular distribution of the ejected mass $M_{\rm ej}$ per unit solid angle for the simulation that includes neutrinos with the simulation in which neutrinos are turned off. We notice an overall decrease in the ejecta mass in simulation with neutrinos. This is due to the reduction in temperatures caused by the presence of strong neutrino cooling. Figures 3.1(b), 3.1(c) and 3.1(d) show the mass-averaged[1] value of the ejecta temperatures, ejecta velocities and ejecta $Y_{\rm e}$ with respect to the ejecta masses in each angular bin. Note that, along with the mass of the ejecta, a decrease in the mass-averaged temperature of the ejected particles is also observed in Fig. 3.1(b).

Figure 3.1(c) shows the comparison of the mass-averaged velocity along each angular bin. It is observed that the angular distribution of the mass-averaged velocities is nearly spherical with an average velocity of approximately 0.2c-0.3c in simulation with neutrinos, while it shows strong fluctuations when neutrinos are turned off. Looking at Fig. 3.1(d), we find a considerable increase in the mass-averaged $Y_{\rm e}$ values when neutrinos are included. This is evident from the discussions in Sec. 2.2 and from Eq. 2.18 where the source terms from neutrinos are the main contribution that drives the $Y_{\rm e}$ to higher values due to weak interactions. Without neutrinos, the distribution of $Y_{\rm e}$ values does not evolve and remains close to the β-equilibrium values of the initial cold NSs. In addition, it is also observed that the mass-averaged values of $Y_{\rm e}$ along the polar direction are comparatively

[1]We calculate a mass-averaged value by summing the contributions from all SPH particles, with each contribution weighted by the mass of the particle relative to the total mass, as same as in [278]. Note that we often use the mass-averaged value in SPH simulations to explore the average value of any quantity.

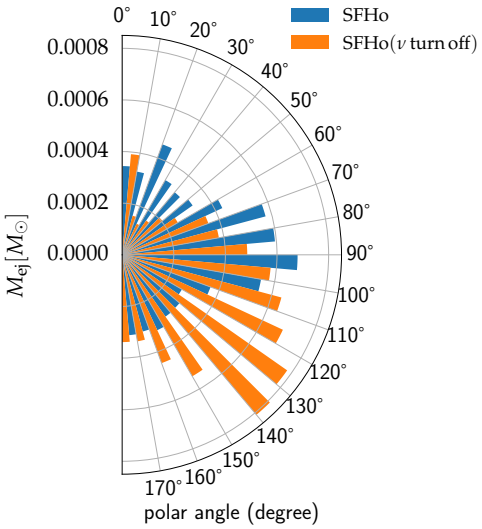

(a) Ejecta Mass

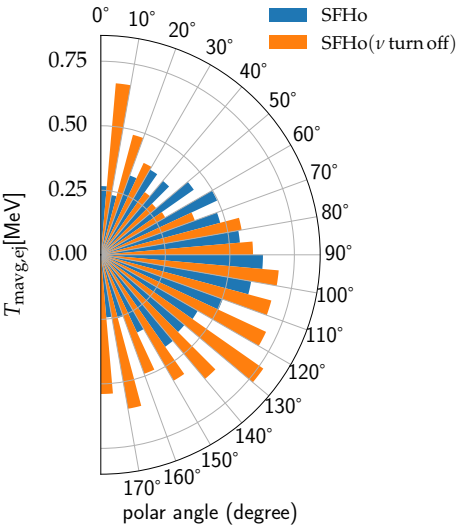

(b) Mass-averaged ejecta temperature

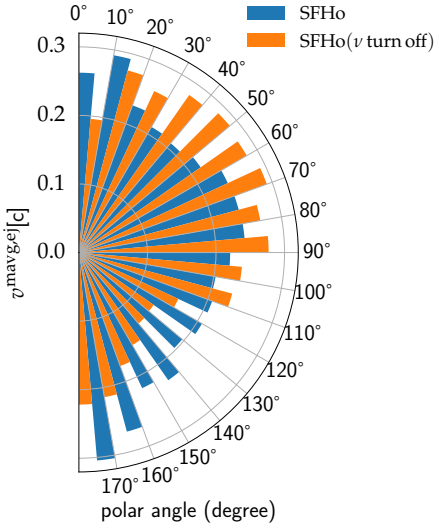

(c) Mass-averaged Velocity

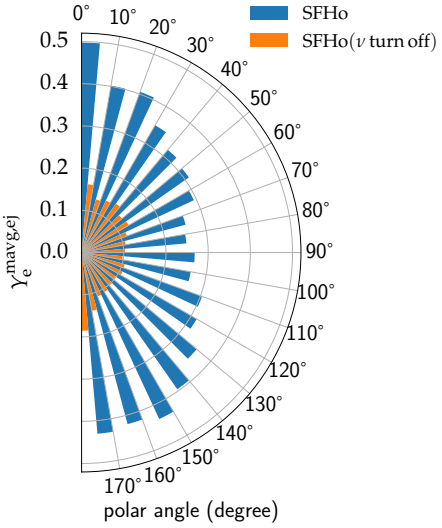

(d) Mass-averaged electron-fraction

Figure 3.1: The angular distribution of ejected mass, mass-averaged temperature, mass-averaged velocity and mass-averaged electron fraction in each bin, within the end of the simulation period for a 1.35-1.35$M_\odot$ BNS merger using SFHo EOS. The simulation with ILEAS neutrino leakage scheme is represented by blue histograms, and the simulation where the neutrinos are turned off after the merger (where the minimum of the lapse function occurs) is represented by orange histograms. The width of the histogram bin is reduced by half and shifted to accommodate the visualisation of both simulations within a single angular bin.

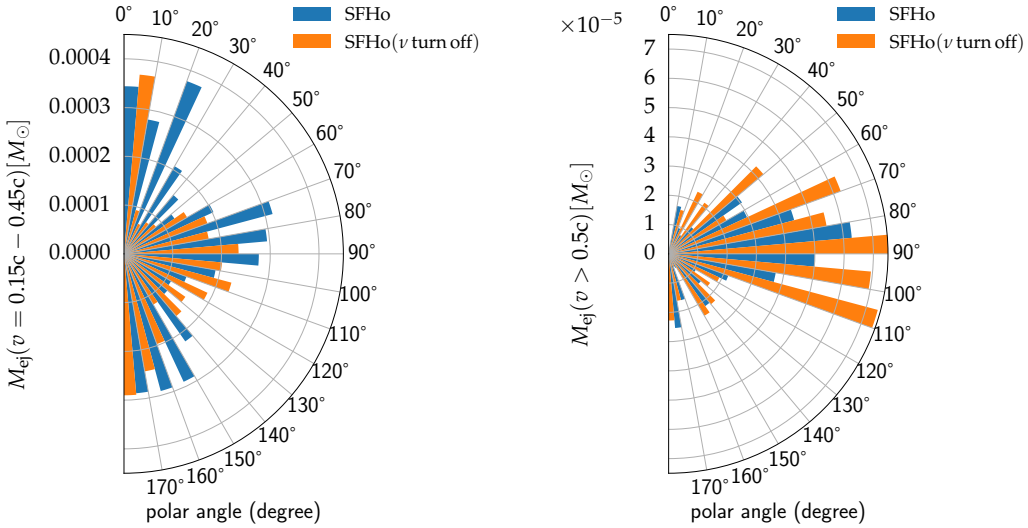

(a) Ejecta mass with velocity 0.15c-0.45c

(b) Ejecta mass with velocity > 0.5c

Figure 3.2: The angular distribution of ejected mass constrained by velocity range between 0.15c-0.45c and above 0.5c, within the end of the simulation period for a 1.35-1.35$M_\odot$ BNS merger using SFHo EOS. The simulation with ILEAS neutrino leakage scheme is represented by blue histograms, and the simulation where the neutrinos are turned off after the merger (where the minimum of the lapse function occurs) is represented by orange histograms. The width of the histogram bin is reduced by half and shifted to accommodate the visualisation of both simulations within a single angular bin.

higher than those in the equatorial direction. This is expected since the amount of neutrinos produced along the polar direction is larger (Fig. B.1) and gives rise to higher electron fraction values. Further discussions on this, and a detailed mapping of $Y_{\rm e}$ along the z-axis of a BNS merger snapshot can be found in [16].

While we did not see a considerable difference in the distribution of the mass-averaged velocity in each polar direction (from Fig. 3.1(c)), we cannot rule out the possibility that the amount of ejecta mass produced within different velocity intervals may have a completely different angular distribution. In Figs. 3.2(a) and 3.2(b), we show the amount of ejecta mass per unit solid angle within the velocity range of 0.15c-0.45c and above 0.5c. When considering only the velocity range 0.15c-0.45c, the mass distribution of the ejecta almost looks symmetric. Note that, due to the limited resolution of the underlying SPH particles, variations can occur in each polar bin from one to another. Increasing the bin intervals to larger angles could significantly alter these values to a more spherical distribution; see [56]. It is important to note that most of the high-velocity (> 0.5c) ejecta components are ejected along the equatorial direction, where the relative $Y_{\rm e}$ values are lower and more neutron-rich [161].

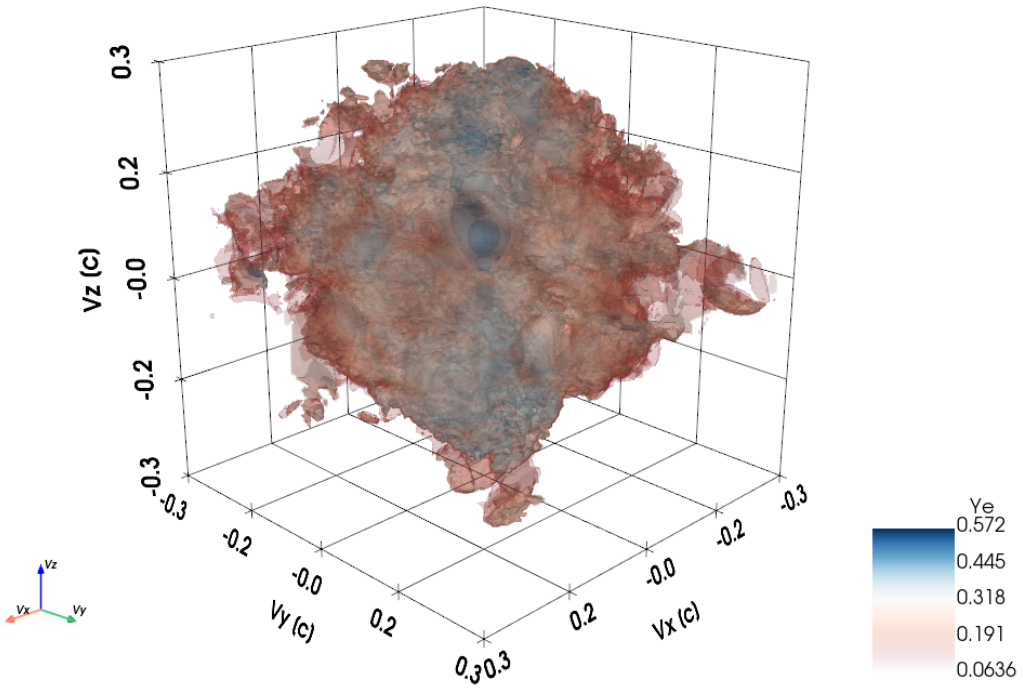

Figure 3.3: Mapping of the dynamical ejecta onto a Cartesian grid in velocity space, with the v_z axis corresponding to the rotation axis (or polar axis) of the system. The equatorial plane is represented by $v_z = 0$. For visual clarity, we do not display grid cells with contributions from fewer than 5 SPH particles. The colour scale is determined by isosurfaces that show the average Y_e in each grid cell. Generally, the material near the equator has a lower Y_e than in the polar directions, based on [55].

3.1.2. Composition and nucleosynthesis

As a starting point for the kilonova modelling, at the end of our simulation ($\sim$ 20 ms after the merger), we extract the trajectories of all the ejected particles from our SPH simulation despite mass still being ejected through different channels (see the introduction of chapter 1) and will continue. We obtain a total mass of about 0.005 $M_\odot$ produced from our dynamical simulation. As discussed in Sec. 1.3, the Y_e and velocity distribution of the ejected material is one of the fundamental quantities which determines the properties of the produced kilonova. It is important to understand which regions of the BNS merger remnant produce high Y_e and at which velocity these ejecta are produced. We present this in Fig. 3.3, by showing a 3D mapping of the dynamical ejecta of the merger remnant in velocity space, approximately $\sim$ 20 ms after the merger. The colour scale indicates Y_e of the ejecta, where the values of Y_e are taken to be the values at the end of the merger simulation, indicating the three-dimensional structure produced by the merger.

As already demonstrated in Fig. 3.1(d), the illustration in Fig. 3.3 reveals that the material near the equator has lower values of Y_e, while the material in the polar directions has higher values of Y_e, consistent with results from previous works [217, 87, 96, 136, 55]. However, we point out that the polar directions are not composed only of high Y_e material, but rather mixed with lower Y_e and higher Y_e materials [119].

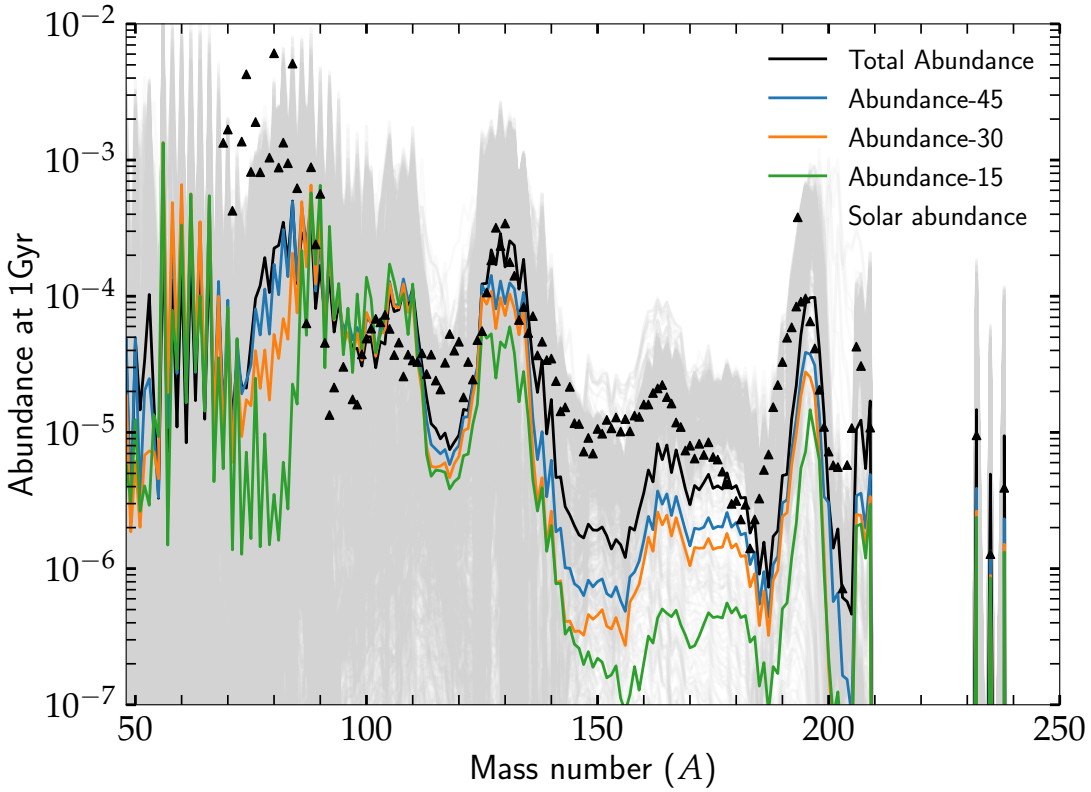

Figure 3.4: The mass-averaged total abundance (black line) from each ejected SPH particle in a 1.35-1.35$M_\odot$ BNS merger simulation using the SFHo equation of state is compared to the solar abundance (black triangles) [99]. The mass-averaged abundance for various amounts of ejecta binned by different angular ranges is shown in blue, green and purple lines using the polar angle θ (blue: $0° < \theta < 15°$, orange: $0° < \theta < 30°$ and green: $0° < \theta < 45°$). The transparent grey lines in the back indicate the individual abundance pattern obtained from each ejected SPH particle trajectories, based on [277].

To calculate the energy release in the ejecta and the various amounts of elements produced, we start a time-dependent nuclear network calculation for each SPH particle when the temperature of the ejected particle falls to 1 MeV ($\sim 10^{10} K$). In cases where the temperature of the particle remains above 1 MeV at the end of the simulation, we adopt the temperature reached at the last time step of the hydrodynamical simulation as our starting point for network calculations. Furthermore, we also use the Y_e value of the SPH particle to determine the composition at the beginning of the network calculations. Since the nucleosyn-

thesis calculations extend beyond the end of our hydrodynamical simulation, it intrinsically assumes that the value of Y_e at the end of the SPH simulation remains constant and does not change further during the network calculations. In fact, this is anticipated by the simulations, where during this phase the expansion time scale is significantly shorter than the weak interaction time scale, and the Y_e values of most ejected particles are observed to reach a plateau [55]. Given the temperature and Y_e, the initial composition of the ejecta is determined by assuming nuclear statistical equilibrium (NSE) for the density derived from the SPH data. After the end of our hydrodynamical simulation, these densities are extrapolated by assuming homologous expansion that satisfies the condition $\rho(t)r(t)^3 = \rho_0 r_0^3$. Here $r(t) = r_0 + v_0(t - t_0)$, where r_0 and v_0 are the radial position and velocity at time t_0. We note that t_0 is the time of the end of the simulation period ($\sim$ 20 ms after the merger in our case). Thus, the density evolution is determined using the expression,

$$\rho(t) = \rho_0 \left(\frac{\Delta + t_0}{\Delta + t} \right)^3 \tag{3.1}$$

where $\Delta = \frac{r_0}{v_0} - t_0$.

We employ the same nuclear reaction network as presented in [157], using the set of nuclear reactions labelled "FRDM". In summary, the reaction network incorporates neutron capture and photodissociation rates calculated within the statistical model, using FRDM masses [170]. For nuclei with experimentally unknown β-decay rates, we refer to the compilation provided by [171]. Fission rates [203] are calculated based on the Thomas-Fermi fission barriers outlined in [175] and β-decay rates are calculated using the Viola-Seaborg formula [71] for nuclei lacking experimental values.

Following the calculations of the nucleosynthesis network, we derive the abundance of each individual trajectory. Considering all trajectories, we compute the total mass-averaged abundance, which is then compared to the solar abundance [99]. This is illustrated in Fig. 3.4 for a 1.35-1.35$M_\odot$ BNS merger using the SFHo EOS. We further evaluate the abundance pattern with respect to different polar angles based on various amounts of ejecta mass binned by different angular ranges. This is shown in Fig. 3.4 using blue, green and purple lines where different angular ranges are indicated by the polar angle θ, $0° < \theta < 15°$, $0° < \theta < 30°$ and $0° < \theta < 45°$, respectively.

Along the polar direction, the ejecta are observed to exhibit higher values of Y_e and result in a notable reduction in the abundance of heavy elements. Consequently, the production of lanthanides along the polar direction decreases as we move closer to the polar z-axis. Despite the reduction in the amount of lanthanides, we observe that the second and third r-process peaks are more robustly generated with isotopic abundances that closely resemble the solar abundance. Therefore, we observe a distinct correlation between the initial Y_e composition of the ejecta (at the beginning of nuclear network calculations) and the resulting heavy elements, consistent with the existing results (see [60] for a review). We note that, at the end of the nuclear network calculations, heating rates and abundances are derived attributed to radioactive decays and are subsequently used in advanced kilonova modelling through radiative transfer calculations [55, 254, 56].

3.2. Systematic study of neutrino simulations

Table 3.1: The list of simulations used in the systematic study of BNS merger simulations with neutrinos. The table lists characteristics of the simulations, such as the EOS, the individual masses of the NSs in the binary system, the mass ratio, the total mass, the dominant postmerger oscillation frequency $f_{\rm peak}$, the ejected mass $M_{\rm ej}$, and the mass-averaged electron fraction $\langle Y_{\rm e}\rangle^{\rm ej}$ of the ejecta.

EOS	M_1 $[M_\odot]$	M_2 $[M_\odot]$	q	$M_{\rm tot}$ $[M_\odot]$	$f_{\rm peak}$ [kHz]	$M_{\rm ej}$ $10^{-3}[M_\odot]$	$\langle Y_{\rm e}\rangle^{\rm ej}$
SFHo	1.3	1.3	1	2.6	3.229	2.974	0.308
	1.35	1.35	1	2.7	3.372	4.077	0.304
	1.375	1.375	1	2.75	3.431	5.057	0.307
	1.4	1.4	1	2.8	3.561	6.820	0.307
	1.45	1.45	1	2.9	-	-	-
	1.11428	1.48571	0.75	2.6	3.074	8.878	0.276
	1.15714	1.54286	0.75	2.7	3.221	11.324	0.261
	1.17857	1.57143	0.75	2.75	3.304	11.895	0.288
	1.2	1.6	0.75	2.8	3.412	12.017	0.294
	1.24286	1.65714	0.75	2.9	-	-	-
DD2	1.3	1.3	1	2.6	2.581	2.715	0.345
	1.35	1.35	1	2.7	2.639	3.105	0.328
	1.375	1.375	1	2.75	2.662	2.951	0.328
	1.4	1.4	1	2.8	2.685	3.280	0.320
	1.45	1.45	1	2.9	2.749	3.712	0.319
	1.11428	1.48571	0.75	2.6	2.524	6.824	0.250
	1.15714	1.54286	0.75	2.7	2.580	7.461	0.257
	1.17857	1.57143	0.75	2.75	2.601	7.723	0.256
	1.2	1.6	0.75	2.8	2.627	8.968	0.268
	1.24286	1.65714	0.75	2.9	2.680	9.358	0.276

In this section, we extensively investigate 3D relativistic BNS merger simulations using the SPH code with neutrinos and describe the results with particular attention to their dependence on the total mass and the mass ratio. We perform a systematic set of BNS merger simulations by changing the total mass of the BNS system from $2.6M_\odot$ to $2.7M_\odot$, $2.75M_\odot$, $2.8M_\odot$ and $2.9M_\odot$, and the mass ratio from $q = 1$ to $q = 0.75$, using the SFHo and DD2 EOS. This amounts to a total of 20 BNS merger simulations. The characteristics of these simulations, such as the EOS, the individual masses of NSs in the binary system, the mass ratio, the total mass, the dominant postmerger oscillation frequency $f_{\rm peak}$, the ejected mass $M_{\rm ej}$, and the mass-averaged electron fraction $\langle Y_{\rm e}\rangle$ of the ejecta are tabulated in Tab. 3.1. It is worth mentioning that these systematic simulations have slight modifications and improvements compared to the previously discussed simulation

of a 1.35-1.35$M_\odot$ BNS merger with neutrinos[2]. As a consequence, apart from the common statistical fluctuations, these simulations are not expected to produce the exact same values of remnant properties or ejecta quantities. Minor variations in different quantities are unavoidable.

Due to the high computational cost, all simulations are run only until $\sim$ 15 ms after the merger, and in some cases with DD2 EOS, they are run longer up to $\sim$ 20 ms after the merger. For all the merger models listed in Tab. 3.1, we do not find a collapse into a BH except for the SFHo EOS with a total mass of $2.9M_\odot$, which promptly collapses to a BH since it exceeds the threshold mass limit (we refer to [34, 33] for an elaborate discussion on the threshold mass values for various EOSs).

3.2.1. Merger dynamics and remnant properties

Throughout this section, we follow the convention that we show the simulations using the SFHo EOS in the left column panels and the simulations using the DD2 EOS in the right column panels. As discussed in Sec. 1.5, it is widely known that SFHo EOS being softer than DD2 produces more compact remnants with higher densities, higher temperatures, higher GW frequencies, higher luminosities and higher ejecta mass. Since the properties of simulations with different EOSs have been widely discussed in many previous works in the literature [24, 217], we do not discuss in detail the comparison of the remnant properties based on the softness or stiffness of different EOSs.

We present the results of our simulations with particular emphasis on the dependence of the mass ratio and the total mass. Looking at the high-density central part of the remnant, for a given total mass, in simulations where the BNS merger remnant does not collapse into a BH, a rotating double-core structure is formed and undergoes strong oscillations in the postmerger phase. As the cores merge, the maximum density of the central core increases with each cycle of the oscillation and eventually approaches a plateau within tens of milliseconds. From Figs. 3.5(a) and 3.5(b), for models using the same EOS (either the left column panels for SFHO EOS or the right column panels for DD2 EOS), the rate at which the maximum density increases appears to depend on the mass ratio of the BNS system. This is understandable since the maximum density of the heavy partner in an asymmetric BNS system starts at a density comparatively higher than that of the one with symmetric binary masses. Consequently, it quickly reaches relatively higher possible values and follows an approximate plateau where the comparative changes in the maximum density become small. Hence, we find that the maximum densities in the remnants of asymmetric mergers achieve an approximate plateau faster than their symmetric counterparts.

Another quantity of importance that is tightly correlated with the high-density central region of a BNS merger remnant is the GW signal. With regard to GW

[2]Unlike the neutrino simulation discussed in Sec. 3.1, to better assess the properties of the ejected material, we do not restrict the smoothing length of each SPH particle to a maximum of $\sim$ 150 km (Sec. 2.1) but rather allow it to spread up to a length of 0.75 times the distance of this particle from the coordinate centre.

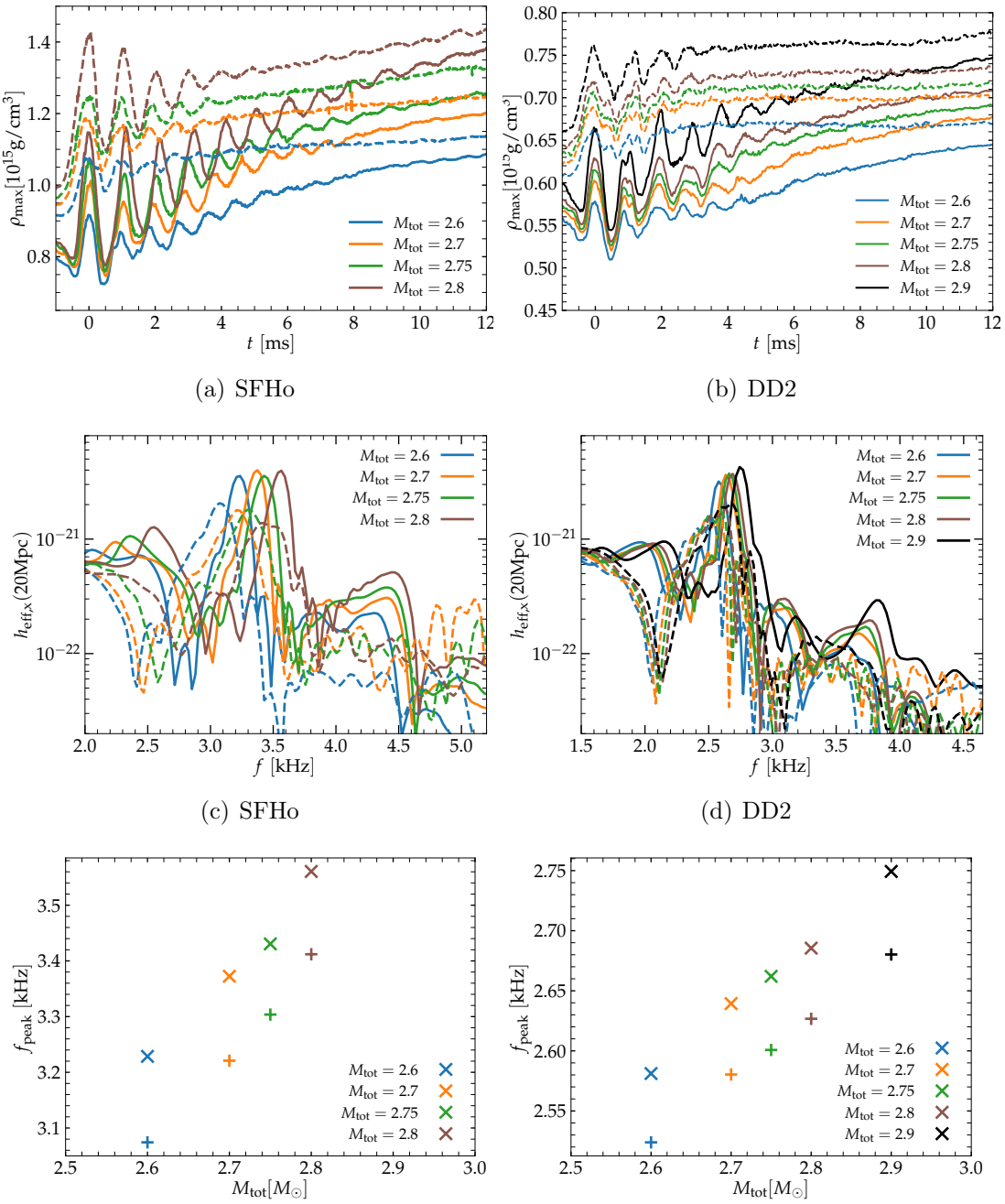

(a) SFHo (b) DD2

(c) SFHo (d) DD2

(e) SFHo (f) DD2

Figure 3.5: Time evolution of the maximum baryonic rest-mass density (top panel), cross-polarisation amplitude of the GW spectra for an observer at 20 Mpc along the polar axis (middle panel), and the dominant postmerger GW oscillation frequency with respect to the total mass of the binary system (bottom panel) for BNS systems using SFHo EOS (left column panels) and DD2 EOS (right column panels). Symmetric models are indicated by solid lines, and asymmetric models are indicated by dashed lines. The dominant postmerger oscillation frequencies are indicated by crosses for symmetric mergers and by plus signs for asymmetric mergers. The time zero corresponds to the instant of maximum compression during the first bounce after merging (minimum in the lapse function), defined as in [278].

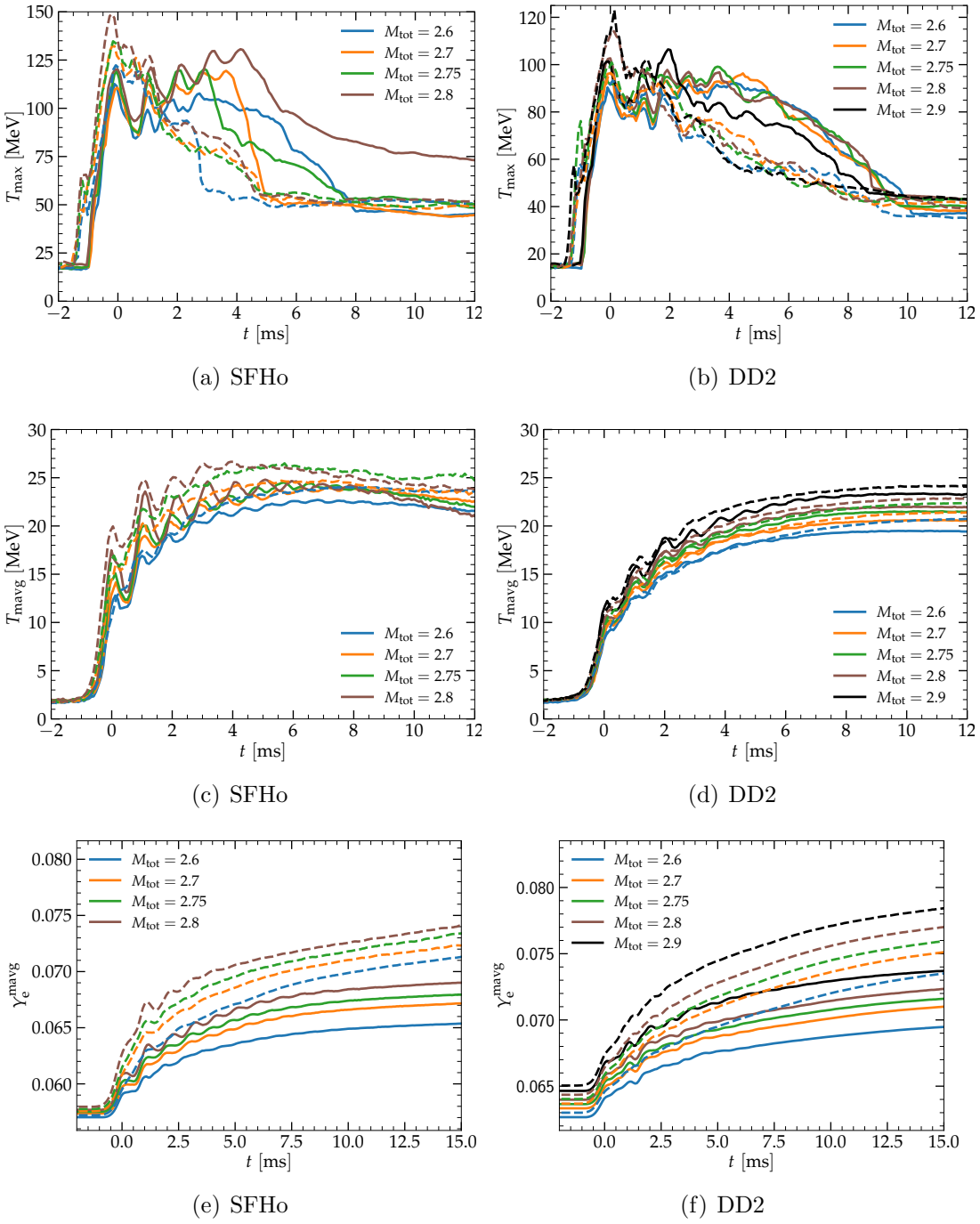

(a) SFHo (b) DD2

(c) SFHo (d) DD2

(e) SFHo (f) DD2

Figure 3.6: Time evolution of the maximum temperature (top panel), the mass-averaged temperature (middle panel) and the mass-averaged electron fraction (bottom panel) for BNS systems using SFHo EOS (left column panels) and DD2 EOS (right column panels). Symmetric models are indicated by solid lines, and asymmetric models are indicated by dashed lines. The time zero corresponds to the instant of maximum compression during the first bounce after merging (minimum in the lapse function).

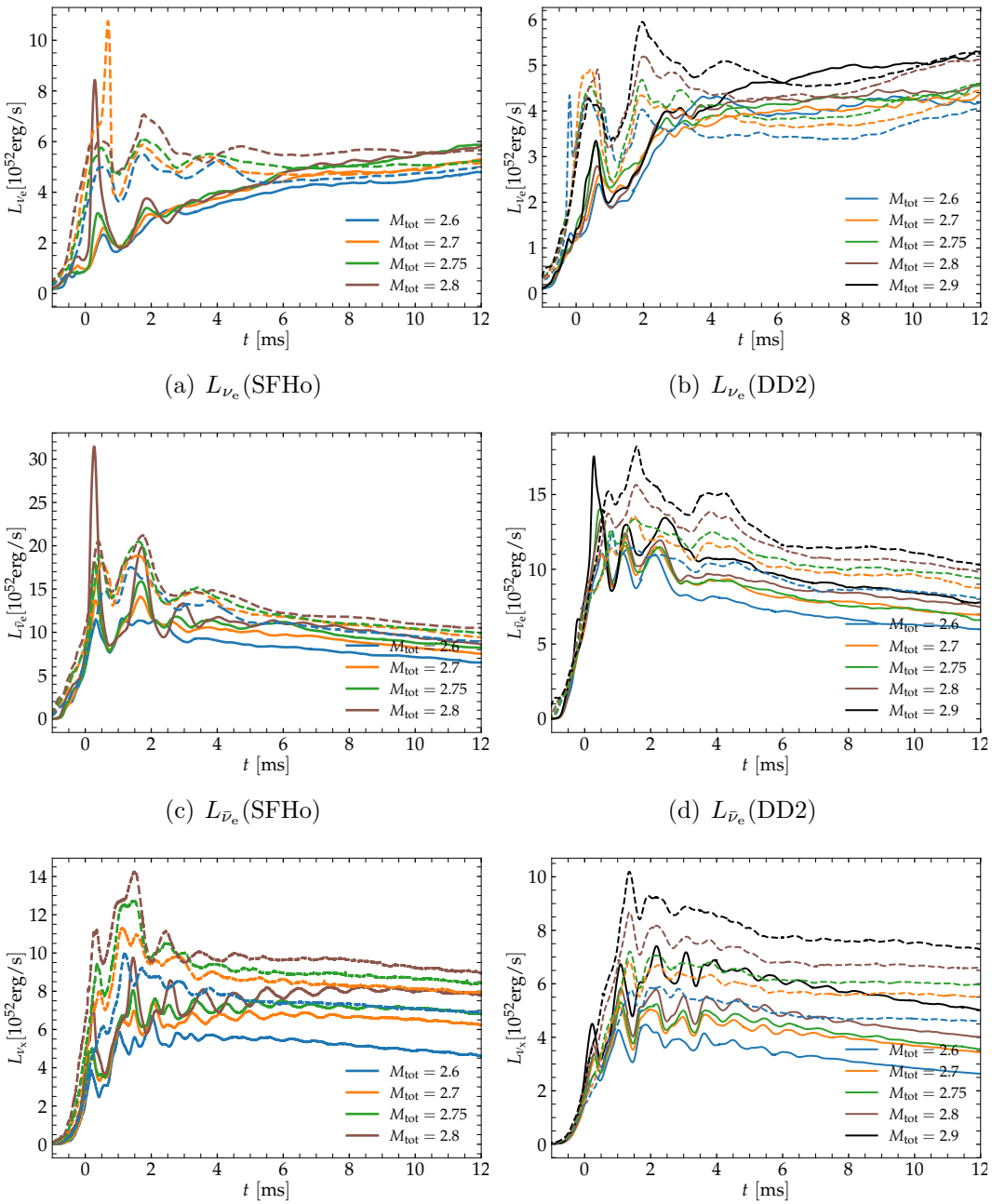

(a) L_{ν_e}(SFHo) (b) L_{ν_e}(DD2)

(c) $L_{\bar{\nu}_e}$(SFHo) (d) $L_{\bar{\nu}_e}$(DD2)

(e) L_{ν_x}(SFHo) (f) L_{ν_x}(DD2)

Figure 3.7: Time evolution of the electron neutrino luminosity (top panel), electron antineutrino luminosity (middle panel) and the heavy lepton neutrino luminosity (bottom panel) for BNS systems using SFHo EOS (left column panels) and DD2 EOS (right column panels). Symmetric models are indicated by solid lines, and asymmetric models are indicated by dashed lines. The time zero corresponds to the instant of maximum compression during the first bounce after merging (minimum in the lapse function).

emission, there exists a single dominant post-merger frequency that reflects the dominant oscillation mode of the central remnant known as the $f_{\rm peak}$ (as discussed in Sec. 1.5). This dominant post-merger oscillation frequency is known to scale tightly with the NS radii, the tidal deformability, $\rho_{\rm max}$ and other NS parameters [27, 26, 264, 41, 29, 43]. More discussion on these empirical relations is also given in Sec. 4.3.3. In Figs. 3.5(c) and 3.5(d), we show the amplitude of the post-merger GW spectra for an observer at 20 Mpc along the polar axis, for all our BNS merger simulations that do not collapse to a BH. Looking at these figures, we find that this dominant oscillation frequency systematically increases with the total mass of the binary and shifts to lower values with a decrease in the mass ratio (as shown in Figs. 3.5(e) and 3.5(f)). We hypothesise that for a given total mass, the central neutron star remnant formed in asymmetric mergers is less massive because of the increased production of ejecta mass (which will be discussed in the following) and leads to a decrease in the angular momentum profile. In addition, the merger occurs at a larger orbital separation because of the larger tidal deformabilities involved in asymmetric mergers. Thus, both the larger tidal deformabilities and the overall lower angular momentum involved in asymmetric mergers result in a decrease in the energy and angular momentum released by gravitational radiation, and a decrease in GW frequencies.

Regarding neutrinos, the production of neutrinos in the merger remnant is strongly dependent on local temperature values. In Fig. 3.6, we show the maximum and the mass-averaged temperatures for simulations using the SFHo EOS (left columns) and the DD2 EOS (right columns). Both the maximum value (Figs. 3.6(a) and 3.6(b)) and the average value (Figs. 3.6(c) and 3.6(d)) of the temperature are found to increase for systems with a larger total mass and greater asymmetry in the mass ratio. This is related to the fact that the increase in the total mass of the merger system leads to more violent collisions that produce larger temperatures, while the asymmetry in the mergers produces larger temperatures from larger tidal disruptions. Also, we observe that the maximum temperatures in asymmetric mergers seem to cool down faster[3] than the maximum temperatures in symmetric mergers, and reach about the same values at the end of the simulation. We note that the number of particles in the high-density regime of the merger remnant is comparatively much larger than the total number of ejected particles. For this reason, the mass-averaged values of any quantity with respect to the whole merger system are always mainly dominated by the higher abundance of particles in the central remnant.

The higher overall temperatures produced within the remnants of asymmetric mergers lead to increased neutrinos production and an overall increase in the values of $Y_{\rm e}$. In Figs. 3.6(e) and 3.6(f), we show the mass-averaged electron fraction weighted over all particles and indeed find that asymmetric mergers produce an overall increase in the mass-averaged $Y_{\rm e}$ values compared to symmetric mergers. In Fig. 3.7, we show the electron neutrino luminosity (top panels), electron antineutrino luminosity (middle panels), and heavy-lepton neutrino luminosity (bottom panels) for models using SFHo EOS (left column) and DD2 EOS (right column).

[3]We caution that these maximum temperatures are calculated on the SPH particle level and are very susceptible to resolution dependencies (see the discussion in Sec. 4.3.1 and Fig. 4.15).

We observe luminosities in asymmetric mergers that are comparatively higher than those of symmetric mergers within the first few milliseconds after the merger. At later times, this difference seems to get smaller and, in many cases, overlap each other within the end of our simulation period. We relate this trend to the initial offset of central densities and temperatures to higher values in asymmetric mergers compared to their symmetric counterparts (Figs. 3.5 and 3.6). The same trends are also observed with increasing total mass. As the merger evolution progresses to later times, both the densities and the temperatures reach a plateau independent of the mass ratio; consequently, these trends seem to disappear gradually. Interestingly, we observe a hierarchy in the neutrino luminosity values $L_{\bar{\nu}_e} > L_{\nu_x} \geq L_{\nu_e}$ (consistent with the findings in [16]) and find it to be preserved independent of the total mass and the mass ratio in most of our BNS merger simulations within the first few milliseconds.

3.2.2. Ejecta properties

The primary mechanisms by which dynamical mass ejection occurs in BNS mergers are shock heating and the tidal torque by the hyper massive neutron star (HMNS) remnant [92, 252]. Shock heating which produces higher temperatures and the subsequent increase in neutrino irradiation in the merger remnant generally increase Y_e for a large fraction of the ejecta. However, all the ejected particles from the HMNS merger remnant do not always undergo weak interaction. Specifically, if the matter is ejected from regions of the merger remnant where the effects of weak interaction are not significant and less neutrino irradiation is present, i.e. far away from the central remnant, the Y_e value of these ejected particles does not evolve much (from Eq. 2.18). Consequently, a large fraction of the ejecta can retain its low Y_e values from cold neutrinoless β-equilibrium conditions (see Fig. 4.7) and maintain the neutron richness of the ejecta. As a result, the dynamical ejecta from BNS mergers broadly consists of components with a wide range of Y_e values from its initial low β-equilibrium values up to and above ~ 0.5.

From Figs. 3.8(a) and 3.8(b), it is quite clear that the simulation with a higher total mass and a higher mass ratio produces a larger amount of ejecta. In addition, higher temperature distributions and the larger amount of neutrinos involved in the asymmetric merger can cause the ejecta to be more spherical. To obtain a measure of the sphericity of the ejecta distribution, we define a quantity $\left(\frac{M_{\rm pol}}{M_{\rm eq}}\right)^{\rm ej}$ that calculates the total mass of the ejecta within a polar angle of 45 degrees about the north and south poles and the total mass of the ejecta within 90 degrees around the equatorial direction. $M_{\rm pol}$ is the total mass of the ejecta per unit solid angle from the polar angle $0^\circ - 45^\circ$ and $135^\circ - 180^\circ$, $M_{\rm eq}$ is the total mass of the ejecta per unit of solid angle from the polar angle $45^\circ - 135^\circ$. From Figs. 3.8(c) and 3.8(d), it is seen that binary systems with larger asymmetry produce a more spherical ejecta distribution than symmetric BNS systems within the first few milliseconds after the merger.

To separately take into account the Y_e distribution of only the ejected mass, we show the mass distribution of the ejecta based on the bin Y_e values in Figs. 3.9(a) and 3.9(b), and the angular mass distribution based on the bin Y_e values in

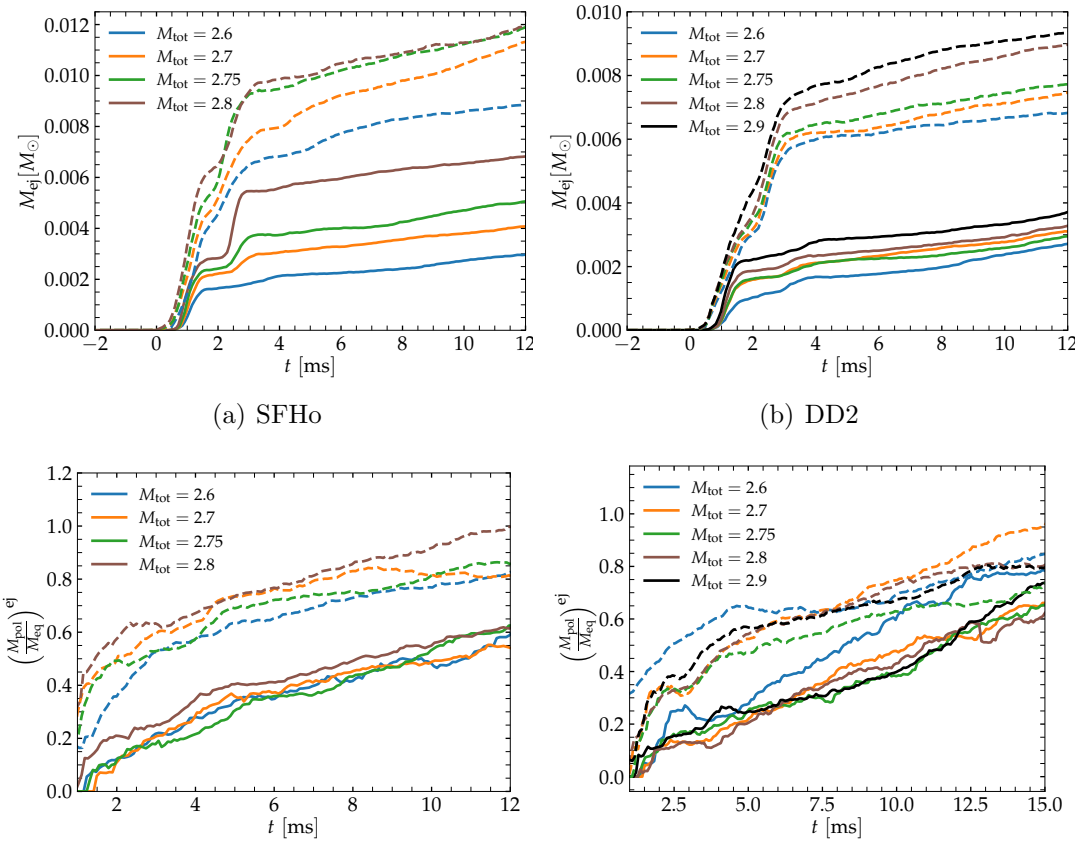

(a) SFHo (b) DD2

(c) SFHo (d) DD2

Figure 3.8: Time evolution of the ejecta mass and the ratio of the ejecta mass per unit solid angle along the poles ($0^\circ < \theta < 45^\circ$ and $135^\circ < \theta < 180^\circ$) and about the equator ($45^\circ < \theta < 135^\circ$), $\left(\frac{M_{\rm pol}}{M_{\rm eq}}\right)^{\rm ej}$, for BNS mergers using SFHo EOS (left column panels) and DD2 EOS (right column panels). Symmetric models are indicated by solid lines, and asymmetric models are indicated by dashed lines. The time zero corresponds to the instant of maximum compression during the first bounce after merging (minimum in the lapse function).

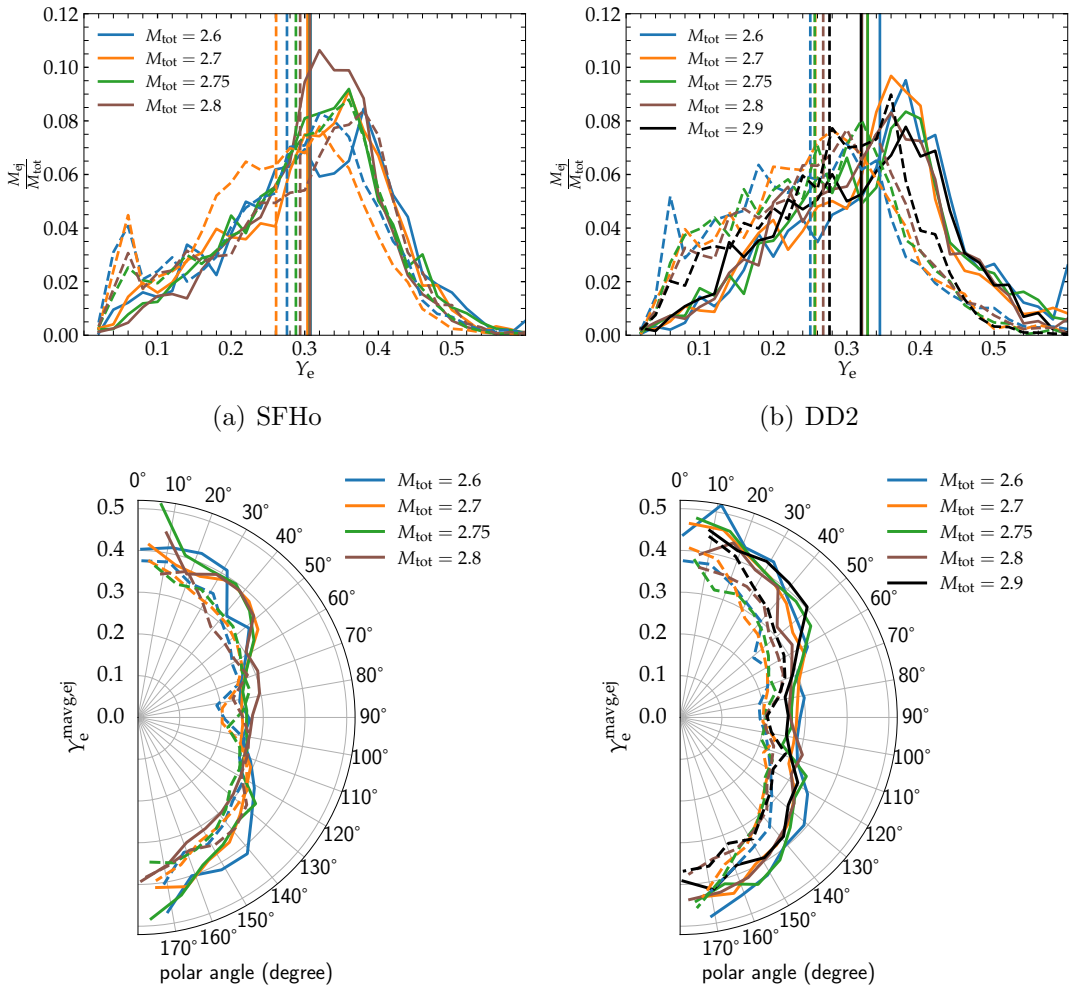

(a) SFHo (b) DD2

(c) SFHo (d) DD2

Figure 3.9: The scaled mass distribution of the ejecta with respect to the electron fraction values (top panel) and the angular distribution of the ejecta mass with respected to the mass-averaged electron fraction values for each angular bin (bottom panel), for BNS systems using SFHo EOS (left column panels) and DD2 EOS (right column panels). Symmetric models are indicated by solid lines, and asymmetric models are indicated by dashed lines. The vertical lines represent the weighted average of the distribution and give a rough estimate on how the distribution is shifted from one simulation to another.

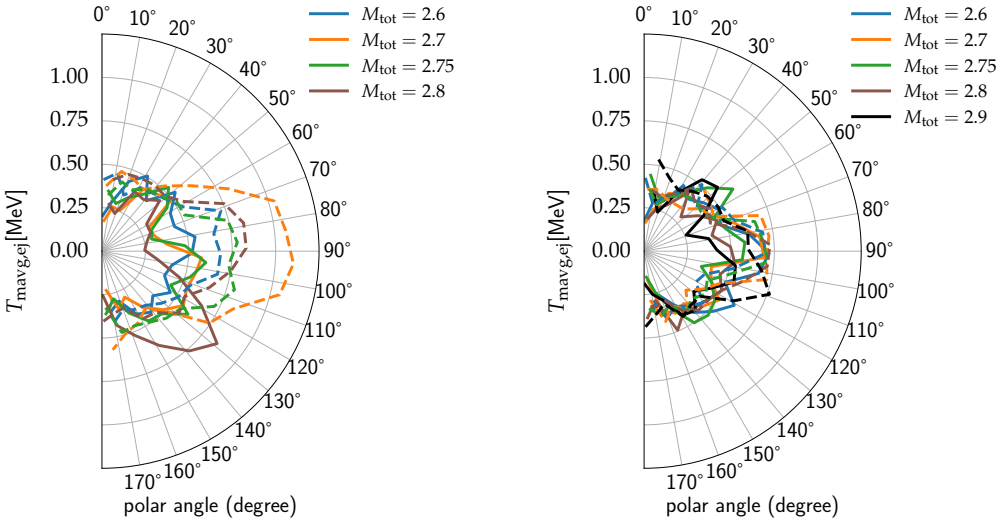

(a) SFHo (b) DD2

Figure 3.10: The angular distribution of the mass-averaged temperature of ejected particles within each angular bin, for BNS mergers using SFHo EOS (left column panels) and DD2 EOS (right column panels). Symmetric models are indicated by solid lines, and asymmetric models are indicated by dashed lines.

Figs. 3.9(c) and 3.9(d). Note that, from the discussions in Sec. 3.1, considering the complications involved in plotting histograms for a large number of simulations and for better visualisation, we plot the data bins with lines instead of histograms. Since the total ejecta mass varies a lot from one simulation to another, considering different total mass and mass ratio, we scale the mass distribution to the total ejected mass of the system. The vertical lines represent the weighted average of the distribution and give a rough estimate on how the distribution is shifted from one simulation to another.

Unlike our previous finding on the trend of total mass-averaged $Y_{\rm e}$ values, which attain higher values in asymmetric mergers, we actually find that the whole distribution of $Y_{\rm e}$ with respect to the ejecta mass is shifted to lower values (indicated by the vertical lines in Figs. 3.9(a) and 3.9(b)). The same trend is also observed by looking at the angular distribution of $Y_{\rm e}$ in different angular bins (Figs. 3.9(c) and 3.9(d)). This is consistent with the results of [248, 92, 217, 182, 40], where they also find a shift in the distribution of $Y_{\rm e}$ to lower values in their ejecta composition.

However, despite the shift of the $Y_{\rm e}$ distribution to lower values, we do not find a systematic decrease in ejecta temperatures, but rather find that the mass-averaged ejecta temperatures increase for each polar angle in asymmetric mergers (see Figs. 3.10(a) and 3.10(b)). We also observe that this change in the distribution of $Y_{\rm e}$ to lower values is related to the larger ejecta mass produced from the larger radii of the central merger remnant. Since the luminosity of neutrino irradiation decreases with distance, particles that are ejected from farther distances of the central remnant do not evolve much from their original beta-equilibrium values of $Y_{\rm e}$. As a result, the overall distribution of the ejecta mass shifts to lower $Y_{\rm e}$

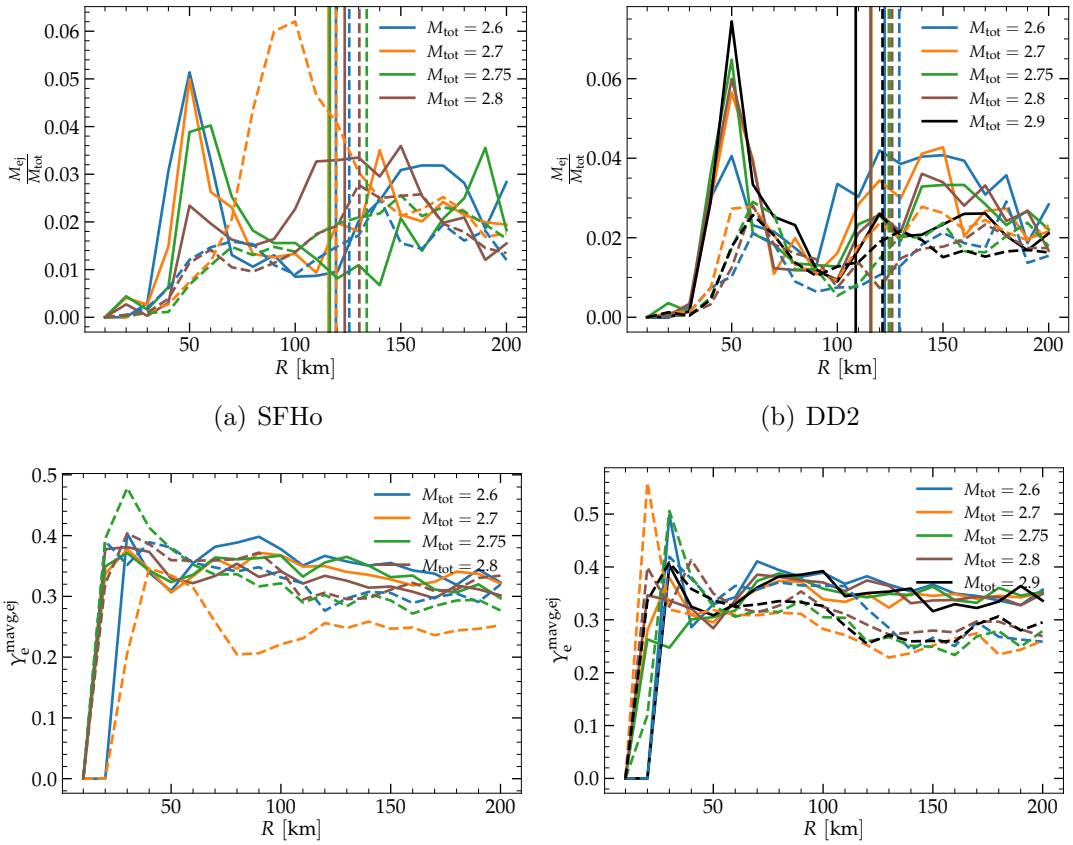

(a) SFHo (b) DD2

(c) SFHo (d) DD2

Figure 3.11: The scaled ejecta mass distribution based on the radial position of all the ejected particles at about 10 milliseconds after the merger (top panel) and the corresponding mass-averaged $Y_{\rm e}$ values in each of these radial positions, for BNS mergers using SFHo EOS (left column panels) and DD2 EOS (right column panels). Symmetric models are indicated by solid lines, and asymmetric models are indicated by dashed lines. The vertical lines represent the weighted average of the distribution and give a rough estimate on how the distribution is shifted from one simulation to another.

values independent of the temperature distribution of the merger ejecta. This is seen in Figs. 3.11(a) and 3.11(b), where the positions of the ejected particles are binned in different radius bins by calculating the trajectories of each ejected particle and trace them backward in time to find the originating radial positions at about 10 milliseconds after the merger. We see a clear shift in the average radial position (indicated by vertical lines) to larger radii with a pattern similar to that observed in the neutrino-richness of the ejecta. Using the same radial positions and calculating the corresponding mass-averaged values of $Y_{\rm e}$, we again find a consistent shift of $Y_{\rm e}$ to lower values in asymmetric mergers, shown in Figs. 3.11(c) and 3.11(d). Thus, we find that the neutron-richness of the dynamical ejecta is higher for merger systems with larger asymmetry compared to symmetric BNS systems, and is mainly caused by the increase in the number of particles ejected

from farther radii of the central merger remnant.

Declaration

The whole part of this chapter with the corresponding Appendix. C and the conclusions are all based on the work **"Impact of pions on binary neutron star mergers"**, Vimal Vijayan, Ninoy Rahman, Andreas Bauswein, Gabriel Martínez-Pinedo and Ignacio L. Arbina, published in *Phys. Rev. D* 108, 023020, on July 2023. The text, figures, and tables have been adapted to suit this thesis.

4. Impact of pions on binary neutron star mergers

The EOS for high-density matter plays a crucial role in shaping the structure of NSs and influencing the behaviour of BNS mergers and their outcome. The incompleteness of our understanding of the EOS of NS matter prompts the proposals of various theoretical models along with the efforts to obtain insights from observations of, for instance, BNS mergers. These theoretical models employ diverse approaches to tackle the complex nuclear many-body problem and require distinct assumptions regarding the components of high-density matter, e.g. [140, 196, 37, 220, 209, 219, 129]. In addition to neutrons, protons, and electrons, certain models also incorporate other particles, including hyperons, deconfined quarks, muons, quarks, pions, kaons, and, at finite temperatures, positrons, photons, neutrinos, and anti-neutrinos. The finite-temperature regime of the EOS is especially relevant for phenomena such as core-collapse supernovae and binary neutron star mergers, where temperatures can reach several 10 MeV, as discussed in the reviews above.

For decades it has been speculated that negatively charged pions could form a Bose-Einstein condensate in the cores of NSs [242, 164, 36, 285, 20, 165, 75, 166, 10]. However, the occurrence and density at which such a condensate forms depend on the detailed interactions between pions and nucleons, which are currently unknown. It is anticipated that pions are influenced by an effective pion mass that deviates from its vacuum value of approximately 140 MeV. At finite temperature, it gives rise to the possibility of the presence of a thermal pion population, that encompasses positively and negatively charged pions, as well as neutral pions [156, 111, 179, 180, 195, 208, 81].

The impact of pions in the context of BNS mergers, whether in the form of a condensate or as part of a thermal population, remains largely unexplored. But see refs [179, 180, 208], which investigate pions in simulations of core-collapse supernovae. In fact, currently only a limited number of temperature-dependent EOS tables are available for astrophysical applications that incorporate pions [111, 195, 243, 81]. These calculations indicate that the inclusion of pions in the models leads to a softening of the EOS compared to models without pions, as they primarily alter the proton fraction in the system.

In this study, we provide a first assessment of the potential influence of pions within BNS merger simulations. We adopt a relatively simple model characterising pions as a non-interacting Bose gas with a chosen effective mass, and by this we

consider both a condensate and a thermal population of pions. We incorporate the pion contributions into existing EOS tables and calculate properties of isolated NSs under conditions of neutrinoless beta-equilibrium at zero temperature. We then focus on the impact in dynamical simulations of BNS mergers and analyse the influence of pions on the dynamics, on BH formation, on the GW signal, and on the mass ejection in these events.

A primary objective of this exploration is to assess the degree to which neglecting pions in prior studies influences empirical relations for the dominant postmerger GW frequency and the threshold mass for prompt BH formation, e.g. [26, 27, 24, 108, 30, 41, 264, 223, 143, 133, 46, 274, 9, 43, 280, 33, 271, 125, 132]. These relationships have been established based on calculations that do not incorporate pions[1] and, partly, they are already employed to interpret observations and to infer EOS information, or they may be used in future measurements.

We observe that the majority of empirical relationships continue to hold true for models that incorporate pions, despite the fact that these relationships were originally established based on calculations that did not consider pions. These relationships establish connections between the characteristics of isolated, cold, non-rotating neutron stars and the observable properties of the merger. Since the inclusion of pions affects both the properties of isolated stars and the merger itself, these empirical relationships are not too much affected for the range of chosen effective pion masses in this study. It is assumed that the values of the effective pion masses used here somewhat encompass a reasonable spectrum and capture the more complicated physics of pions in the dense environment of NSs [221, 117, 272, 82, 80], which we do not include here. Based on these findings, we conclude that it is relatively safe to employ such relations in existing and future studies.

4.1. Pionic equation of state

In this section, we elaborate on our approach to incorporating pions into an existing non-pionic EOS. The tabulated SFHo EOS [105, 104, 262] and the DD2 EOS [275, 105, 276] are used in this study as base EOSs. These EOSs include neutrons, protons, light nuclei (deuterium, tritium, ^{3}He, etc.), alpha particles, heavy nuclei (charge number $Z \geq 6$), electrons, and positron as their constituents. They assume nuclear statistical equilibrium (NSE) across a wide range of density and temperature. The base non-pionic EOSs provide tabulated data for various thermodynamic quantities as functions of baryonic density ρ, temperature T, and number fraction of positively charged particles Y_p. It is worth noting that in the absence of pions, the net electron fraction $Y_\mathrm{e} = Y_{\mathrm{e}^-} - Y_{\mathrm{e}^+}$ is equal to Y_p, where Y_{e^-}, Y_{e^+} represent the number fractions of electrons and positrons, respectively.

The vacuum rest masses of the charged pions π^-, π^+ and the neutral pion π^0 are given by $m_{\pi^\pm}$ =139.57039 MeV and m_{π^0} =134.9768 MeV [200]. We treat

[1] Some of these studies do include a few models with pions such as the APR EOS [11, 243]. However, most of the EOS models in use disregard the presence of pions. Consequently, the models incorporating pions have a minimal influence on the resulting fits. For simplicity, in the following discussion, we will refer to these empirical relations as derived from models without pions.

pions as a free non-interacting Bose gas and assume that their masses do not change with baryonic density. For extensive discussions on the variation in pion mass in dense medium, see [186, 117, 272, 80]. We also assume that pions are in thermal and chemical equilibrium with nucleons due to the strong interaction. Therefore, the chemical potentials of the pions follow $\mu_{\pi^\pm} = \mp(\mu_\mathrm{n} - \mu_\mathrm{p})$ and $\mu_{\pi^0} = 0$, where μ_n, μ_p, μ_{π^-}, μ_{π^+}, and μ_{π^0} are the chemical potentials of neutrons, protons, negatively charged pions, positively charged pions, and neutral pions, respectively. Given our assumption that pions are a non-interacting Bose gas, it follows that the chemical potential of negatively charged pions should be either equal to or smaller than their vacuum rest mass. Additionally, charge neutrality requires $Y_\mathrm{p} = Y_\mathrm{e} + Y_\pi = Y_\mathrm{e} + Y_{\pi^-} - Y_{\pi^+}$, where Y_π represents the net number fraction of charged pions, while Y_{π^-} and Y_{π^+} are the number fraction of negatively charged pions and positively charged pions, respectively.

To incorporate charged pions into the base EOS, we apply the following procedure. For a given baryonic density ρ, temperature T, and net electron fraction Y_e, we iteratively determine Y_p until charge neutrality $Y_\mathrm{p} - Y_\pi = Y_\mathrm{e}$ is satisfied. The base EOS provides $\hat{\mu} = \mu_\mathrm{n} - \mu_\mathrm{p}$, and if $|\hat{\mu}| < m_{\pi^\pm}$, we calculate the net number fraction of pions Y_π using Bose-Einstein statistics, with given T, and $\mu_{\pi^\pm} = \pm\hat{\mu}$ in each iteration.

In a neutron-rich environment when $Y_\mathrm{p} < 0.5$, the base EOS can yield $\hat{\mu} > m_{\pi^-}$, where the chemical potential difference between neutrons and protons can exceed the rest mass of negatively charged pions. However, the maximum allowed value for the chemical potential of negatively charged pions, denoted as $\mu_{\pi^-}^\mathrm{max}$, corresponds to their rest mass, as pions behave as a Bose gas. Under such thermodynamic conditions when $\hat{\mu} > m_{\pi^-}$, the negatively charged pions can form the Bose-Einstein condensate which, unlike thermal pions, has zero kinetic energy. In such conditions, we iteratively solve for a new value of Y_p using $\hat{\mu} = \mu_{\pi^-}^\mathrm{max} = m_{\pi^-}$, under fixed baryonic density, temperature, and electron fraction. Subsequently, we employ the charge neutrality condition to obtain the number fraction of negatively charged condensed pions $Y_\pi^\mathrm{c} = Y_\mathrm{p} - Y_\mathrm{e} - Y_\pi^\mathrm{thermal}$, where the number fraction of thermal pions Y_π^thermal is evaluated from the Bose-Einstein statistics with $\mu_{\pi^-} = m_{\pi^-}$.

This condensed portion of negatively charged pions does not contribute to the total pressure and the total thermal energy. Under certain proton-rich conditions, it is conceivable for a condensate of positively charged pions to develop. However, such scenarios are generally not anticipated in the context of zero-temperature β-equilibrium NSs and HMNSs. It is straightforward to calculate the number fraction of neutral pions since their production depends only on the temperature of the Bose gas. In the end, we combine everything and determine the net contribution of pions to the pressure, the internal energy, and the total entropy per baryon using the Bose-Einstein statistics.

We note that the base SFHo and DD2 EOSs employed in this study include the electronic contributions corresponding to $Y_\mathrm{e} = Y_\mathrm{p}$ in the total pressure, the total energy, and the total entropy of the gas, and they tabulate these thermodynamic quantities against ρ, T, and Y_p. Hence, when constructing our modified EOSs to include pions, which tabulate thermodynamic quantities as a function

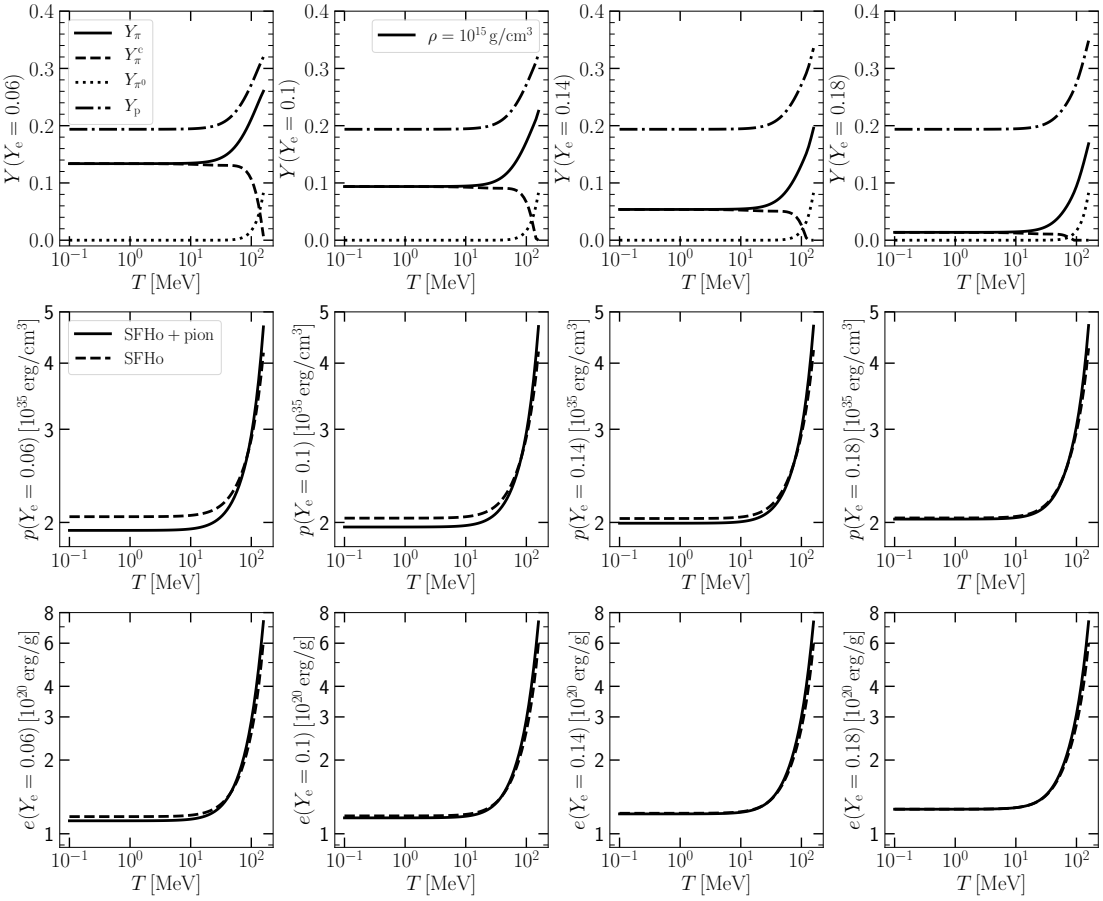

Figure 4.1: Comparison between the SFHo EOS and the modified SFHo EOS with pion masses equal to their vacuum values at a baryon density of $10^{15}\,\mathrm{g/cm^3}$. The net number fraction of charged pions (solid lines) and number fraction of condensed negative pions (dashed lines), neutral pions (dotted lines), and positive charges (dotted-dashed lines) are shown in the top row. The total pressure and total specific internal energy are shown for the SFHo EOS (dashed lines) and the modified SFHo EOS with pions (solid lines) in the second and third rows, respectively. Different columns represent different electron fractions. Taken from [278].

of ρ, T, and Y_e with $Y_e \neq Y_p$, we first subtract the electronic contributions corresponding to $Y_p = Y_e + Y_\pi$ from the total pressure, the total energy, and the total entropy, and then we add the electronic contributions corresponding to Y_e to the total pressure, the total energy, and the total entropy of the gas.

The base EOS takes into account the Coulomb interactions between charged particles and includes their respective contributions to the pressure, the internal energy, and the proton chemical potential. Since the mean separation length between positive charges and pions can be smaller than the mean separation length between positive charges and electrons, the Coulomb contributions for pions can differ from the ones that correspond to electrons. Despite that, we refrain from making modifications to these contributions in thermodynamic quantities within the scope of this study, which constitutes a limitation of our approach. However, at densities above the nuclear saturation density, which is the most relevant for pion production, the nuclear contributions dominate over the Coulomb contributions. Therefore, our approximation regarding the Coulomb interactions is expected to have a minor impact on the structure of NSs and the GWs emitted during merger, which are the two main topics of this chapter.

In a dense medium, it is also possible for the effective mass of the pion to vary with baryon density, temperature, and composition, due to the pion-pion interaction and the pion-nucleon interaction (see, e.g., [186, 117, 272, 80]). Reference [80] has shown a considerable increase in the mass of negatively charged pions at densities above saturation density and zero temperature. However, further studies are required to provide a clear understanding on the behavior of pions at typical temperatures of a few 10 MeV, which is relevant for postmerger remnants. To probe the consequences of the effective pion mass variation on the various thermodynamic quantities, we construct our pionic EOSs with different constant effective pion masses. For simplicity, we use three different fixed pion masses by adopting the vacuum mass, 170 MeV, and 200 MeV and assume that the neutral and charged pions have the same masses. As we have already pointed out, positively charged pions are significantly suppressed under the relevant conditions. Therefore, we do not anticipate substantial effects from a potential mass splitting between negatively and positively charged pions. Although our approach may not account for all the intricacies of how the dense medium can influence the pionic EOS (see, e.g., [221, 151, 82, 80] for discussions about the medium modification of pionic EOSs), it provides a simple way to examine the potential impact of pion mass variations on BNS mergers.

Throughout this chapter, we consistently adopt the following notation: "SFHo" for the base SFHo EOS, "SFHo+π, m_π = Vac. mass", "SFHo+π, $m_\pi = 170\,\mathrm{MeV}$", "SFHo+$\pi$, $m_\pi = 200\,\mathrm{MeV}$" for SFHo based EOSs that include pions with effective pion masses equal to the vacuum mass, 170 MeV and 200 MeV, respectively. A similar notation is used for models based on DD2.

In Fig. 4.1, we present a comparison between the base SFHo EOS and the modified SFHo EOS, with pion masses equal to their vacuum values at a baryon density of $10^{15}\,\mathrm{g/cm^3}$. The panels display various quantities as functions of gas temperature. The top panels show the net number fraction of the charged pions Y_π (solid lines), the number fraction of the condensed negatively charged pions

$Y_\pi^{\rm c}$ (dashed lines), the neutral pions Y_{π^0} (dotted lines), and the positive charges $Y_{\rm p}$ (dotted-dashed lines). The middle and bottom panels show the total pressure and the specific internal energy, respectively, for the SFHo EOS (dashed lines) and the modified SFHo EOS with pion masses equal to their vacuum values (solid lines). Each column represents different electron fractions, namely $Y_{\rm e} = 0.06$ (first column), 0.1 (second column), 0.14 (third column), and 0.18 (fourth column). These values of the electron fraction, along with a baryon density of $10^{15}\,{\rm g/cm^3}$, are representative of conditions within a HMNS (see, e.g., [249, 143, 88, 217, 16]).

Under these thermodynamic conditions, both the total number fraction of charged pions and the number fraction of condensed negatively charged pions remain constant until a certain threshold temperature $T_{\rm thres}$ is reached. At temperatures below $T_{\rm thres}$, pions exist predominantly in the Bose-Einstein condensate form, where $Y_\pi \approx Y_\pi^{\rm c}$. As the temperature rises beyond $T_{\rm thres}$, an increasing number of pions transition out of the condensate form. Furthermore, the net number fraction of charged pions rises with temperature due to the substantial production of thermal pions, which are characterised by non-zero kinetic energies. We also observe that the threshold temperature increases with increasing baryon density and decreases with increasing electron fraction, as shown in Fig. 4.2, where $T_{\rm thres}$ are marked by crosses for various densities and electron fractions. We approximate $T_{\rm thres}$ as the temperature where the number fraction of condensed negatively charged pions differs by one percent from the net number fraction of charged pions. We also observe that neutral pions are predominantly generated at high temperatures, and their number fraction remains relatively unaffected by the changes in the electron fraction since their chemical potential is assumed to be zero. In contrast, the net number fraction of charged pions decreases as the electron fraction increases. The fraction of positively charged particles follows the charge neutrality condition $Y_{\rm p} = Y_{\rm e} + Y_\pi$. In the neutron-rich conditions illustrated in Fig. 4.1, the π^- are more abundantly produced than π^+, i.e. $Y_\pi > 0$, which leads to $Y_{\rm p} > Y_{\rm e}$. As a result, the inclusion of pion production causes baryonic matter to approach a more symmetric state ($Y_{\rm p} \to 0.5$), which in turn affects the pressure.

The total pressure shown in the middle row of Fig. 4.1 contains contributions from baryons, electrons, positrons, photons for both EOSs and, in addition, includes contributions from thermal charged pions and the neutral pions for the modified SFHo EOS. The bottom panels of Fig. 4.1 display the specific internal energy, which represents the relativistic specific internal energies with the vacuum rest-mass energies of baryons subtracted. This quantity includes contributions from baryons, electrons, positrons, photons, and, if present, from pions. It is worth noting that the condensed negatively charged pions do not contribute to the pressure, as they possess zero kinetic energy, and they only affect the specific internal energies.

At temperatures below several 10 MeV, both the pressure and the specific internal energy of the EOS containing pions are lower compared to those of the base EOS. This difference arises because a fraction of the pions exists in a condensed form, and consequently, they do not contribute to the thermal pressure and thermal energy. The reduction in pressure attributable to pion production is more significant compared to the impact on the specific internal energy. Furthermore,

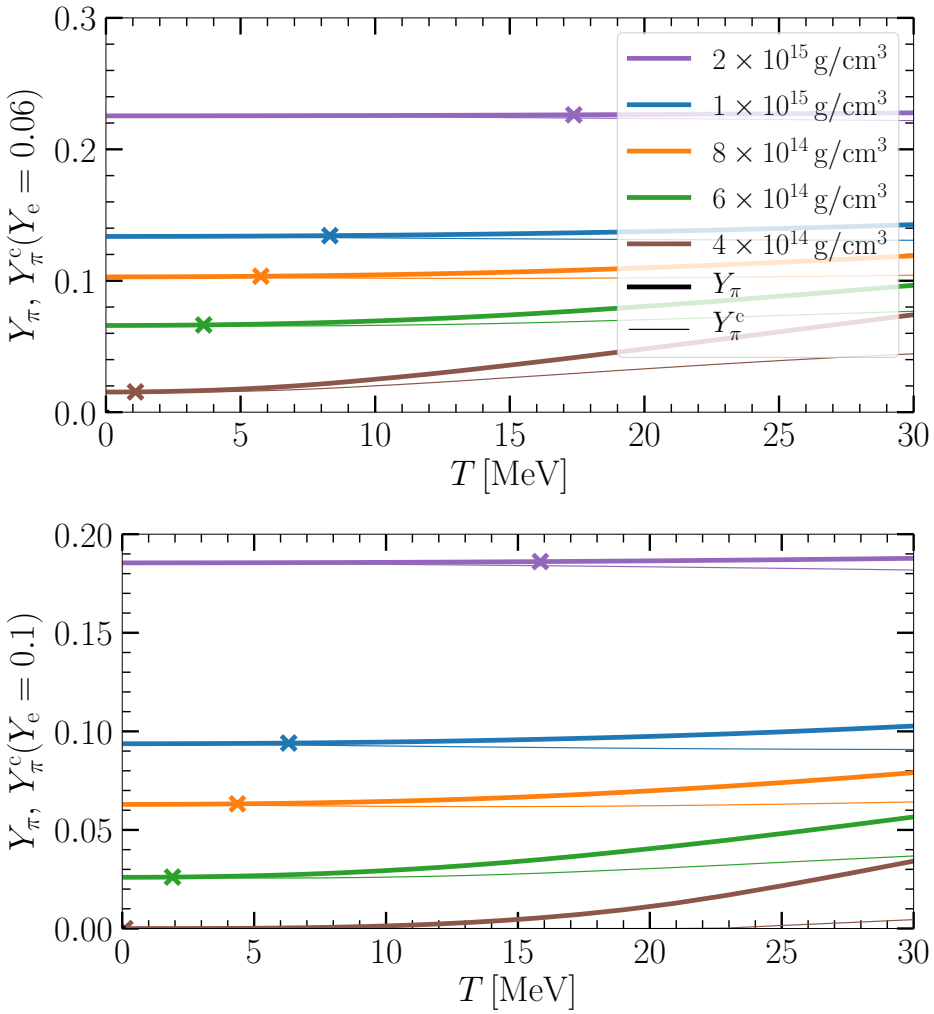

Figure 4.2: Net number fraction of charged pions and number fraction of negative pions in the condensate versus temperature at different densities for the modified SFHo EOS with pion masses equal to their vacuum values. The top panel and the bottom panel show these number fractions at electron fractions of 0.06 and 0.1, respectively. The crosses mark the threshold temperatures. We define these threshold temperatures as the points where the number fraction of negative pions in the condensate differs by one percent from the net number fraction of charged pions. Taken from [278].

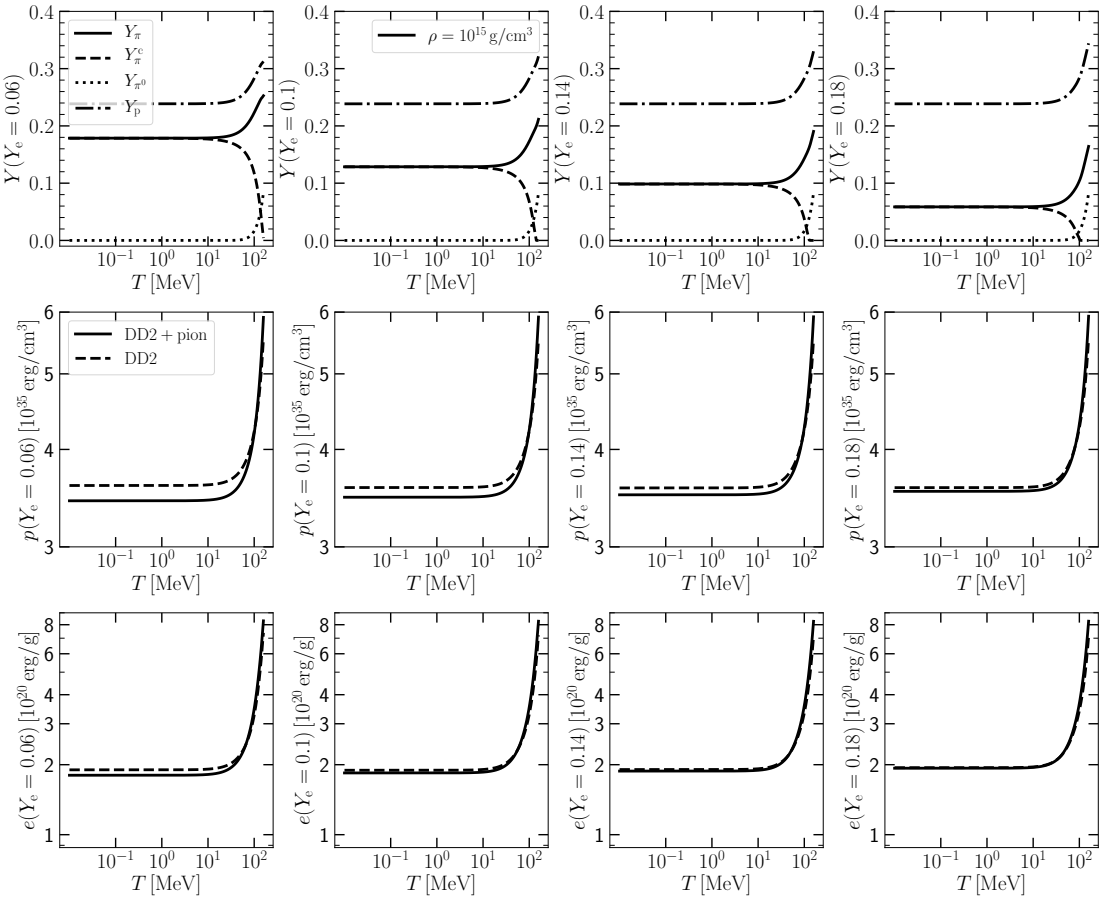

Figure 4.3: Comparison between the DD2 EOS and the modified DD2 EOS with pion masses equal to their vacuum values. Quantities shown here are the same as in Fig. 4.1. Taken from [278].

the disparity between the two EOSs diminishes with a higher electron fraction, primarily due to the reduction in the net number fraction of charged pions.

As the temperature increases and the pions transition out of their condensed form, these reductions in pressure and specific internal energy vanish, and at temperatures above several 10 MeV, the pressure and the specific internal energy of the modified SFHo EOS surpass those of the base SFHo EOS. This is due to the contributions from the thermal charged pions and the neutral pions, which are produced in abundance at high temperatures.

In Fig. 4.3, we show a similar comparison of quantities as in Fig. 4.1, but for the DD2 EOS and the modified DD2 EOS with pion masses equal to their vacuum values. The qualitative trends discussed earlier for the modified SFHo EOS are also evident in the case of the modified DD2 EOS. However, there are some quantitative differences between the modified DD2 EOS and the modified SFHo EOS, which are expected since the underlying base EOSs are different and based on different nuclear models [262, 275, 276].

In Fig. 4.4, we show the total pressures (top panel) and the net number fractions of charged pions (bottom panel) as a function of temperature, at a baryon density of $10^{15}\,\mathrm{g/cm^3}$ and an electron fraction of 0.06 for the SFHo EOS (black lines) and the modified SFHo EOS with different pion masses, including the vacuum masses (blue lines), 170 MeV (orange lines), and 200 MeV (green lines). As the pion masses become larger, the total pressure of the modified SFHo EOSs approaches that of the base EOS. This reduction in the difference in total pressure between the modified SFHo EOSs and the base SFHo EOS is expected because the production of charged pions decreases with increasing pion mass. The decrease in pion production is evident from the shift of the net number fraction of charged pions towards smaller values as the pion masses increase (lower panel). Recently, [80] discusses the density dependence of pion mass at T=0, showing that the negatively charged pion mass can exceed 200 MeV at densities relevant for the pion production, i.e., at densities greater than the nuclear saturation density. In such high-density conditions, the net pion fraction will be extremely small, and the influence of pion production on the total pressure, total energy, and other factors will be negligible. Further research is needed to understand the dependence of pion effective mass on density and temperature, as well as how the energy-momentum dispersion relation of pions changes in a dense medium.

In Fig. 4.5, the net number fraction of charged pions is represented in the baryon density-temperature plane (ρ-T plane) for modified SFHo EOSs with pion masses equal to their vacuum values (top panel), 170 MeV (middle panel), and 200 MeV (bottom panel). Furthermore, the black lines indicate the ratios of the number fraction of condensed charged pions and the net number fraction of charged pions, denoted as Y_π^{c}/Y_π, where Y_π and Y_π^{c} are evaluated under the assumption that the charged pions are in chemical equilibrium with the nucleons and electrons. This gives the condition $\mu_{\pi^-} = \mu_{\mathrm{n}} - \mu_{\mathrm{p}} = \mu_{\mathrm{e}}$, where μ_{e} is the chemical potential of electrons. The $Y_\pi^{\mathrm{c}}/Y_\pi = 0.99$ line corresponds to the threshold temperature T_{thres} (see also Fig. 4.2). From Fig. 4.5, it is evident that for a given temperature, the net number fraction of charged pions generally increases as the baryon density increases. The ratio between Y_π^{c} and Y_π increases with the baryon

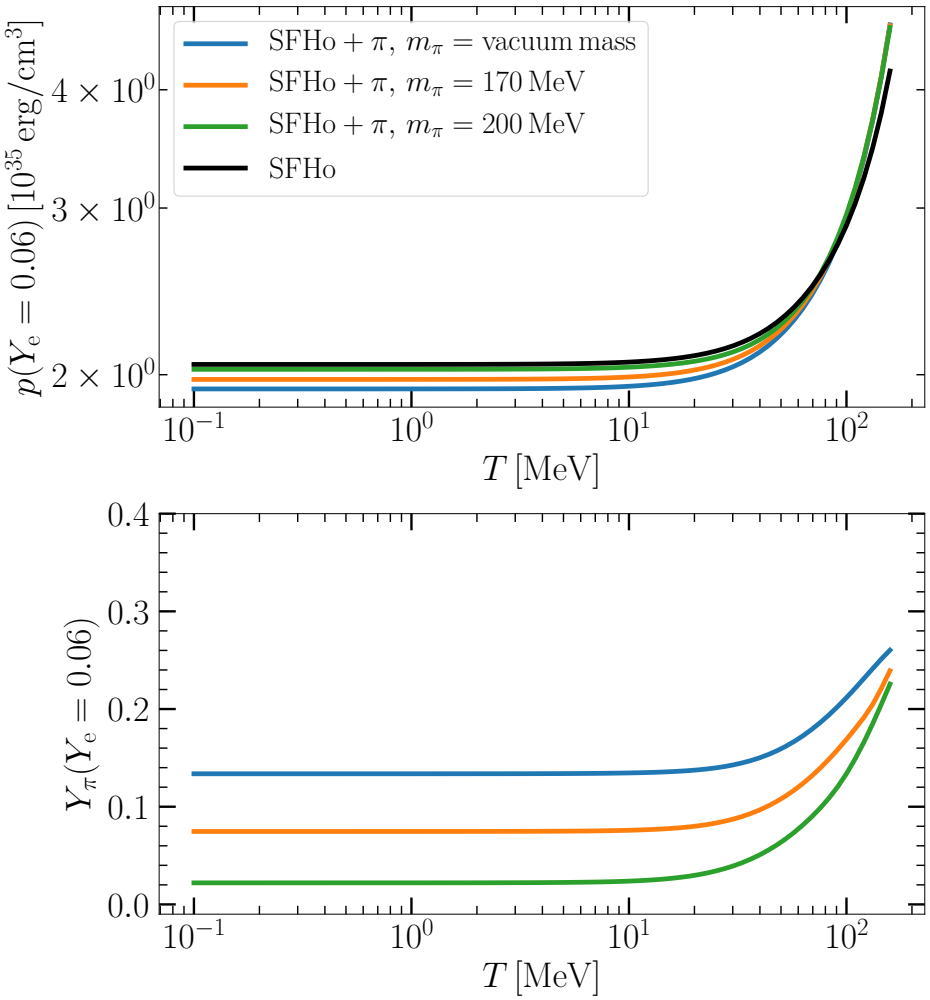

Figure 4.4: Total pressure of matter (top panel) and net number fraction of charged pions (bottom panel) versus temperature at a baryon density of $10^{15}\,\mathrm{g/cm^3}$ and at an electron fraction of 0.06 for the SFHo EOS (black lines) and the modified SFHo EOSs with different pion masses, namely, vacuum mass (blue lines), 170 MeV (orange lines), and 200 MeV (green lines). The total pressure of matter for the modified EOSs with pions approaches the SFHo EOS values as the mass of the pion increases. Moreover, the net number fraction of charged pions decreases with the growing pion mass. Taken from [278].

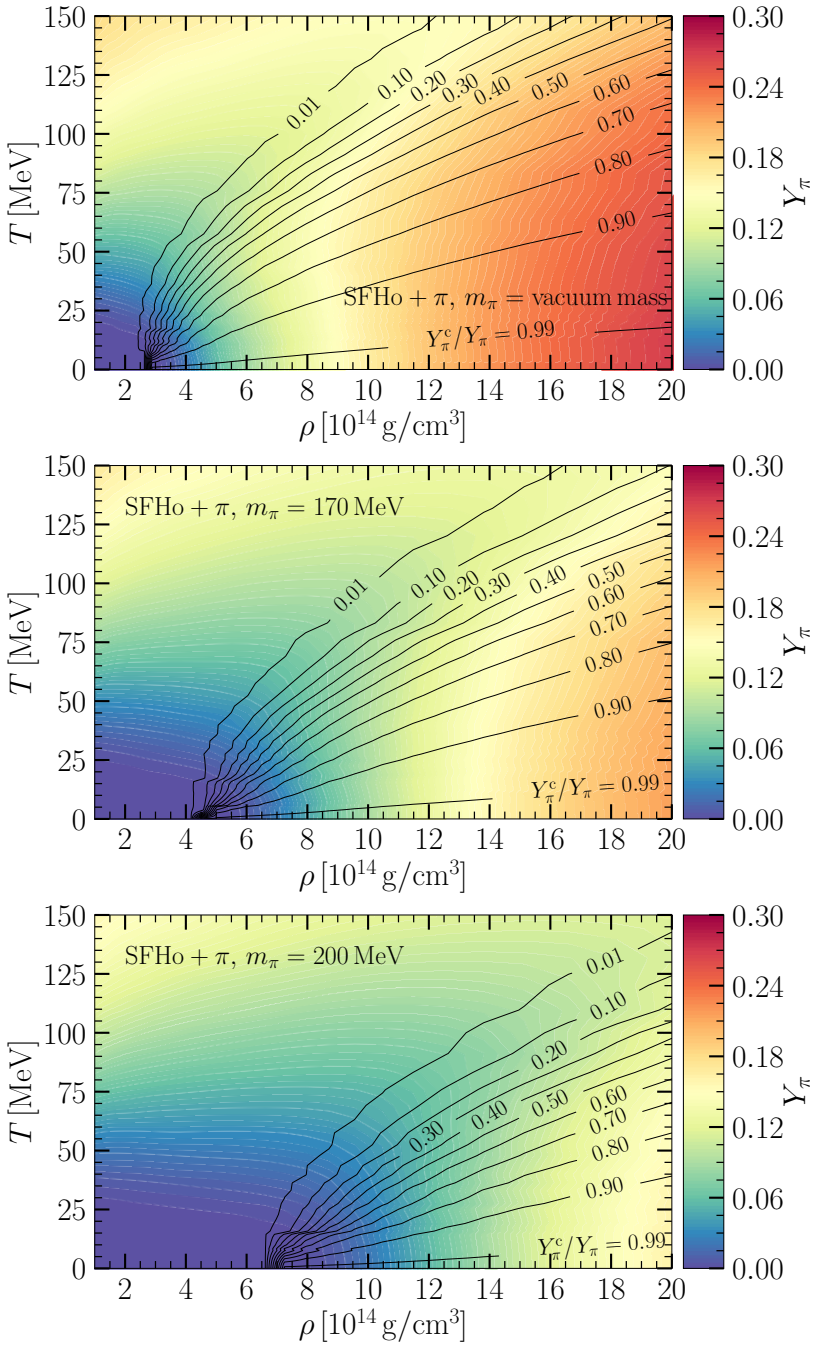

Figure 4.5: Equilibrium net number fractions of charged pions, i.e., the net number fraction of charged pions when the charged pions, nucleons, and electrons are in chemical equilibrium, are shown colour-coded on the baryon density-temperature plane (ρ-T plane) for the modified SFHo EOSs with pion masses equal to their vacuum values (top panel), 170 MeV (middle panel), and 200 MeV (bottom panel). The ratios of the equilibrium number fraction of negatively charged condensed pions and the equilibrium net number fraction of charged pions are marked by black lines. Taken from [278].

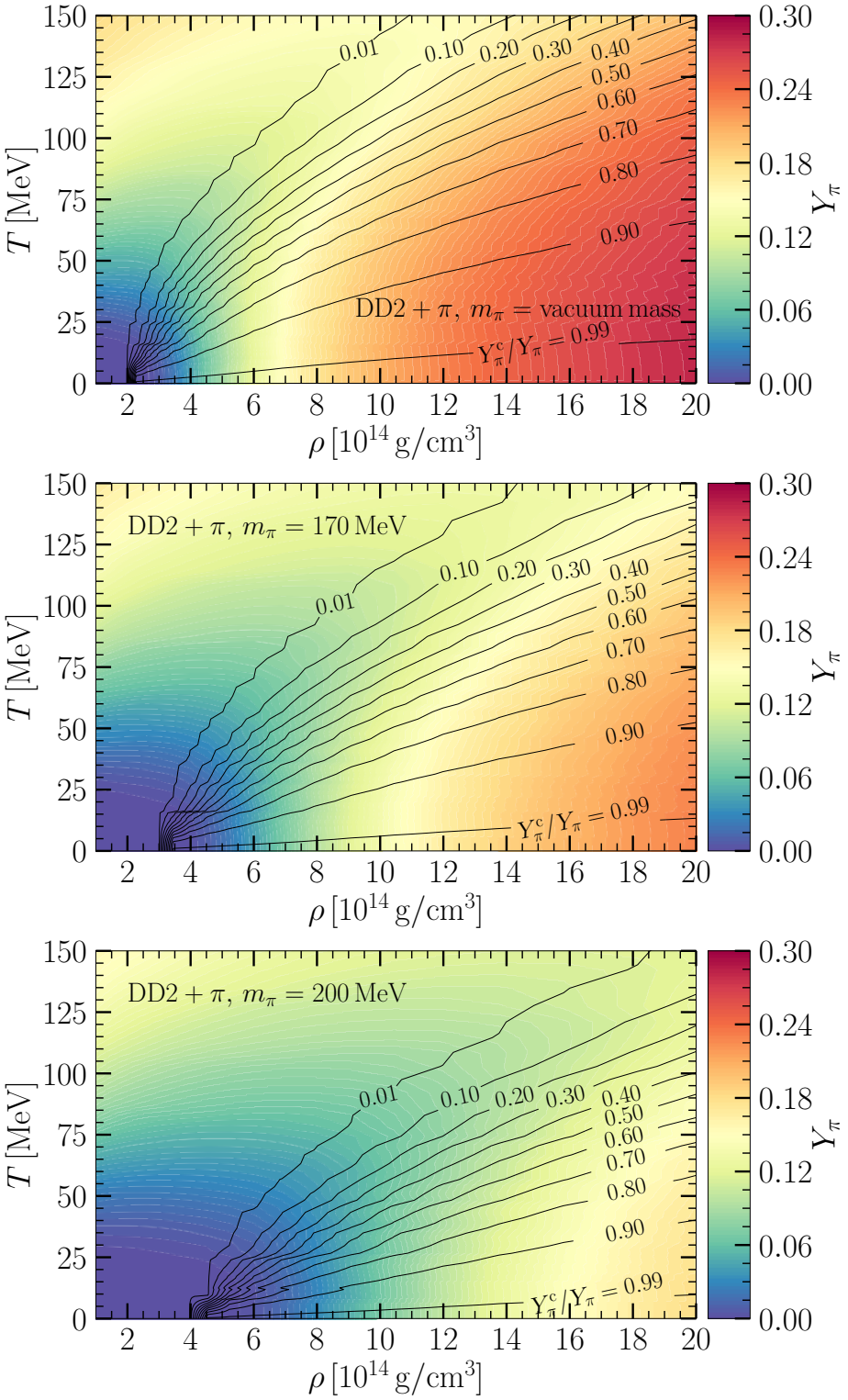

Figure 4.6: Same as Fig. 4.5 but for the EOSs based on the DD2 model. Taken from [278].

density for all modified EOSs. As the temperature decreases, a larger fraction of negatively charged pions enters the condensed state, which is also evident from Figs. 4.1 and 4.2. When comparing the panels for different modified SFHo EOSs, which correspond to different assumed pion masses, in Fig. 4.5, we see that the value of Y_π drops with increasing charged pion mass for a given baryon density and temperature. As the charged pion masses grow, it becomes necessary to reach higher densities and lower temperatures to achieve the same value of the Y_π^c/Y_π ratio because a larger value of $\hat{\mu}$ is required to form the pion condensate. Similar qualitative trends in the behaviour of Y_π and Y_π^c/Y_π with varying density, temperature, and pion masses can be observed for the modified DD2 EOSs, as shown in Fig. 4.6.

4.2. Stellar structure and merger modelling

To understand the impact of pions on BNS mergers, we first study the stellar structure of isolated NSs using EOS models that include pions. We then perform a series of simulations using the EOS models described in section 4.1 based on the SFHo and DD2 models, with effective pion masses equal to their vacuum masses, 170 MeV, and 200 MeV. As a reference, we also consider simulations without pions by utilising the base SFHo and the base DD2 EOS.

4.2.1. Stellar structure of isolated NS star

Before describing merger simulations with the new EOS models, we first explore the influence of pions on stellar structure by examining the zero-temperature neutrinoless beta-equilibrium slices of the EOS models and by solving the Tolman–Oppenheimer–Volkoff (TOV) equations [270, 198] for these barotropic relations.

The presence of pions in NS matter significantly affects the conditions for chemical equilibrium and thereby influences the equilibrium stellar structure of NSs and determines the initial conditions for binary mergers. In Fig. 4.7, we show the beta-equilibrium conditions at zero temperature. The upper panel shows the chemical potential difference between neutrons and protons as a function of density. Once $\mu_n - \mu_p$ reaches the value of the effective pion mass used in the model, the difference remains constant. Consequently, the electron chemical potential value also becomes constant, which implies that the electron fraction Y_e decreases with density because $\mu_e = \text{const.} \propto n_e^{1/3} \propto (\rho Y_e)^{1/3}$ for relativistic electrons. This can be seen in the middle panel, where the thick lines exhibit Y_e. Thus, in the regime where $\mu_n - \mu_p$ remains constant, the electron fraction value is independent of the nuclear EOS.

With larger effective pion masses, the point at which the chemical potential becomes constant sets in at a higher density. At this critical density, the presence of condensed pions leads the proton fraction to diverge from the electron fraction (as shown in the middle panel). Establishing the charge neutrality between protons, electrons and pions, we see an increase in Y_p compared to the base EOS. The proton

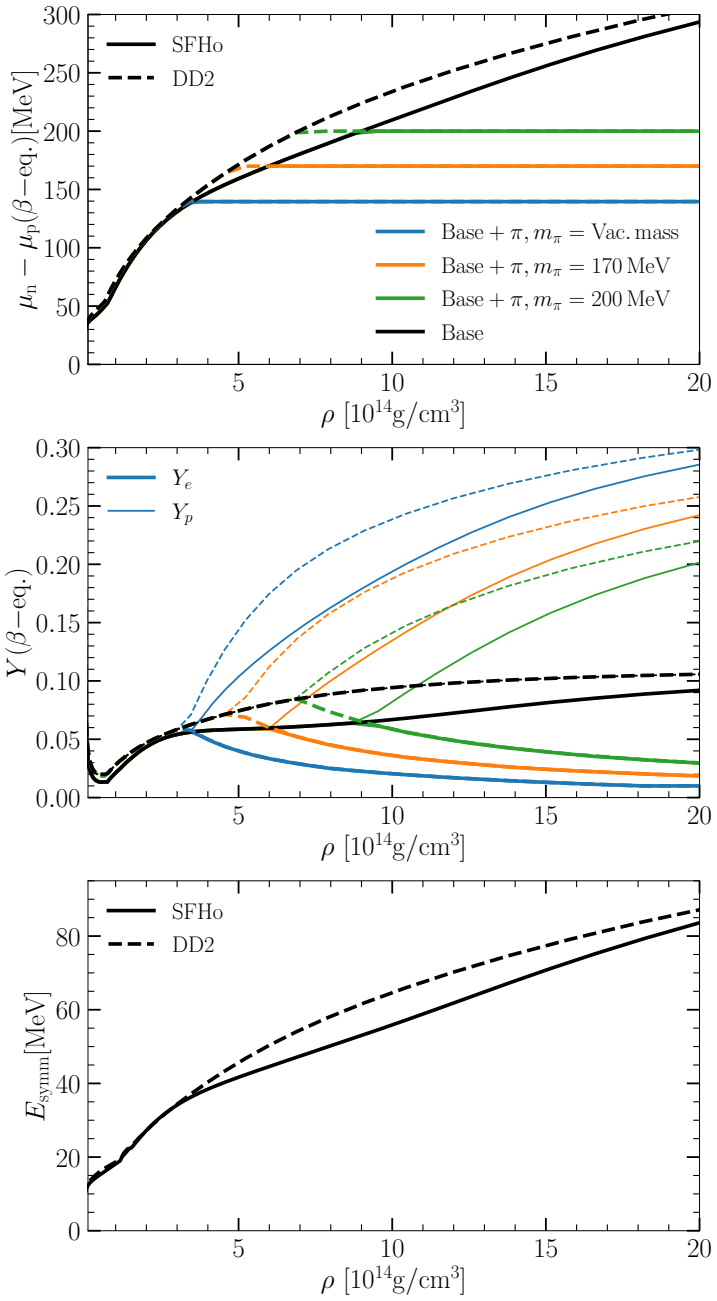

Figure 4.7: Top panel shows the difference between neutron and proton chemical potential as function of density at zero temperature for beta-equilibrium. The middle panel provides the electron fraction and proton fraction in beta-equilibrium. The bottom panel displays the symmetry energy of nuclear matter as the energy difference between neutron matter and symmetric matter. In all panels, black curves refer to the base EOS without pions. Coloured curves show the aforementioned quantities for EOSs with pions assuming different effective pion masses. Solid lines are for SFHo based models, while dashed curves visualise DD2 based models. In the middle panel thin lines display the proton fraction and thick lines indicate the electron fraction. For the base models, both coincide. Taken from [278].

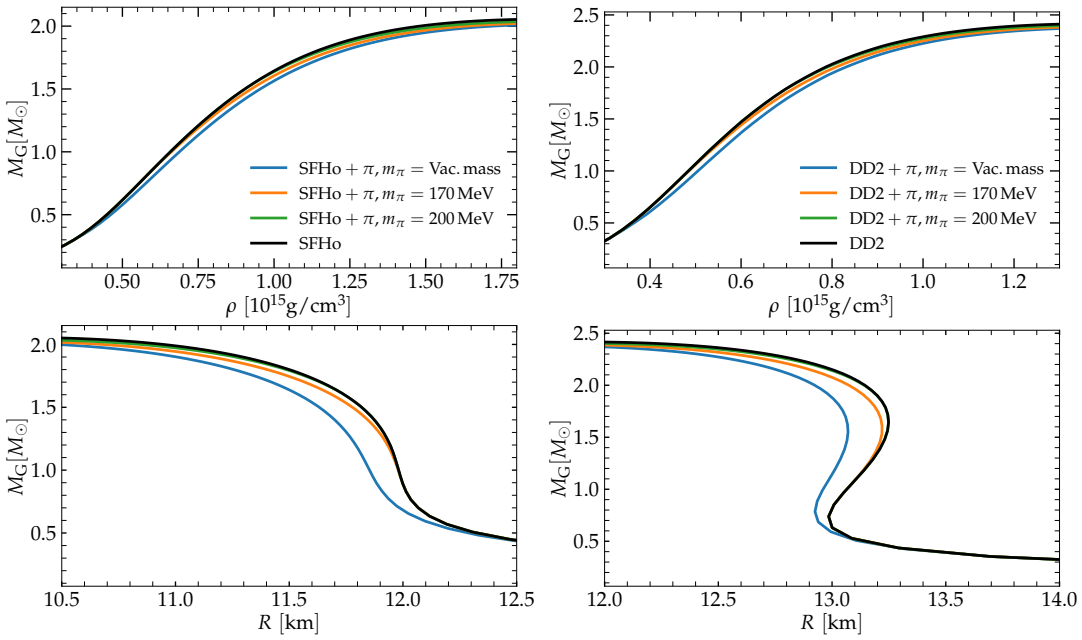

(a) SFHo (b) DD2

Figure 4.8: Left: Gravitational mass versus central baryon density (top panels) and gravitational mass versus the radius of NSs (bottom panels) for the base SFHo EOS and the ones including pions, SFHo, SFHo + π, m_π = Vac. mass, SFHo + π, $m_\pi = 170\,\mathrm{MeV}$ and SFHo + π, $m_\pi = 200\,\mathrm{MeV}$. Right: Same plots as in the left panel, but for DD2, DD2 + π,m_π = Vac. mass, DD2 + π, $m_\pi = 170\,\mathrm{MeV}$ and DD2 + π, $m_\pi = 200\,\mathrm{MeV}$. Taken from [278].

fraction exhibits a dependence on the nuclear EOS at all densities, including the regime with pion condensation. As a result, the fraction of pions also relies on the EOS to maintain charge neutrality.

One can better understand this behaviour by considering the symmetry energy of the EOS which is defined as the energy difference between neutron matter and symmetric matter. In beta-equilibrium matter composed of neutrons, protons and electrons, the symmetry energy determines the proton fraction from the difference of chemical potentials between neutrons and protons, $\hat{\mu} = \mu_{\rm n} - \mu_{\rm p}$, and $Y_{\rm p}$ (see, e.g. [101, 141]; noting that there exist slight variations in the definitions of symmetry energy used in the literature). Thus, in the regime of pion condensation where $\hat{\mu} = \text{const.}$, the proton fraction is entirely determined by the symmetry energy. This symmetry energy is illustrated in the bottom panel of Fig. 4.7. With a rise in symmetry energy for a constant $\hat{\mu}$, it is also evident from the middle panel that the proton fraction increases after a certain critical density. Specifically, as a consequence of a larger symmetry energy (bottom panel), the DD2-based models display a higher proton fraction in comparison to the SFHo-based models.

In Fig. 4.8(a), calculated at zero temperature, we present NS gravitational masses versus central densities (top panel) and NS gravitational masses versus NS radii (bottom panel) for the SFHo EOS and the modified SFHo EOSs with pions. Figure. 4.8(b) displays the same relations as in Fig. 4.8(a), but for the DD2 EOS and the modified DD2 EOSs with pions. As we can notice from the top panel of Figs. 4.8(a) and 4.8(b), the production of condensed pions in a NS lowers the pressure support against gravity and leads to a reduced mass for the same central density. Furthermore, the inclusion of pions leads to a reduction in the maximum mass for both EOS models. This effect ranges from one to two percent for models adopting the vacuum masses and diminishes for higher effective pion masses. See Tabs. 4.1 and 4.2. Similar trends are also observed for NS radii, where we see a reduction of about one percent for models adopting the vacuum masses.

In general, the inclusion of pions causes a softening effect, resulting in higher compactness. Within a specific EOS with a constant effective pion mass, the softening at higher densities is inversely proportional to the effective mass of the pion incorporated in that EOS. In cases of large effective pion masses, the stellar structure closely resembles that derived from EOSs without pions.

4.2.2. Simulation details

We conduct hydrodynamical simulations of NS mergers using our SPH code without neutrinos that employs the conformal flatness condition to solve the general relativistic Einstein field equations [110, 286, 194, 193, 28]. The initial setup of neutron stars is constructed by imposing neutrinoless β-equilibrium conditions in the respective EOSs. This ensures that neutrons, protons, electrons, and pions (if present) are in both chemical and thermal equilibrium. The stars are assumed not to have any intrinsic rotation and to be in a quasi-circular equilibrium orbit, with an orbital separation designed to facilitate a merger after a few orbital revolutions. Since we do not include any explicit interactions from neutrinos in any of our simulations with pions, we instead advect the initial electron fraction with the fluid,

Table 4.1: Properties of the simulated models with the SFHo EOS and the modified SFHo EOSs with pions. First column shows names of the simulated models. The second column shows the gravitational masses of BNSs, m_π is the effective pion mass employed in the modified EOS, $R_{\rm ns}$ and Λ are the radius and the dimensionless tidal deformability of a single NS corresponding to one of the star in the equal-mass BNS system. $M_{\rm chirp}$ represents the chirp mass of the BNS system. The column "Prompt collapse" indicates whether a BH is formed immediately after the merger or not, $f_{\rm peak}$ denotes the peak frequency of the GW spectrum. The $f_{\rm peak}$ is shown only for the models without prompt collapse. Taken from [278].

Model	BNS masses $[M_\odot]$	m_π [MeV]	$R_{\rm ns}$ [km]	Λ	$M_{\rm chirp}$ $[M_\odot]$	Prompt collapse	$f_{\rm peak}$ [kHz]
SFHo_Pions_VacMass_1.35_1.35	1.35–1.35	vacuum mass	11.727	377.902	1.175	no	3.462
SFHo_Pions_170MeV_1.35_1.35	1.35–1.35	170 MeV	11.872	413.490	1.175	no	3.351
SFHo_Pions_200MeV_1.35_1.35	1.35–1.35	200 MeV	11.896	420.776	1.175	no	3.318
SFHo_Base_1.35_1.35	1.35–1.35	no pion	11.896	420.813	1.175	no	3.310
SFHo_Pions_VacMass_1.40_1.40	1.40–1.40	vacuum mass	11.700	296.937	1.219	no	3.599
SFHo_Pions_170MeV_1.40_1.40	1.40–1.40	170 MeV	11.845	324.561	1.219	no	3.530
SFHo_Pions_200MeV_1.40_1.40	1.40–1.40	200 MeV	11.874	332.950	1.219	no	3.454
SFHo_Base_1.40_1.40	1.40–1.40	no pion	11.874	332.970	1.219	no	3.419
SFHo_Pions_VacMass_1.42_1.42	1.42–1.42	vacuum mass	11.687	270.635	1.236	yes	—
SFHo_Pions_170MeV_1.42_1.42	1.42–1.42	170 MeV	11.833	296.199	1.236	no	3.621
SFHo_Pions_200MeV_1.42_1.42	1.42–1.42	200 MeV	11.864	303.134	1.236	no	3.552
SFHo_Base_1.42_1.42	1.42–1.42	no pion	11.864	303.089	1.236	no	3.499
SFHo_Pions_VacMass_1.425_1.425	1.425–1.425	vacuum mass	11.684	264.060	1.241	yes	—
SFHo_Pions_170MeV_1.425_1.425	1.425–1.425	170 MeV	11.830	289.202	1.241	yes	—
SFHo_Pions_200MeV_1.425_1.425	1.425–1.425	200 MeV	11.862	295.680	1.241	no	3.622
SFHo_Base_1.425_1.425	1.425–1.425	no pion	11.862	295.619	1.241	no	3.573
SFHo_Pions_VacMass_1.43_1.43	1.43–1.43	vacuum mass	11.681	257.484	1.245	yes	—
SFHo_Pions_170MeV_1.43_1.43	1.43–1.43	170 MeV	11.827	282.205	1.245	yes	—
SFHo_Pions_200MeV_1.43_1.43	1.43–1.43	200 MeV	11.859	288.226	1.245	yes	—
SFHo_Base_1.43_1.43	1.43–1.43	no pion	11.859	288.156	1.245	no	3.614

i.e. $\frac{dY_e}{dt} = 0$, which represents a relatively simple treatment of weak interactions

As a first approach, we only consider equal mass BNS systems. Specifically, we select binaries with masses of 1.35-1.35$M_\odot$ and total mass close to the threshold binary mass for prompt BH formation, which we estimate for the EOSs with pions from empirical relations [33]. We provide a complete list of simulations in Tab. 4.1 for SFHo based models and table 4.2 for DD2 based models[2]. These tables provide details on the total mass of the binaries ($M_1 + M_2$) , the effective mass of pions, the radius of cold, isolated NSs with half of the total mass of the BNS, the tidal deformability of the binary system, and the chirp mass. We recall the definition of tidal deformability from Eq. 1.3. The chirp mass is given by $M_{\rm chirp} = \frac{(M_1 M_2)^{3/5}}{(M_1+M_2)^{1/5}}$, where M_1 and M_2 are the individual masses of the NSs in the binary. We also specify whether the system undergoes a prompt gravitational collapse and include the dominant GW frequency of the postmerger phase. For the models which experience prompt collapse, this dominant GW frequency is not calculated.

4.3. Simulation results

In this section, we begin with the description of the general dynamics and the evolution of the pion contributions in our binary merger simulations. Then, we address the postmerger GW signal, associated empirical relations for postmerger GW frequencies, the threshold mass for prompt BH formation, and the mass ejection to understand the extent to which these features are affected by the presence of pions.

4.3.1. Dynamics and pion production in NS mergers

All binary neutron star merger simulations proceed in a qualitatively similar manner. Apart from qualitative effects, no specific differences are observed between calculations with the base EOSs and those with the modified EOSs incorporating pions. Most of the simulated binaries result in the formation of a rotating HMNS remnant. Only a few systems with relatively large total binary masses lead to direct BH formation after merging (to be discussed below in Sec. 4.3.4).

In simulations where a NS remnant is formed, the merging stars create a rotating double-core structure. As the densities in the postmerger phase increase, the remnant undergoes vivid oscillations. These density oscillations can be seen in Fig. 4.9, which shows the evolution of the maximum baryonic rest-mass density for the 1.35-1.35 $M_\odot$ BNS models. The quantitative trends align with existing findings in the literature, where softer EOSs result in higher densities. This observation applies to both the comparison between the base EOSs, SFHo and DD2, as well as the comparison between the respective base EOS and the versions incorporating pions. Smaller effective pion masses result in softer EOSs and more

[2]In these tables we do not list all simulations performed for this study but provide only those for which we run the same total binary mass for all four versions of the EOS model. To determine the threshold binary mass for the individual EOS models we conducted additional simulations for specific total binary masses.

Table 4.2: Properties of the simulated models with the DD2 EOS and the modified DD2 EOSs with pions. Same as Tab. 4.1 but for the models based on DD2. Taken from [278].

Model	BNS masses $[M_\odot]$	m_π [MeV]	$R_{\rm ns}$ [km]	Λ	$M_{\rm chirp}$ $[M_\odot]$	Prompt collapse	$f_{\rm peak}$ [kHz]
DD2_Pions_VacMass_1.35_1.35	1.35–1.35	vacuum mass	13.048	796.159	1.175	no	2.681
DD2_Pions_170MeV_1.35_1.35	1.35–1.35	170 MeV	13.189	854.982	1.175	no	2.642
DD2_Pions_200MeV_1.35_1.35	1.35–1.35	200 MeV	13.199	871.076	1.175	no	2.597
DD2_Base_1.35_1.35	1.35–1.35	no pion	13.199	871.135	1.175	no	2.608
DD2_Pions_VacMass_1.62_1.62	1.62–1.62	vacuum mass	13.068	262.744	1.410	no	3.099
DD2_Pions_170MeV_1.62_1.62	1.62–1.62	170 MeV	13.219	287.197	1.410	no	3.030
DD2_Pions_200MeV_1.62_1.62	1.62–1.62	200 MeV	13.247	294.408	1.410	no	3.008
DD2_Base_1.62_1.62	1.62–1.62	no pion	13.247	294.465	1.410	no	2.997
DD2_Pions_VacMass_1.64_1.64	1.64–1.64	vacuum mass	13.066	243.524	1.428	yes	—
DD2_Pions_170MeV_1.64_1.64	1.64–1.64	170 MeV	13.217	266.835	1.428	no	3.137
DD2_Pions_200MeV_1.64_1.64	1.64–1.64	200 MeV	13.248	270.335	1.428	no	3.024
DD2_Base_1.64_1.64	1.64–1.64	no pion	13.248	270.407	1.428	no	3.036
DD2_Pions_VacMass_1.65_1.65	1.65–1.65	vacuum mass	13.065	234.778	1.436	yes	—
DD2_Pions_170MeV_1.65_1.65	1.65–1.65	170 MeV	13.216	256.653	1.436	yes	—
DD2_Pions_200MeV_1.65_1.65	1.65–1.65	200 MeV	13.248	260.521	1.436	no	3.127
DD2_Base_1.65_1.65	1.65–1.65	no pion	13.248	260.531	1.436	no	3.047
DD2_Pions_VacMass_1.66_1.66	1.66–1.66	vacuum mass	13.064	226.031	1.445	yes	—
DD2_Pions_170MeV_1.66_1.66	1.66–1.66	170 MeV	13.216	246.472	1.445	yes	—
DD2_Pions_200MeV_1.66_1.66	1.66–1.66	200 MeV	13.248	251.637	1.445	yes	—
DD2_Base_1.66_1.66	1.66–1.66	no pion	13.248	251.658	1.445	no	3.139

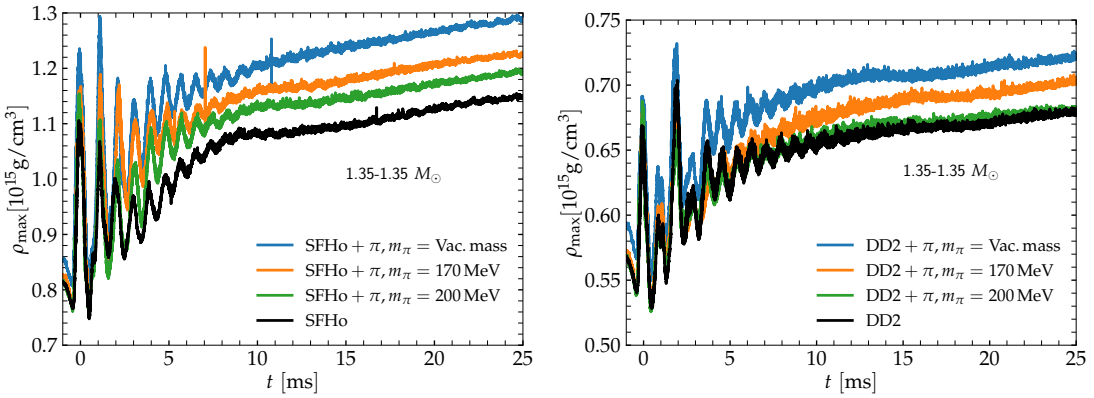

(a) SFHo (b) DD2

Figure 4.9: Time evolution of the maximum baryonic rest-mass density for 1.35-1.35$M_\odot$ BNS systems using SFHo EOS (left panel) and DD2 EOS (right panel). The time zero corresponds to the instant of the maximum compression during the first bounce after merging (minimum in the lapse function). We evaluate the maximum baryonic rest-mass density at the SPH particle level, which is why some noise is visible. Taken from [278].

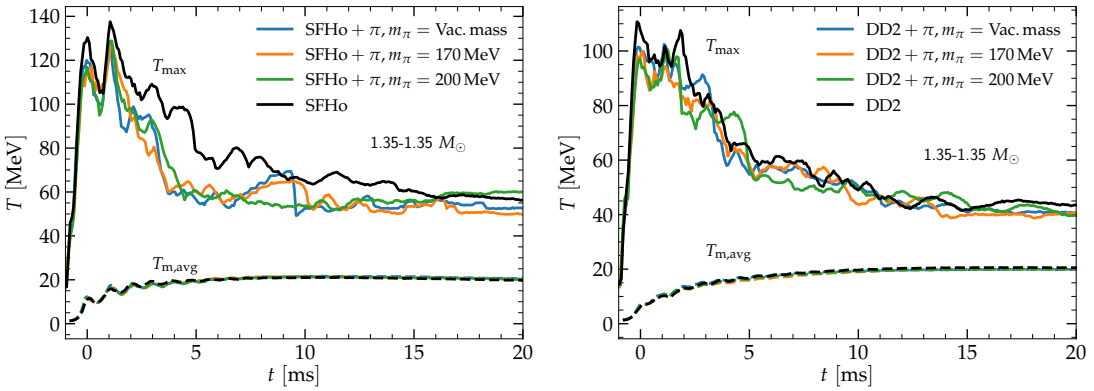

(a) SFHo (b) DD2

Figure 4.10: Time evolution of the maximum and mass-averaged temperature for 1.35-1.35$M_\odot$ BNS systems using SFHo EOS (left panel) and DD2 EOS (right panel). The time zero corresponds to the instant of the maximum compression during the first bounce after merging (minimum in the lapse function). Taken from [278].

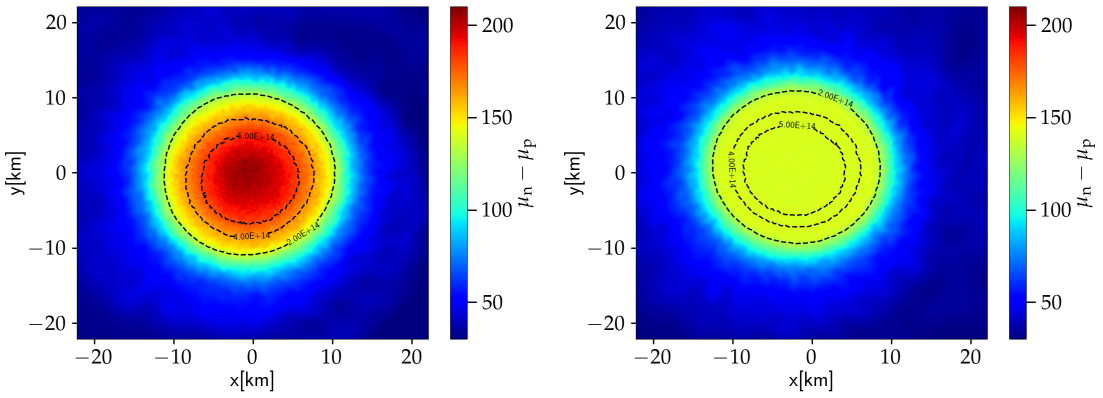

(a) Base DD2

(b) DD2 + π, m_π = Vac. mass

Figure 4.11: The panels (a) and (b) show snapshots of neutron and proton chemical potential difference $\mu_n - \mu_p$ in the equatorial plane for a 1.35-1.35$M_\odot$ BNS model after the merger, using the base DD2 EOS without pions and the modified DD2 EOS that includes pions with an effective pion masses equal to their vacuum masses, DD2 + π, m_π = Vac. mass. The density regions of 2×10^{14}g/cm^3, 4×10^{14}g/cm^3 and 5×10^{14}g/cm^3 are shown by dashed contour lines. Taken from [278].

compact stellar configurations, leading to higher $\rho_{\max}$ values in the merger remnant. Quantitatively, these maximum densities in the merger remnant are consistent with empirical relations for $\rho_{\max}$ derived from a large sample of candidate EOSs without pions (see discussion below in Sec. 4.3.3).

As discussed in Sec. 4.1, depending on the density and temperature, the production of pions depends on the chemical potential difference between neutrons and protons. At typical densities in the context of NSs and NS merger remnants, the contributions from thermal pions become significant only when the temperature exceeds a certain threshold value of several tens of MeV (see Fig. 4.2 and discussion in Sec. 4.1). To assess the temperatures produced in merger remnants, we show the evolution of the maximum temperature and the mass-averaged temperature in Fig. 4.10 for 1.35-1.35 $M_\odot$ BNS simulations.

The highest temperatures are observed at the collisional interface between the merging NSs, with this contact layer typically having a thickness ranging from some hundreds of meters to kilometers. It is important to note that the exact values of $T_{\max}$ are influenced by numerical resolution, with the general trend indicating an increase in the maximum temperature by a few tens of percent, shown in Fig. 4.15. We have investigated this resolution dependence by running additional simulations with about 600,000, 1,200,000 and 2,400,000 SPH particles compared to our default resolution of about 300,000 SPH particles. The maximum temperatures show a slight increase with higher resolution by at most a few 10 MeV, which is roughly comparable to the differences between models with and without pions. However, we observe that relative changes in $T_{\max}$ over time are independent of the resolution. While the maximum temperatures can reach around 100 MeV, such extreme conditions are confined to a small volume within the remnant and do not

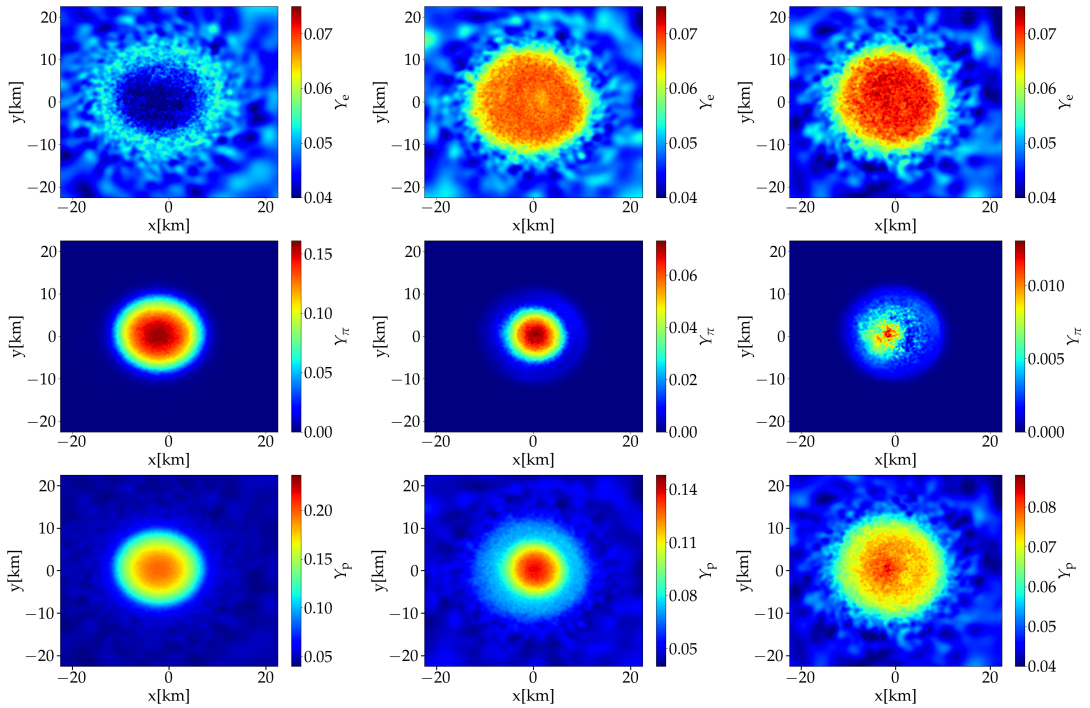

(a) DD2 + π, m_π = Vac. mass (b) DD2 + $\pi, m_\pi = 170$ MeV (c) DD2 + $\pi, m_\pi = 200$ MeV

Figure 4.12: Y_e distribution (top row panels), Y_π distribution (middle row panels) and Y_p distribution (bottom row panels) in the equatorial plane for 1.35-1.35$M_\odot$ BNS systems using DD2+π, m_π = Vac. mass (left column panels), DD2+π, m_π = 170 MeV (middle column panels) and DD2 + π, m_π = 200 MeV (right column panels). Taken from [278].

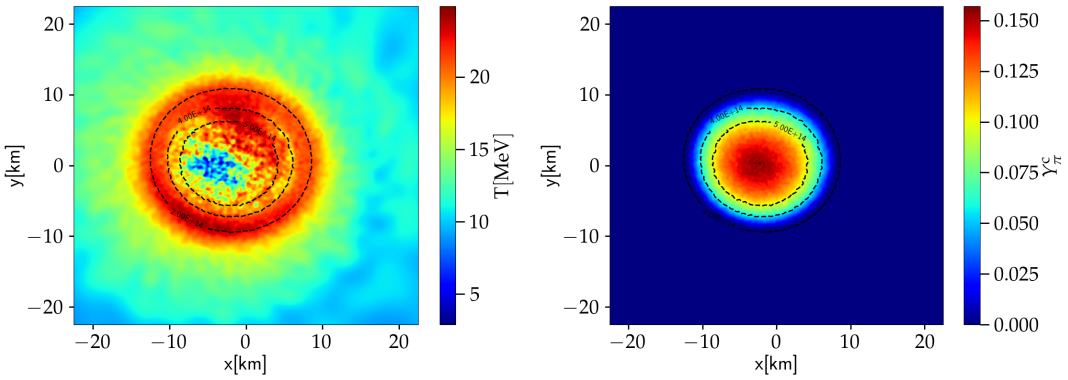

(a) T [MeV] (b) Y_π^c

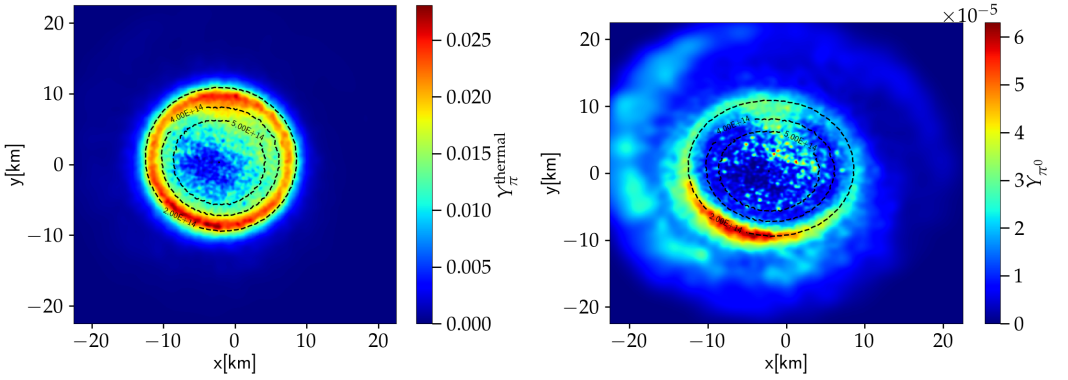

(c) Y_π^{thermal} (d) Y_{π^0}

Figure 4.13: Temperature, Y_π^c, Y_π^{thermal} and Y_{π^0} distribution in the equatorial plane for a 1.35-1.35$M_\odot$ BNS system using the DD2 + π, m_π = Vac. mass model. The densities of 2×10^{14}g/cm^3, 4×10^{14}g/cm^3 and 5×10^{14}g/cm^3 are shown by dashed contour lines. Taken from [278].

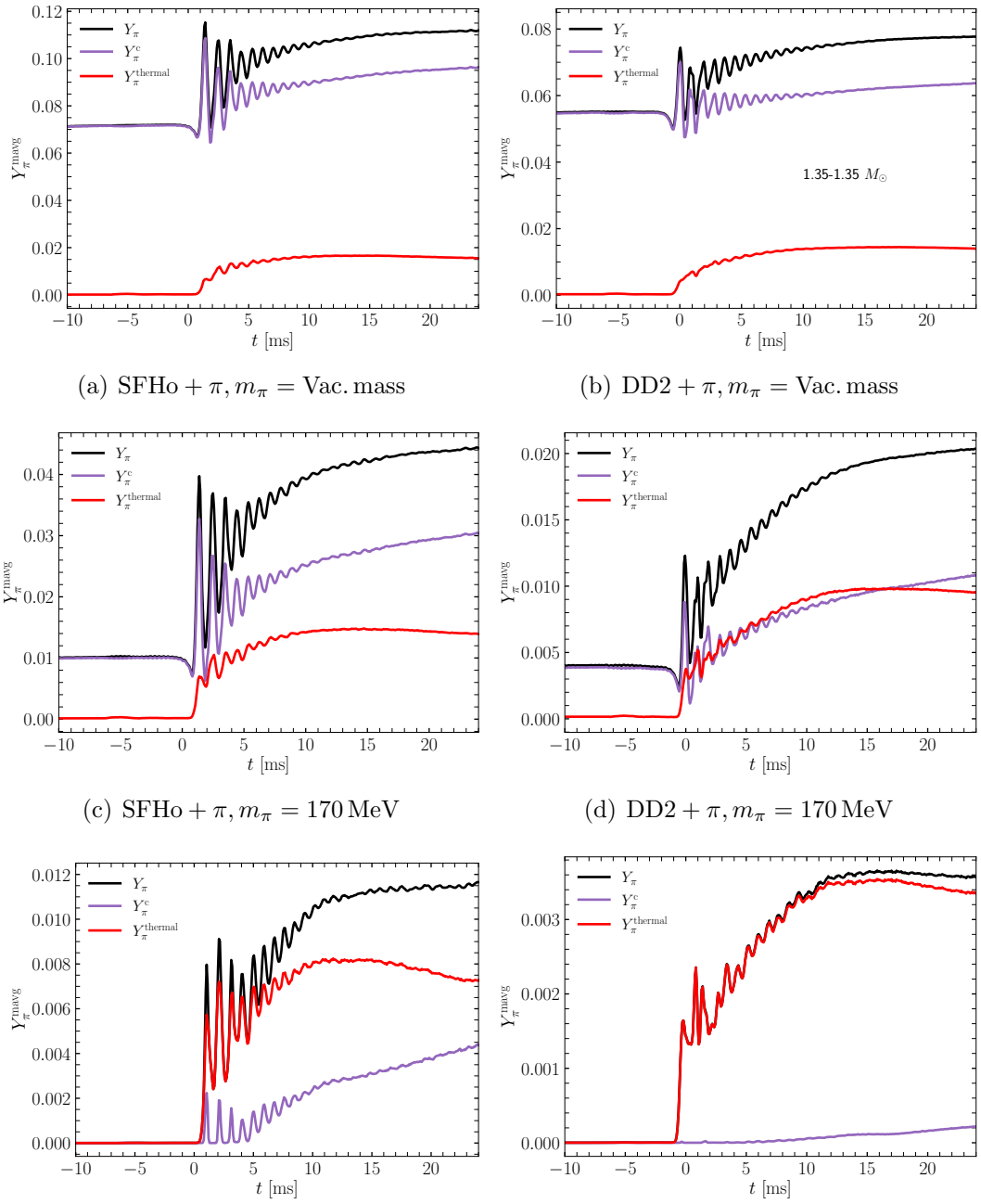

(a) SFHo $+\,\pi, m_\pi =$ Vac. mass

(b) DD2 $+\,\pi, m_\pi =$ Vac. mass

(c) SFHo $+\,\pi, m_\pi = 170\,$MeV

(d) DD2 $+\,\pi, m_\pi = 170\,$MeV

(e) SFHo $+\,\pi, m_\pi = 200\,$MeV

(f) DD2 $+\,\pi, m_\pi = 200\,$MeV

Figure 4.14: Time evolution of the mass-averaged pion fraction $Y_\pi^{\rm mavg}$ of total pion fraction Y_π, condensed pion fraction $Y_\pi^{\rm c}$ and thermal pion fraction $Y_\pi^{\rm thermal}$ for 1.35-1.35$M_\odot$ BNS systems. The time zero corresponds to the instant of the maximum compression during the first bounce after merging (minimum in the lapse function). Taken from [278].

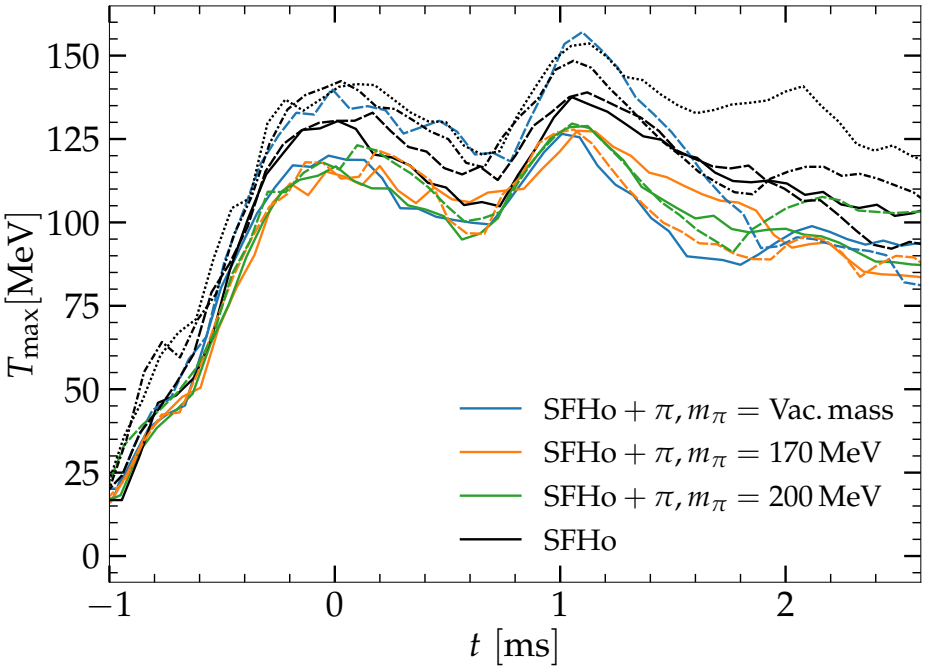

Figure 4.15: Time evolution of the maximum temperature for 1.35-1.35$M_\odot$ BNS systems using SFHo EOS. The solid lines indicate simulations with 300K SPH particles and the dashed lines indicate simulations with 600K SPH particles. In addition, we also show the results from the simulation with 1.2 million and 2.4 million SPH particles using dashed-dotted and dotted lines. Due to high computation cost, these runs were ran only until the first one or few milliseconds after the merger. The time zero corresponds to the instant of the maximum compression during the first bounce after merging (minimum in the lapse function).

necessarily correspond to the highest densities. Average temperatures within the merger remnant are significantly lower and of the order of about 20 MeV. This suggests that the contribution from thermal pions likely play only a sub-dominant role in the merger remnant of the systems considered here and the inclusion of pions in BNS merger simulations overall has a softening effect.

In Fig. 4.10(a), we notice that the models with the softer SFHo EOS exhibit slightly higher maximum temperatures compared to the models with DD2 EOS. This can be attributed to the more violent collisions of stars described by the former EOS, which leads to stronger compression of the remnant. Additionally, there is the tendency for models incorporating pions to yield slightly lower maximum temperatures. We also note from Fig. 4.4 that at these high temperatures, the inclusion of pions can result in a stiffening of the EOSs, a trend which appears to be relatively independent of the effective pion mass. Since the evaluation of the temperature is based on individual SPH particles, we caution that they are susceptible to noise and one should not overinterpret the differences in the maximum temperature between EOSs. Note that in Fig. 4.15, we also run simulations with about 600,000 SPH particles for all SFHo models with and without pions. The evolution of $T_{\max}$ in the first few milliseconds after merging follows approximately

the one in the simulations with our default resolution. Only for the model with m_π equal to the vacuum mass, we find that $T_{\max}$ is higher (by about 20 MeV) compared to the run with 300,000 particles. Comparing runs with 600,000 particles, the model with pion mass equal to the vacuum mass actually features the highest temperatures in the first milliseconds after merging somewhat in contrast to the finding for the default-resolution simulations, where the base models yields the highest $T_{\max}$.

Upon directly evaluating the ratio between the number of thermal pions and pions in the condensate, we indeed find that thermal pions are subdominant in the hot merger remnant and the primary effects of pions appear to originate from the condensate (Figs. 4.13 and 4.14 except for the case with $m_\pi = 200$ MeV). In this regard, it is instructive to directly compare the chemical potential difference $\hat{\mu}$ between neutrons and protons for the base model and the calculation that incorporates pions. In Fig. 4.11, we show the distribution of $\hat{\mu}$ in the equatorial plane of the merger remnant for the base DD2 model and the model with pions which adopts the vacuum pion mass. In the latter case due to condensation, $\hat{\mu}$ is restricted to the mass of the pion (~ 139.6 MeV for this case), which otherwise can exceed more than 200 MeV in the central remnant if pions are not included. For models with pions where the effective mass is equal to their vacuum mass, a pion condensate is found to be present throughout the whole high-density region of the remnant. From the range of $\hat{\mu}$ in the left panel of Fig. 4.11, it is evident that the condensation of pions in the remnant depends on the chosen effective pion mass. For instance, $\hat{\mu}$ increases towards the centre and reaches 200 MeV only in the innermost region of the base model. As a consequence, for $m_\pi = 200$ MeV, pion condensation occurs solely in the centre of the remnant at the highest densities. This clearly illustrates the significant impact of the effective pion mass on the production of pions in BNS mergers.

In Fig. 4.12, we display the snapshots of the electron fraction (top panel), the pion fraction (middle panel) and the proton fraction (bottom panel) for a 1.35-1.35$M_\odot$ BNS merger remnant in the equatorial plane at approximately 18.95 milliseconds after merging. These simulations utilise the pionic DD2 EOSs, where the columns represent different m_π increasing from left to right. From the presence of pions, it is obvious that the electron fraction in the remnant which is determined by $\hat{\mu}$ is affected by both their effective mass and their properties in the progenitor (see Fig. 4.7).

With the produced number of pions, the proton fraction in the remnant increases while the electron fraction in the remnant remains rather small (Fig. 4.12(a)). For example, the highest Y_e and the lowest Y_p is found for the case when $m_\pi = 200\,\mathrm{MeV}$ (Fig. 4.12(c)) where less number of pions are produced. Recalling the simplistic treatment of weak interactions employed in these simulations where neutrinos are ignored and electron fraction is advected, both the behaviour of the pion fraction and the proton fraction are consequences of the advected electron fraction. They follow similar trends as for equilibrium NSs, i.e. Y_e is strongly suppressed for smaller effective mass with a larger pion fraction and larger proton fraction (see Fig. 4.7). Despite these simple approximations involved in the treatment of weak interactions, Fig. 4.12 indicates a potentially significant impact by pions on

the conditions for the chemical potentials in the remnant and consequently on the microphysics of weak interactions.

The dependence of the pion content in the remnant on the effective pion mass is depicted in the middle row panels of Fig. 4.12. As anticipated, the amount of pion content in the HMNS shrinks in size as the effective mass of the pion increases. For $m_\pi = 200\,\mathrm{MeV}$, the presence of pions is so significantly suppressed that it occurs only in the centre where $\hat{\mu}$ reaches more than or equal to 200MeV, i.e. the effective mass of the pion. As a result, we understand from this panel that the model with DD2$+\pi, m_\pi = 200\,\mathrm{MeV}$ should behave very similar to the models adopting the base EOS.

To examine the distribution of thermal and condensed pions in various regions of the merger remnant, we present the distribution of Y_π^{c} and Y_π^{thermal} in Fig. 4.13 for the DD2 $+ \pi, m_\pi =$ Vac. mass model along with the corresponding temperature distribution. The correlation between thermal pions and local temperature is evident from the hot ring-like structure in the merger remnant shown in Figs. 4.13(a) and 4.13(c). At relatively lower temperatures, the distribution of condensed pion fraction, i.e. Y_π^{c}, roughly follows the density distribution in Fig. 4.13(b). Regarding neutral pions, it is important to note that while the number of neutral pions increases with temperature, their relative magnitude remains very low (Fig. 4.13(d)). From Figs. 4.1 and 4.3, we anticipate that the contribution of neutral pions will only become noticeable at high temperatures, around $\sim$ 100 MeV, corresponding to SPH particles with maximum temperature.

As temperatures and densities rise during the dynamical evolution, more pions are generated compared to the pion content of the initial stars. This pion production is quantified in Fig. 4.14, which presents the mass-averaged fraction of the total number of pions, condensed pions, and thermal pions as a function of time for both SFHo and DD2 EOSs.

The production of pions is notably sensitive to the effective pion mass. When the pion mass equals the vacuum mass, a substantial number of pions is already present in the initial stars in condensate form, and the additional increase in the pion fraction during merging is moderate. In models with $m_\pi = 170\,\mathrm{MeV}$, in addition to the condensate pions during the inspiral, a substantial increase in Y_π is also observed by about a factor of four during the merger. If the effective pion mass is as high as 200 MeV, no pions are present during the inspiral. Only subsequent increase in density and temperature after merging leads to the production of pions, which are predominantly thermal in nature.

In addition to the pionic contributions, SFHo EOS being inherently softer than DD2 leads to higher densities in the inspiralling stars and higher temperatures in the postmerger remnant. For this reason, the production of pions and the softening effect is more pronounced for models based on SFHo compared to the models utilising DD2 EOS.

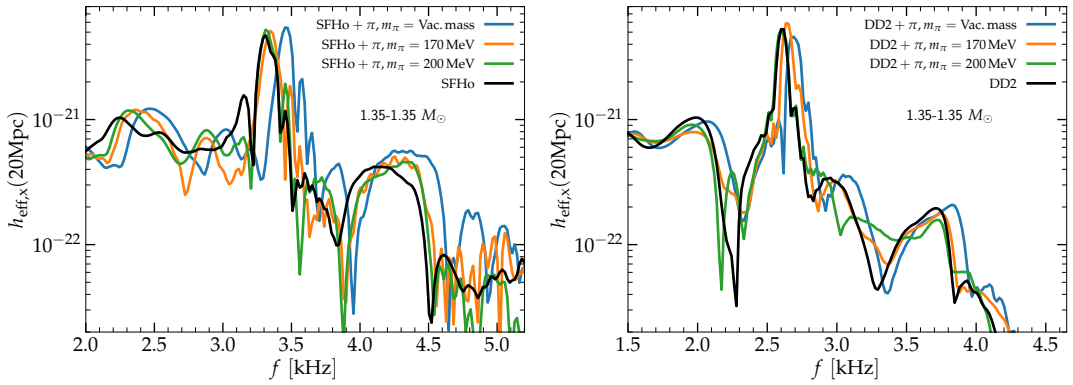

(a) SFHo (b) DD2

Figure 4.16: Comparison of the the cross-polarisation amplitude of the GW spectra for an observer at 20 Mpc along the polar axis with the SFHo and DD2 EOSs for 1.35-1.35$M_\odot$ binaries. The colour scheme is the same as in Figs. 4.9 and 4.10. Taken from [278].

4.3.2. Gravitational wave signal

Inspiral

The GW signal in BNS mergers contains information on both the dynamical evolution of BNS mergers and the properties of the EOS. During the inspiral, the GW signal is primarily related to the tidal deformability Λ of the system. When comparing the models with the base EOS without pions and the models with modified EOSs adopting the vacuum mass for the effective pion mass, we observe a reduction of Λ of up to about 10 per cent by the inclusion of pions. From the mass-radius relations in Fig. 4.8, one can infer the dependence of the tidal deformability on the chosen effective pion mass values, and that larger effective pion masses exhibit a smaller or even negligible impact on the tidal deformability.

These findings, although seem straightforward, serve as a caution that neglecting pions in EOS calculations could introduce a systematic bias, especially if the effective pion mass in the medium closely approximates its vacuum mass. This situation is particularly relevant in cases where microphysical parameters of the EOS, such as the slope of the symmetry energy, are determined from GW inspiral signal using EOS models that exclusively consider baryonic and leptonic contributions, thereby omitting the effects of pions. Disregarding pions and consequently overlooking an additional unaccounted softening in the EOS models could thus introduce a systematic bias in these parameters. However, it is evident that the severity of these issues cannot be fully assessed in our current exploratory study, given the relatively basic inclusion of pions and the arbitrary selection of effective pion masses. It is conceivable that the influence of pions might become more pronounced in the case of NSs and BNS systems with higher masses.

Postmerger

The GW signal may encompass a high-frequency component arising from the postmerger phase, specifically the dynamic evolution of the NS remnant. In contrast, the high-frequency emission from a BH forming directly in a prompt gravitational collapse is weak. If a rotating NS merger remnant is formed, the influence of pions might be significant due to finite temperatures and higher densities in the postmerger remnant compared to the inspiralling NSs. The GW emission from a BNS merger postmerger remnant is primarily characterised by a single, approximately constant frequency denoted as f_{peak}. This frequency represents the primary oscillation mode of the central object and manifests as a prominent peak in the GW spectrum.

In Fig. 4.16, the cross-polarisation amplitude of the GW spectra are depicted for an observer located at 20 Mpc along the polar axis and BNS systems with masses of 1.35-1.35$M_{\odot}$, where the left panel corresponds to models employing the SFHo EOS and the right panel represents BNS systems with the DD2 EOS. The primary frequency f_{peak} is established to closely correlate with the NS radii, serving as an indicator of the softness of the EOS [27]. The DD2 models exhibit oscillations at notably lower frequencies, approximately around 2.6 kHz, in contrast to the SFHo-based EOSs which oscillate at frequencies exceeding 3 kHz.

When considering the influence of pions, we observe that the inclusion of pions shifts the dominant peak of the GW spectrum to higher frequencies. This effect is more prominent for smaller effective pion masses, a result that aligns with the mass-radius relations of these EOSs. In particular, the shift is observed to be slightly more pronounced for the SFHo-based models, with a modification of approximately 200 Hz. For an effective pion mass, $m_{\pi} = 200\,\mathrm{MeV}$, this dominant peak remains largely unaffected by the inclusion of pions, consistent with the findings in Sect. 4.3.1, indicating a minimal contribution from pions in this particular model.

Additionally, we observe an impact on the secondary features of the GW spectrum, such as subdominant frequency peaks. These secondary features have been associated, for example, with the formation of massive tidal bulges on the surface of the remnant or the non-linear coupling of the dominant mode with the quasi-radial oscillation of the central object (as discussed in detail in [29]). Interestingly, for models based on SFHo EOS, it seems to be appear that the influence of pions on these secondary features is more substantial.

We present the frequency shift of the dominant peak and the quantitative impact of the selected effective pion mass in Fig. 4.17, revealing a clear dependence on m_{π}. Based on the observed shifts in SFHo based models compared to DD2 based models, this shift suggests a potentially stronger impact of pions in softer EOSs. Considering that softer models can attain higher densities and temperatures, and thereby a more pronounced influence from pions, this observation is not unexpected and similar trends in the frequency shift are noted for other binary masses as well (see Tabs. 4.1 and 4.2).

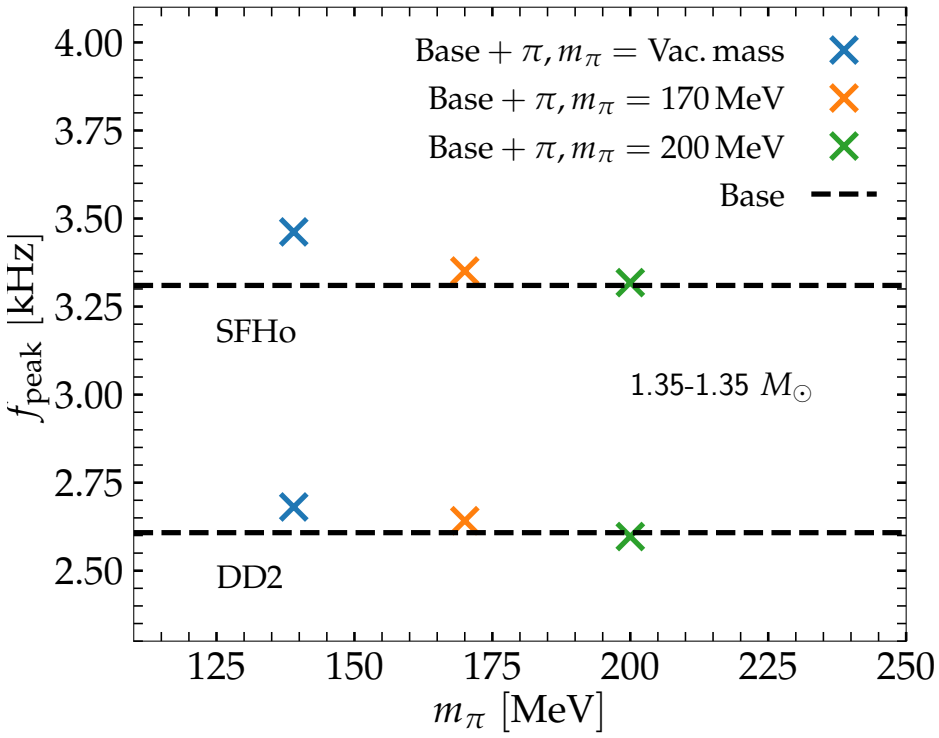

Figure 4.17: The dominant postmerger GW oscillation frequency with respect to the pion mass employed in the modified EOSs for 1.35-1.35$M_\odot$ simulations. $f_{\rm peak}$ for the respective base EOS is indicated by the black dashed line. Taken from [278].

4.3.3. Empirical relations for postmerger GW frequencies

By examining an extensive set of EOS models without pions, several empirical relationships have been widely established in the literature. These relations connect the dominant postmerger frequency to the intrinsic properties of isolated, cold, non-rotating NSs, such as their radii or tidal deformability, e.g. [26, 27, 108, 41, 264, 223, 143, 46, 274, 43, 280]. These relationships are significant as they form the basis for inferring stellar parameters, such as radii and tidal deformability, from measurements of $f_{\rm peak}$, e.g. [53].

Our findings thus far have revealed that the inclusion of pions has an impact on both the properties of isolated NSs and the characteristics of postmerger GW emission. Since the empirical relations are derived from models that do not account for pions, it becomes crucial to examine whether models incorporating pions comply with these empirical relationships or if there are any deviations. This investigation is significant because using existing relations for EOS constraints could introduce a bias if the influence of pions is not properly accounted for.

We also recall that the influence of pions might vary across different regimes. It is not straightforward to estimate, how the inclusion of pions can affect the different EOSs at different conditions. As demonstrated in Sect. 4.1, the incorporation of pions can result in either a softening or a stiffening of the EOS when compared to a base model without pions, depending on the temperature. To

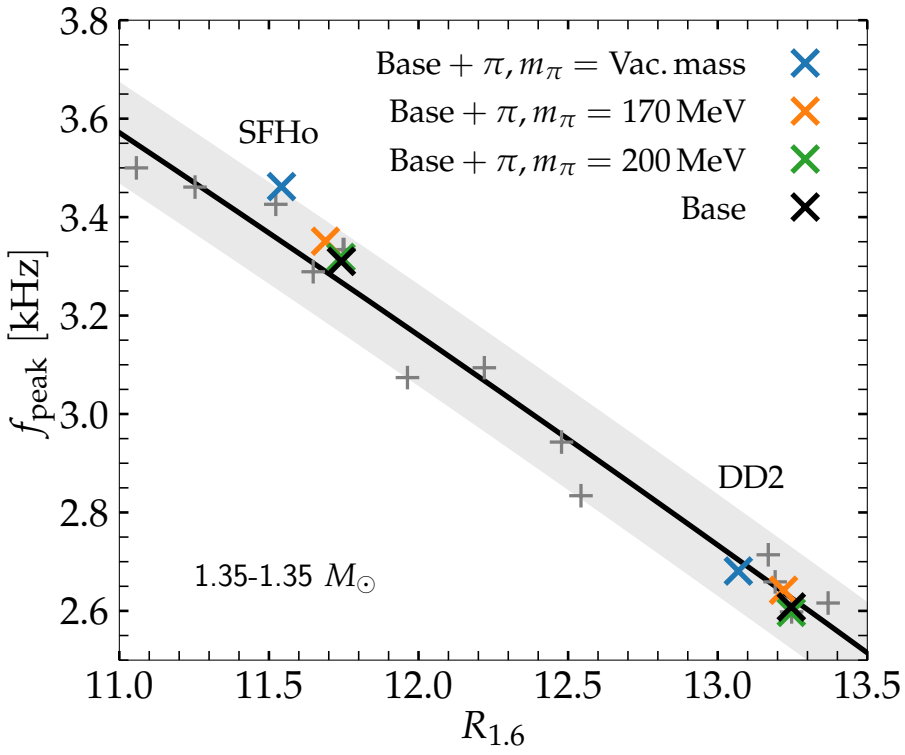

Figure 4.18: Dominant postmerger GW frequency, $f_{\rm peak}$ versus the radius of nonrotating $1.6M_\odot$ NS for 1.35-1.35$M_\odot$ BNS models using the modified SFHo and DD2 EOSs (crosses) compared to models using different microphysical EOSs which do not include pions (plus signs). The solid curve is a least squares fit to the data points of EOSs without pions, with the grey shaded area visualising the largest deviation of the data from the least squares fit. Taken from [278].

address this aspect, we approach the issue by examining mass-dependent empirical relations [43], specifically focussing on relations for a fixed total binary mass. These relations offer the most stringent correlations, making it easier to pinpoint potential deviations. In our analysis, we concentrate on binaries with a total mass of 1.35-1.35 $M_\odot$.

Figure 4.18 illustrates the relationship between $f_{\rm peak}$ and the radius $R_{1.6}$ of nonrotating NSs with a mass of 1.6 $M_\odot$ [27]. The plot incorporates results from our recent calculations and previous data from [43] for a broader range of EOSs, which do not account for pions. The solid black line represents a least squares polynomial fit to the data from [43], describing the behaviour of EOS models without pions. The shaded band illustrates the maximum scatter in this relation and its width is set to match the maximum residual between the fit and the data.

The figure demonstrates that the incorporation of pions does not result in significant deviations from the empirical $f_{\rm peak}$-$R_{1.6}$ relation. The presence of pions alters both the postmerger GW emission and the properties of nonrotating NSs. Thus, the modifications by pions to a large extent cancel each other. Only for the SFHo model with m_π equal to the vacuum mass of pions, $f_{\rm peak}$ shifts to higher frequencies, making it marginally compatible with the inherent scatter of this rela-

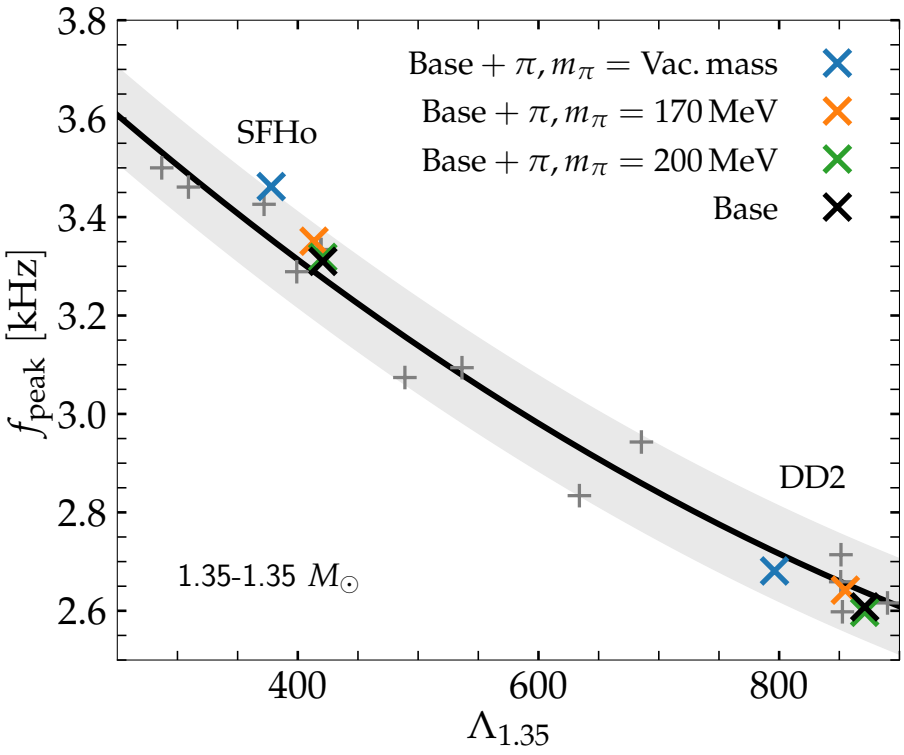

Figure 4.19: Dominant postmerger GW frequency, $f_{\rm peak}$, versus the tidal deformability Λ of 1.35-1.35$M_\odot$ BNSs using modified SFHo and DD2 EOSs (crosses) compared to models using different microphysical EOSs which do not include pions (plus signs). The solid curve is a least squares fit to the data points of EOSs without pions, with the grey shaded area visualising the largest deviation of the data from the least squares fit. Taken from [278].

tion defined by the shaded band (as discussed in detail in [149] regarding frequency deviations in empirical relations for the postmerger GW signal). These findings suggest that, at most, there might be a slight bias for soft EOSs, implying that the actual relation could slightly shift towards higher frequencies if the effective pion mass is close to its vacuum value.

A comparable scenario emerges for the relationships that connect the dominant postmerger frequency and the tidal deformability, which is described in works such as [264, 41, 43] and demonstrated in Fig. 4.19. Once again, models that incorporate pions align with the relationships established from models without pions. The SFHo + π, m_π = Vac. mass model results in a slightly more noticeable frequency shift, and in this case, it is only marginally compatible with the relation.

Furthermore, we explore a relationship that links the dominant postmerger frequency and the maximum rest-mass density, $\rho_{\rm max}^{\rm max}$, which occurs during the initial stages of the evolution of the postmerger remnant. Specifically, this refers to the highest maximum rest-mass density observed within the first five milliseconds after merging [31, 43]. This correlation proves valuable, as it allows for an estimation of the density regime of the central object. Figure 4.20 shows that models incorporating pions also comply with this relation with high accuracy, and no sig-

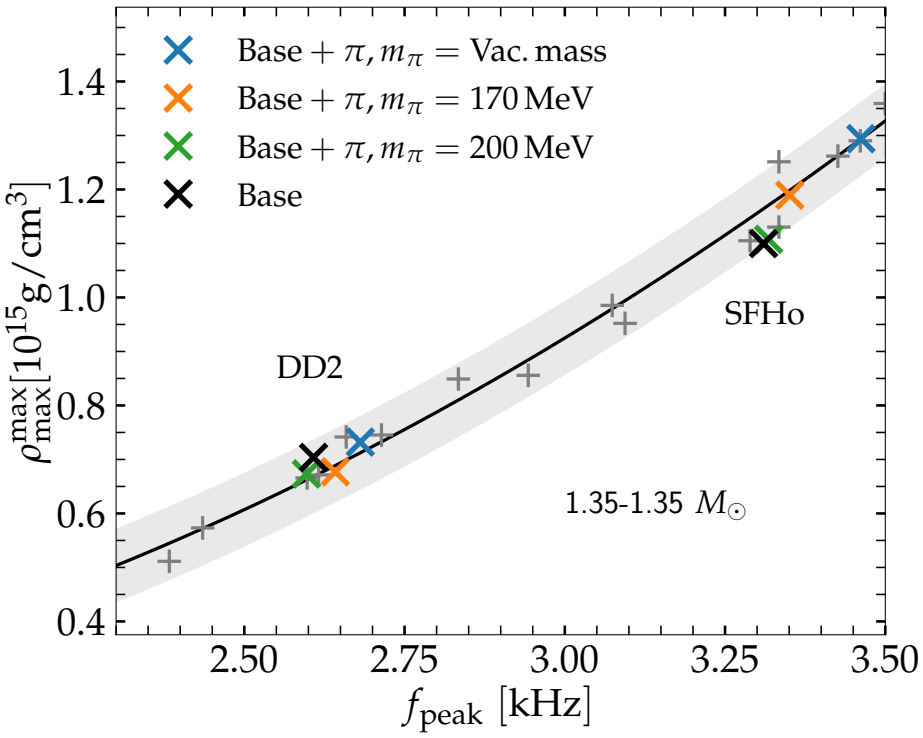

Figure 4.20: Maximum rest-mass density $\rho^{\max}_{\max}$ of the early postmerger evolution as a function of the dominant postmerger GW frequency, f_{peak}, for a 1.35-1.35$M_\odot$ BNSs using modified SFHo and DD2 EOSs (crosses) compared to models using different microphysical EOSs which do not include pions (plus signs). The solid curve is a least squares fit to the data points of EOSs without pions, with the grey shaded area visualising the largest deviation of the data from the least squares fit. Taken from [278].

nificant deviations are observed. In comparison to the base model, the calculation that incorporates an effective pion mass equal to the vacuum mass shows a slight increase in $\rho^{\max}_{\max}$. This observation aligns with the trends depicted in Figs. 4.9(a) and 4.9(b), both of which illustrate an enhanced softening of the EOS due to the inclusion of pions with this specific effective mass. This particular model exhibits the highest pion content, primarily in condensate form, as illustrated in Fig. 4.14. Consequently, it results in the most substantial shifts observed in Fig. 4.18, 4.19 and 4.20, with shifts not only parallel to the black solid lines, but also perpendicular to them. Therefore, it is not entirely implausible that more extreme models with even higher pion content could potentially result in slightly stronger deviations from the various empirical relations. However, considering that our models already encompass a comprehensive coverage of the allowed parameter space, more significant deviations appear improbable.

4.3.4. Threshold mass

The high-density EOS plays a crucial role in shaping the outcomes of BNS mergers. It governs the nature, evolution, and stability of the merger remnants, which can either lead to the formation of a BH for high total binary masses or result in the creation of a massive, rotating neutron star if the total mass of the system does not surpass the threshold mass for a prompt gravitational collapse. Therefore, it is necessary to explore whether pions have an effect in this context as well.

We focus our attention on the threshold binary mass $M_{\rm thres}$ for prompt BH formation. This measure serves as a general indicator of the stability of the remnant formed during a BNS merger. Similar to previous studies [24, 34, 33], we calculate $M_{\rm thres}$ by conducting simulations with varying total binary masses $M_{\rm tot}$ for a specific EOS model. From this series of calculations, we determine the model with the highest $M_{\rm tot} = M_{\rm stab}$ that does not experience a direct collapse to a BH. Simultaneously, we identify the lightest system with $M_{\rm tot} = M_{\rm unstab}$ that promptly forms a BH. The threshold mass $M_{\rm thres}$ is then defined as,

$$M_{\rm thres} = 0.5(M_{\rm stab} + M_{\rm unstab}). \tag{4.1}$$

To differentiate between prompt BH formation and a delayed gravitational collapse, we analyse the evolution of the minimum lapse function $\alpha_{\rm min}$. If $\alpha_{\rm min}$ consistently decreases after initial contact, it indicates a prompt collapse. On the other hand, if $\alpha_{\rm min}$ stabilises and starts to increase, indicating a bounce in the merger remnant, we classify this behaviour as a delayed collapse. In addition to other possible numerical errors in the simulations, the method and definition of $M_{\rm thres}$ used in this study indicate that $M_{\rm thres}$ can only be determined with a finite level of accuracy. For each EOS model, we calculate the threshold mass to be at least within a range of $\pm 0.02\ M_\odot$, i.e. $M_{\rm unstab} - M_{\rm stab} = 0.04\ M_\odot$.

Table 4.3 provides a comprehensive list of threshold masses for all the EOS models analysed in this study. Please note that the values for $M_{\rm thres}$ for our base models may slightly differ from those presented in [33] for the same EOS. This discrepancy arises because $M_{\rm thres}$ is determined using the above mentioned bracketing method based on the results of binary simulations with other total masses. In this study, we achieve a higher accuracy in determining $M_{\rm thres}$ within $\pm 0.02\ M_\odot$ compared to [33]. It is essential to highlight that despite the slight differences in the threshold masses, the outcomes of the respective simulation data are entirely consistent with each other.

In both base EOS models, the systematic inclusion of pions leads to a consistent reduction in $M_{\rm thres}$. Within a given base model, this decrease is more pronounced for smaller m_π and can be as substantial as $0.08\ M_\odot$ (approximately two percent of $M_{\rm thres}$). This aligns with the observed behaviour in the analysis of the GW emission, where smaller effective pion masses result in a more significant overall softening of the EOS. Interestingly, this behaviour might not be immediately intuitive since the inclusion of pions, independent of the effective mass values, actually leads to a stiffening of the EOS in the regime of very high temperatures. However, it appears that the overall softening has a more substantial impact on the stability. This phenomenon could be explained by the fact that only a tiny volume of the

Table 4.3: Determination of threshold mass. The first column gives the different EOSs models used in this chapter. $M_{\rm thres}$ is the threshold binary mass for prompt collapse. $M_{\rm max}$ is the maximum mass of the non-rotating NS, $R_{1.6}$ is the radius of a 1.6 $M_\odot$ nonrotating NS, $R_{\rm max}$ is the radius of the nonrotating maximum mass NS. $\Lambda_{1.4}$ and $\tilde{\Lambda}_{\rm thres}$ are the tidal deformability of a $1.4M_\odot$ NS and the tidal deformability of a binary system with a total mass equal to $M_{\rm thres}$. The last four columns provide an estimated $M^{\rm fit}_{\rm thres}$ using available fit formulae [33] of the form $M^{\rm fit}_{\rm thres} = M^{\rm fit}_{\rm thres}(M_{\rm max}, Y)$ with Y being either $R_{1.6}$, $R_{\rm max}$, $\Lambda_{1.4}$ or $\Lambda_{\rm thres}/2$. For the estimate we employ the respective values of $M_{\rm max}$ and Y for the EOS model of the given row. The fit formulae are obtained from models without pions and thus the estimates allow to assess the performance of these relations for models including pions. The difference, $M_{\rm thres}$ - $M^{\rm fit}_{\rm thres}(M_{\rm max}, Y)$, between the actual threshold mass (second column) and the estimate by the respective fit formula is given in parentheses. We quote the maximum residuals of the respective fits in parentheses in the third line (see [33]). Taken from [278].

Model	$M_{\rm thres}$	$M_{\rm max}$	$R_{1.6}$	$R_{\rm max}$	$\Lambda_{1.4}$	$\tilde{\Lambda}_{\rm thres}$	$M^{\rm fit}_{\rm thres}$ ($Y = R_{1.6}$)	$M^{\rm fit}_{\rm thres}$ ($Y = R_{\rm max}$)	$M^{\rm fit}_{\rm thres}$ ($Y = \Lambda_{1.4}$)	$M^{\rm fit}_{\rm thres}$ ($Y = \tilde{\Lambda}_{\rm thres}$)
(Max. dev./$M_\odot$)							(0.042)	(0.059)	(0.056)	(0.085)
	[$M_\odot$]	[$M_\odot$]	[km]	[km]			[$M_\odot$]	[$M_\odot$]	[$M_\odot$]	[$M_\odot$]
SFHo + π, Vac. mass	2.810	2.017	11.542	10.085	296.937	290.362	2.806(0.004)	2.804(0.006)	2.784(0.026)	2.796(0.014)
SFHo + π, 170 MeV	2.845	2.026	11.688	10.212	324.561	292.701	2.835(0.010)	2.832(0.013)	2.811(0.034)	2.816(0.029)
SFHo + π, 200 MeV	2.855	2.038	11.741	10.277	332.950	291.953	2.851(0.004)	2.850(0.005)	2.825(0.030)	2.832(0.023)
SFHo Base	2.870	2.056	11.743	10.285	332.970	282.036	2.861(0.009)	2.859(0.011)	2.835(0.035)	2.830(0.040)
DD2 + π, Vac. mass	3.250	2.381	13.069	11.692	639.278	256.841	3.257(-0.007)	3.271(-0.021)	3.271(-0.021)	3.228(0.022)
DD2 + π, 170 MeV	3.290	2.390	13.220	11.791	699.649	261.744	3.287(0.003)	3.294(-0.004)	3.325(-0.035)	3.256(0.034)
DD2 + π, 200 MeV	3.310	2.403	13.246	11.865	700.166	256.079	3.298(0.012)	3.314(-0.004)	3.333(-0.023)	3.259(0.051)
DD2 Base	3.322	2.417	13.246	11.899	700.146	250.548	3.306(0.016)	3.327(-0.005)	3.341(-0.019)	3.263(0.059)

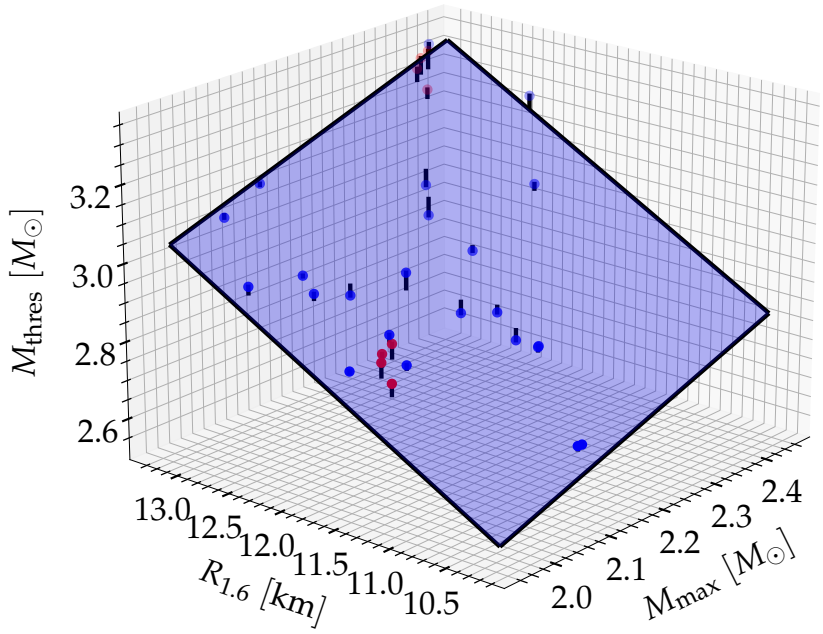

Figure 4.21: Threshold binary mass for prompt collapse as a function of the radius $R_{1.6}$ of a 1.6 $M_\odot$ NS and the maximum mass $M_{\rm max}$ of nonrotating NSs. The blue dots display the results for EOS models without pions, and the blue plane shows a least squares fit to these data (set "b" from [33]). Vertical lines visualise the deviation between the respective data point and the fit (plane). The red dots show the data for the simulations with the EOSs employed in this study including pions. Taken from [278].

remnant features conditions where stiffening by pions could occur, while the rest of the remnant experiences a considerable softening effect.

Similar to the features of the GW signal, the threshold mass for prompt BH formation also follows several empirical relations. These relations describe $M_{\rm thres}$ as a function of stellar parameters of cold, nonrotating neutron stars (NSs). Several such relations have been proposed, derived from the analysis of a large and diverse set of EOS models without pions [24, 30, 133, 34, 9, 33, 271, 125, 132]. These empirical relations usually rely on two key stellar parameters, with one of them being the maximum mass $M_{\rm max}$ of nonrotating NSs. Here we test an approach that involves a bi-linear ansatz,

$$M^{\rm fit}_{\rm thres}(M_{\rm max}, Y) = aM_{\rm max} + bY + c, \tag{4.2}$$

with fitting parameters a, b and c, while Y being either the radius $R_{1.6}$ of a $1.6M_\odot$ NS or radius $R_{\rm max}$ of a non-rotating neutron star at its maximum mass or tidal deformability $\Lambda_{1.4}$ of a $1.4M_\odot$ NS or tidal deformability $\tilde{\Lambda}_{\rm thres}$ measure at the half of the threshold mass [34, 33]. All these stellar parameters are detailed in Tab. 4.3.

The inclusion of pions in an EOS model leads to simultaneous changes in the stellar parameters of cold, nonrotating neutron stars and the threshold mass for BH formation. Therefore, it is crucial to verify whether models incorporating pions comply with the empirical relations derived from fits to EOS models without pions. These relations are used to establish constraints on neutron star properties and interpret BNS merger observations [34, 33]. In Table 4.3, we provide the estimated threshold mass for all models in this study using empirical relations constructed based on EOSs without pions [33]. We insert the stellar parameters from both our modified EOS tables and the original EOS tables. Specifically, we list estimates based on the fits numbered 1, 15, 29 and 43 in [33], which utilise the EOS set labelled "b" containing viable EOS models without phase transition to deconfined quark matter.

Models with pions closely follow these relations with exceptional accuracy, and no significant deviations were found. The differences between the fits and the actual threshold mass are provided in Tab. 4.3. These deviations are generally small, especially when compared to the maximum residuals of the fits given in Tab. 4.3. The accuracy of the fits is further demonstrated in Fig. 4.21, which illustrates $M_{\rm thres}^{\rm fit}(M_{\rm max}, R_{1.6})$. The models incorporating pions (red data points) do not exhibit significant deviations. A similar behaviour is also observed for other empirical relations, as detailed in [33].

Thus, in general, this comparison shows that the empirical relations for $M_{\rm thres}^{\rm fit}$ are accurate and can be effectively employed, even though they do not account for the presence of pions. This is primarily due to the fact that pions influence both the threshold mass and the stellar parameters of neutron stars in such a manner that the resulting effects nearly cancel each other out. As a result, EOS constraints based on relations for the threshold mass, such as those presented in [35, 32, 33], remain unaffected by the exclusion of pions.

4.3.5. Mass ejection

Finally, we focus on the mass ejection in BNS mergers, a crucial aspect necessary for the nucleosynthesis of heavy elements via the rapid neutron-capture process and for the generation of electromagnetic counterparts, kilonovae, e.g. [78, 21, 252, 160, 29, 214, 177, 60, 234, 116]. Certainly, a crucial parameter of interest is the ejecta mass $M_{\rm ej}$, as it significantly influences the production of heavy elements and the characteristics of the resulting electromagnetic transient. Mass ejection in BNS mergers comprises various phases. The simulations discussed here specifically assess the dynamical ejecta, referring to the material that becomes gravitationally unbound during the first few 10 milliseconds following the merger.

Figure 4.22 displays the amount of unbound material as a function of time for the EOS models derived from SFHo (left panel) and DD2 (right panel) for 1.35-1.35 $M_\odot$ binaries. It is evident that the dynamical mass ejection is increased in models incorporating pions, and smaller effective pion masses tend to produce larger amounts of unbound matter. This behaviour is in line with the expectation that softer equations of state leading to smaller neutron star radii result in larger ejecta masses, a phenomenon observed in studies that ignore the effects of

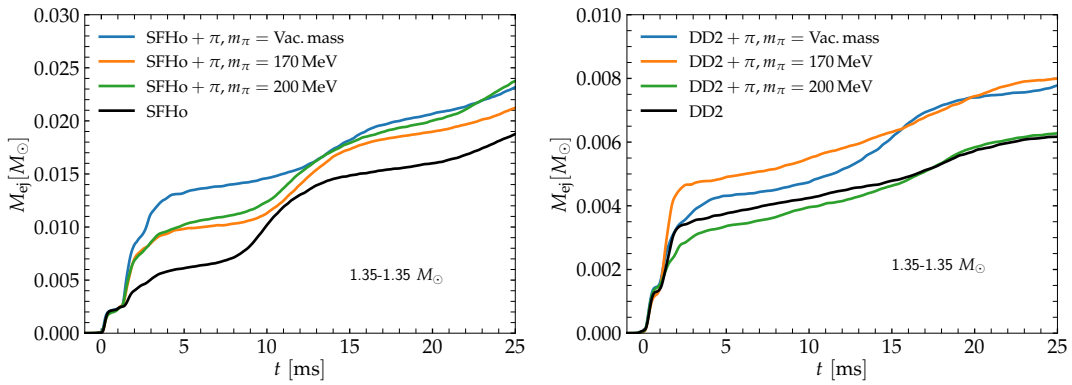

(a) SFHo (b) DD2

Figure 4.22: Time evolution of the ejecta mass for 1.35-1.35$M_\odot$ BNS mergers using modified SFHo EOSs and DD2 EOSs along with their base EOSs. The time zero corresponds to the instant of the maximum compression during the first bounce after merging (minimum in the lapse function). Taken from [278].

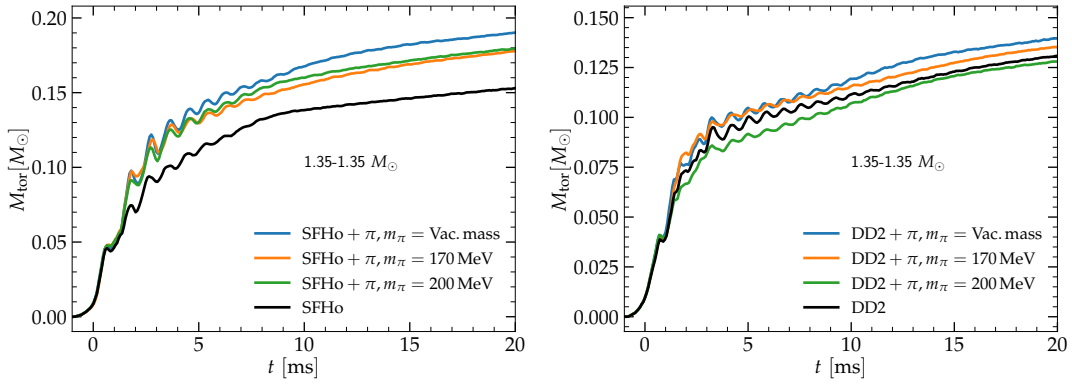

(a) SFHo (b) DD2

Figure 4.23: Time evolution of the torus mass for 1.35-1.35$M_\odot$ BNS mergers using modified SFHo EOSs and DD2 EOSs along with their base EOSs. The time zero corresponds to the instant of the maximum compression during the first bounce after merging (minimum in the lapse function). Taken from [278].

pions [25, 109]. Nevertheless, the softening effect due to the inclusion of pions is relatively subtle, and neutron star radii do not exhibit significant changes, especially for larger effective pion masses. Given this, the observed impact of pions, as depicted in Fig. 4.22 appears to be stronger than anticipated.

Considering previous research works, one would anticipate $M_{\rm ej}$ to increase by only a few percent if neutron star radii decrease by one or two percent. This expectation is based on fit formulas linking the ejecta mass and neutron star radii, as illustrated, for instance, in Fig. 22 of [116], which relies on fits from [70, 57, 135, 183]. However, in Fig. 4.22, it is observed that there is an increase of more than 20% in the dynamical ejecta mass for models employing effective pion masses equal to their vacuum values. Specifically, for models employing effective pion mass values of 170 MeV and 200 MeV, the change in the NS radius is subdominant whereas we see a considerable increase in the ejecta mass values. The absolute values of the dynamical ejecta mass $M_{\rm ej}$ for the base models in Fig. 4.22, approximately 10 milliseconds after merging, align with the results presented in [25], where $M_{\rm ej}$ is determined at the same time. Moreover, typical estimates from existing fit formulas are roughly consistent with the observed $M_{\rm ej}$ values around 10 milliseconds after the collision. It is important to note that the relationships between $M_{\rm ej}$ and neutron star parameters typically exhibit large uncertainties. The ejecta mass is a highly sensitive quantity to numerical methods, and simulations may not be fully converged due to numerical limitations, in addition to the potentially missing physics in the calculations (as discussed in [116]). This sensitivity to various factors might explain the absence of a precise hierarchy concerning m_π.

SPH simulations conducted with different numbers of particles (without neutrinos) as demonstrated in [25] reveal that the ejecta mass can vary by several tens of percent. In these cases, $M_{\rm ej}$ does not exhibit a clear trend with particle number, but rather appears to fluctuate statistically. Therefore, the differences observed in Fig. 4.22 are only tentative, but caution that ignoring the effects of pions might have a more significant impact on mass ejection than implied by the changes in the properties of cold, nonrotating NSs. These findings could significantly impact attempts to deduce EOS constraints from observed kilonovae events, as highlighted in studies such as [57]. It is crucial to recognise that the inclusion of pions affects the EOS in a complex, non-continuous manner across different regimes, involving both softening and stiffening with respect to a base model. This intricate interplay might also contribute to the observed behaviour illustrated in Fig. 4.22.

We note that only an exceedingly small fraction of the ejecta ($< 1\%$ for SFHo, 0% for DD2) is produced from densities beyond the threshold density where the pion condensation sets in at about 3×10^{14} g/cm^3 in beta-equilibrium (as shown in Fig. 4.7). Hence, in merger models with pions, the initial proton fraction of the ejecta remains basically unaffected compared to the base model. This observation suggests that the influence of pions on the composition of the ejecta might be a secondary effect, even when weak interactions are considered in the simulations.

Figure 4.23 illustrates the evolution of the torus mass as a function of time. As a coarse estimate, the torus is defined as the material with density below 10^{13}g/cm^3 and provides a rough estimate of the amount of secular ejecta, which constitutes a fraction of a few tens of percent of the torus material (see, e.g., [119] for a detailed

analysis of torus ejecta). Similar to the dynamical ejecta, we aim to investigate whether the inclusion of pions has an impact on the torus mass since the same few tens of percent of torus mass can become unbound, influence the r-process, and the resulting kilonova. Similar to ejecta mass, in Fig. 4.23, we observe an increase in the torus mass for models that incorporate pions, indicating an increasing trend toward softer equations of state (with the exception of the DD2-based EOS with $m_\pi = 200$ MeV).

We also consider fitting formulas that establish relationships between the torus mass and the TOV properties. These formulas are derived from simulation results and are compiled in Fig. 23 of [116], which includes formulas from [68, 135, 183]. It is important to recognise that these relations are approximate, and that different fitting formulas exhibit significant variations. However, they generally suggest that softer equations of state lead to smaller torus masses. Therefore, these fit formulas predict that changes in TOV properties induced by the inclusion of pions would result in a decrease in the torus mass, contrary to our observed findings. This demonstrates the complexity of the impact of pions on the torus mass and highlights the need for further detailed investigations in this regard.

5. Conclusions

5.1. Systematic study of BNS mergers with neutrinos

In the first part of the thesis, we successfully ran a comprehensive set of BNS merger simulations that include neutrinos with an advanced state of the art leakage-equilibration-absorption scheme [16]. We investigate in detail the dynamical mass ejection, the properties of the ejecta, and the associated nucleosynthesis yields produced from mergers.

We first investigate exemplarily a 1.35-1.35$M_\odot$ BNS merger using the SFHo EOS [105, 104, 262] and focus on the influence of neutrinos and mass ejection. For comparison, we also simulate a BNS merger with the same initial setup and by turning off the neutrinos at the merger when the minimum of the lapse function occurs [136]. For the run with neutrinos, we observe a decrease in the mass of the ejecta and in the temperatures of the ejected material, due to considerable cooling resulting from the emission of neutrinos. We also find a significant increase in the Y_e values of the ejected material compared to simulations without neutrinos, since the source term of neutrinos (Eq. 2.18) is the one that drives the overall Y_e distribution from the initial cold β-equilibrium values (see Fig. 4.7) to higher values, through weak interactions.

The distribution of Y_e and the characteristics of most ejecta agree with existing simulations [248, 217, 136, 96, 92, 182, 40, 207, 42, 63], where higher Y_e values are found along the polar axis and lower values are found near the equatorial direction. In contrast to numerous simulations in the literature, our calculation does not collapse into a BH at the end of our simulation. We observe higher temperatures in the composition of the ejecta and a wider range of Y_e values.

We perform full nucleosynthesis network calculations based on the trajectories extracted from this simulation with neutrinos. Along the polar direction, the ejecta which are observed to exhibit higher values of Y_e result in a notable reduction in the abundance of heavy elements. Consequently, the production of lanthanides along the polar direction decreases as we move closer to the polar z-axis. Despite the reduction in the amount of lanthanides, the nucleosynthesis yields from the dynamical ejecta are observed to produce a wide range of r-process heavy elements and exhibit a more robust second and third r-process peaks within the isotopic abundances that closely resemble the solar abundance [99]. Therefore, we observe a distinct correlation between the initial Y_e composition of the

ejecta at the beginning of the nuclear network calculations and the resulting heavy elements.

We then conduct a systematic study of BNS merger simulations with neutrinos using the SFHo and DD2 EOS. This study encompasses varying total masses and mass ratios while focussing on the dynamics and evaluating the correlation between the mass of dynamically ejected material and its characteristics with respect to variations in the binary parameters and the NS EOS.

Comparing the dynamics of postmerger evolution between the symmetric binaries and the corresponding asymmetric binaries with the same total mass, we observe a systematic decrease in the dominant postmerger oscillation frequencies $f_{\rm peak}$ to lower values and find a relatively quick approximate plateau of maximum densities within the remnants of asymmetric mergers. In addition, we also observe higher temperatures, higher average electron fractions, and a resulting higher neutrino luminosities in the merger remnants of asymmetric mergers. When comparing the neutrino luminosities of different neutrino species, a hierarchy is observed between the luminosities of electron antineutrinos, heavy lepton neutrinos and electron neutrinos, i.e. $L_{\bar{\nu}_{\rm e}} > L_{\nu_x} \geq L_{\nu_{\rm e}}$, which is consistent with the results presented in [16]. This hierarchy is found to be preserved in most of the simulations at least until the first few milliseconds after the merger.

Looking at the ejecta properties, we observe an overall increase in the mass of the ejecta for simulations that feature higher total masses and larger asymmetry of the binary mass. For a given total mass, we find that higher temperatures are generated within the ejecta with a more spherical distribution of the ejecta mass per unit solid angle for mergers with greater asymmetry. Despite this increase in the temperatures of the ejected particles, we identify that the typical neutron richness of the dynamically ejected material in asymmetric mergers tends to be comparatively higher than that of their symmetric counterparts, consistent with the findings in other works [248, 92, 136, 120, 183, 40]. Specifically, the number of particles ejected from the larger radii of the central remnant is found to be comparatively higher than that of the symmetric mergers. These particles ejected from the larger radii experience less neutrino irradiation and do not change much of their $Y_{\rm e}$ values (from Eq. 2.18), thus preserving the neutron-richness of the material, and contributing less to the increase in the average $Y_{\rm e}$ value of the ejecta.

5.2. Systematic study of BNS mergers with pions

In the second part of the thesis, we investigate in detail the impact of pions on BNS mergers. For decades, the existence of pions has been speculated in the cores of NSs, but has been neglected in almost most of the currently available BNS merger simulations and the widely used EOS models. The study presented in this thesis is basically the first study of the impact of pions in the context of BNS mergers.

We use a temperature- and composition-dependent SFHo and DD2 EOSs [105, 104, 262, 275, 105, 276] and incorporate pions as a free, non-interacting Bose gas.

We consider both neutral and charged pions, which can exist as either condensate or thermal ones. We assume that the effective mass of the pion is constant under all thermodynamical conditions and consider three different chosen values of constant effective mass by adopting the vacuum mass of the pion, 170 MeV and 200 MeV.

Compared to models that do not include pions, the addition of pions leads to a softening of the EOS for isolated, cold NSs in neutrinoless beta-equilibrium. This is because the appearance of pions as a condensate does not add any additional pressure but affects the total pressure at a given Y_e by changing the composition, equilibrium conditions, and baryonic contribution. For a given NS mass, the introduction of pions results in a decrease in both the maximum mass and the radius of the NS, showing an inverse correlation with the chosen effective mass. As the effective mass of the pion approaches its vacuum value, the reduction in radii reaches a maximum of about $\sim 200\,\mathrm{m}$. In particular, the tidal deformability shows a potential variation of up to 10 percent when the pion mass is equal to its vacuum value. This shift could significantly influence the inference of the EOS from a GW analysis of the inspiral, especially if the microphysical parameters of nuclear matter used in EOS models do not consider the presence of pions.

We then conduct relativistic hydrodynamical simulations using various EOS models, both with and without the inclusion of pions. We do not find any qualitative differences concerning the general dynamics between simulations with and without pions. Although the treatment of weak interactions in our simulations is rather basic and only advects the initial electron fraction, we observe a significant change in the value of the electron fraction depending on the chosen value of the effective mass. A more sophisticated approach of weak interactions requires the inclusion of neutrinos. Since the presence of pions implicates the presence of muons, the inclusion of muons also become necessary. We provide a brief estimate of the potential impact of muons in the Appendix C. Our analysis suggests that while pions might substantially impact the stellar structure for effective pion masses near vacuum values, the introduction of muons yields relatively minor changes.

Analysing the GW signals from our simulations, we observed an increase in the dominant post-merger GW frequency, f_{peak}, up to 200 Hz in simulations with pions compared to the base model. This frequency shift is more pronounced in scenarios featuring smaller effective pion masses. We evaluate how these changes affect the empirical relationships established between the stellar parameters of NSs and the dominant post-merger frequency (e.g. [26, 27, 108, 30, 41, 264, 223, 143, 46, 274, 43, 280]) based on EOSs that neglect pions. We find that these established relationships still remain valid to good accuracy and justify the continued utilisation of these established relationships for EOS inference in GW observations. We also explore the effect of pions on the threshold binary mass M_{thres} for prompt BH formation. We observe that the overall softening of the EOS due to the presence of pions leads to a decrease in M_{thres} of up to $0.07\,M_\odot$, with a pronounced decrease for smaller pion masses. Despite these changes, the empirical relations for M_{thres} established based on models without pions [33] are still found to be valid.

Considering the mass ejection in BNS mergers, we find that the presence of pions results in an increase about a few tens of percent compared to models without pions. It has been reported that the properties of the ejected material such

as the mass of the ejecta, are related to the characteristics of non-rotating neutron stars [25, 109]. However, we observe that the increase in ejecta mass in models including pions is more substantial than one might expect solely based on the changes observed in the stellar parameters of cold, non-rotating stars. This discrepancy could potentially signify a systematic bias, impacting attempts to deduce stellar parameters of NSs from the observations of kilonovae. Nevertheless, we caution that ejecta properties are generally challenging to precisely determine and that there exist considerable uncertainties and inherent scatter in the relationships that describe kilonova features as a function of NS properties.

5.3. Outlook

We note that the simulations of the BNS mergers with neutrinos presented in chapter 3 are used as a starting point for many sophisticated kilonova models [55, 254, 56] and end-to-end models [122]. Despite the advances, these models still lack in explaining certain features of the kilonova AT2017gfo. Specifically, the mass of the ejecta obtained from our simulation (see Sec. 3.1) is quite low compared to the inferred mass of AT2017gfo, which is about a few $0.01 M_\odot$. This is due to the fact that all our simulations are run only until the first 20ms after the merger (because of the high computational costs) and thus consider only the dynamical ejection. It is important to note that our simulation does not collapse into a BH within this dynamical period and still continues to eject mass through different channels.

Thus, a computationally efficient, higher resolution, long-term simulation with an accurate modelling of neutrino transport is necessary to accurately describe the observed kilonova. In pursuit of this objective, our future goals are dedicated in terms of producing a large set of long-term simulations, for a parameter study with different binary masses, EOSs, ratios, and an extensive analysis of the results with nucleosynthesis and radiative transfer calculations.

In addition to kilonova modelling, it is also important to properly understand the systematic shifts observed in the dominant postmerger oscillation frequencies of asymmetric binaries discussed in Sec. 3.2.1. Many of the empirical relations in the literature [27, 26, 264, 41, 29, 43] that connect these frequencies to the stellar properties of a NS generally deal with equal mass binaries. It is of essential importance to understand how these observed systematic shifts affect these empirical relations when considering asymmetric mergers with different total masses and different EOSs. Future research work will also focus on this.

Regarding pions, further research needs to be conducted to improve the initial evaluation of the impact of pions on BNS mergers. We have described pions as a non-interacting Bose gas and selected a fixed pion mass, which only provides a rough description of the effective interactions at these high-densities. Therefore, it is essential to properly take into account these effective interactions [186, 117, 272, 80] and consider more EOS models. In addition, a more advanced analysis of weak interactions is also necessary to comprehend the effect of pions on the ejecta composition, since our basic simulations already suggest a potentially significant

influence. Specifically, the presence of pions affects the composition of NS matter, changes the electron fraction, and leads to the presence of muons from its decay channels. As a result, comprehensive studies that attempt to properly understand the impact of pions on the properties of the ejecta should include both muons and neutrinos. This is also one of our goals for future work.

In addition to the presence of pions, there exist a few hypotheses on the composition of NS matter at high densities. One of them is the presence of quarks in the cores of the NSs and another one is the presence of an additional cooling effect from the hypothesised axion-like particles. It is important to understand the effects of these subatomic particles on the EOS and the subsequent implications for nucleosynthesis and kilonova models. Thus, a detailed study of BNS merger simulations with neutrinos in the presence of quarks and BNS merger simulations with axion cooling in addition to the existing neutrino cooling, is planned in the very near future.

A. Comparison of a simulation with hybrid MPI parallelisation to a standard simulation

We implement a hybrid MPI parallelisation to overcome the high computational periods involved in the calculation of the diffusion timescale and in the absorption module as discussed in Sec. 2.2.2. Here, we make a detailed comparison of the all relevant hydro and thermodynamical quantities from a 1.375-1.375$M_\odot$ BNS merger simulation with hybrid MPI parallelisation (referred to as "MPI") with those from a corresponding standard simulation without MPI (referred to as "STD"). It is important to note that we do not expect the results to be exactly identical, since there exists intrinsic scatter in these simulations even for the same setup run twice. In addition, in simulations with MPI parallelisation, we also use the approximation where we keep the neutrino source terms constant and evolve them only on every second timestep, for a further speedup. Nevertheless, we expect the qualitative behaviour of the results to be highly similar.

In Fig. A.1, we provide a comparison of various parameters, including the minimum lapse function $\alpha_{\rm min}$, plus polarisation amplitude, the maximum density $\rho_{\rm max}$, the total luminosity of neutrinos, antineutrinos and heavy neutrinos, the maximum and the mass averaged temperature, the total ejecta mass and the mass averaged electron fraction, $Y_{\rm e}^{\rm mavg}$, between simulations with and without hybrid MPI parallelisation. Indeed, we find an agreement between the standard simulation (STD) and the one with hybrid MPI parallelisation (MPI). Despite some quantitative differences in the neutrino luminosity, they all behave very similar. Additionally, it is worth noting that the differences observed in certain quantities can be attributed to the neutrino grid size. In the standard simulation, the neutrino grid size is increased from 289 grid cells to 305 grid cells, depending on the number of particles outside the grid. Conversely, in simulations with hybrid MPI parallelisation, the grid size is maintained at 305 cells throughout the entire simulation period. This variation in grid sizes can account for some of the discrepancies observed in the simulation results.

In typical simulations utilising hybrid MPI parallelisation, we allocate a total of 20 processes distributed across 5 nodes, with 4 processes assigned to each node. Alongside MPI parallelisation, standard simulations also incorporate OpenMP (OMP) parallelisation. We typically employ 24 threads for OMP parallelisation, in addition to MPI. In total, each simulation utilises 480 cores over a period of

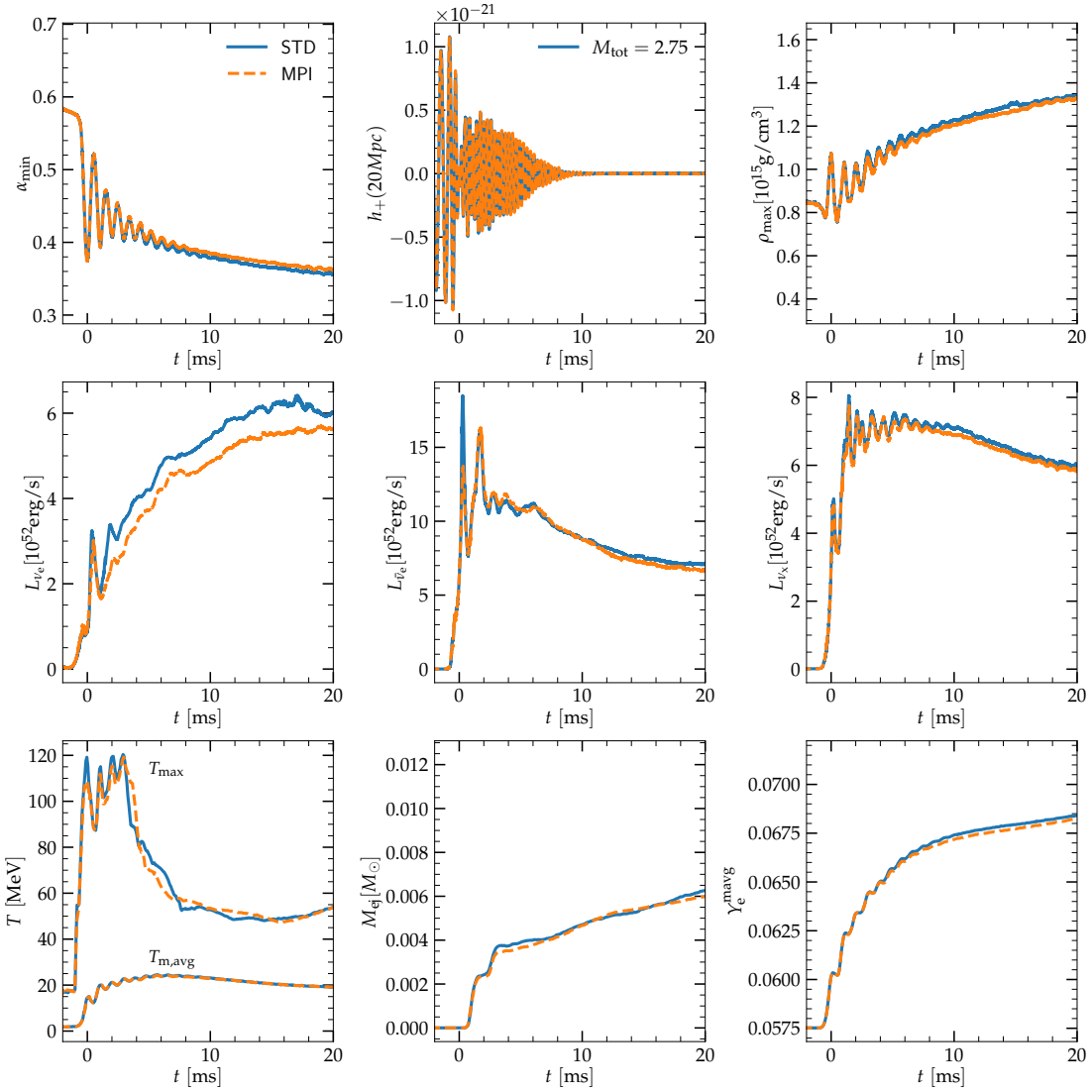

Figure A.1: Comparison of the hydro and thermodynamical quantities from a 1.375-1.375$M_\odot$ BNS merger simulation with hybrid MPI parallelization (MPI) and the respective standard simulation without MPI (STD). First row compares the minimum lapse function $\alpha_{\rm min}$, plus polarisation amplitude and the maximum density $\rho_{\rm max}$. Second row shows the total luminosity of neutrinos, anti-neutrinos and heavy neutrinos. And, the third row compares the maximum and average temperature, the total ejecta mass and the mass averaged electron fraction, $Y_{\rm e}^{\rm mavg}$.

3-4 weeks, covering several milliseconds post-merger. It is important to note that the simulation duration is highly dependent on factors such as the EOS, the total mass of the binary system, and other relevant parameters.

B. Neutrino grid cell resolution in SPH simulations

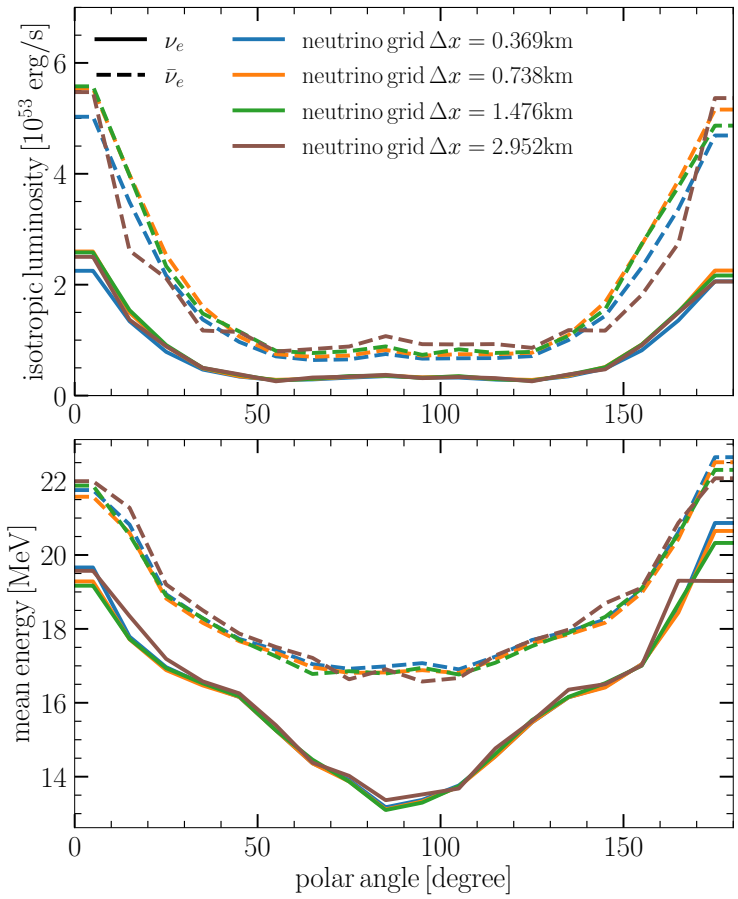

Figure B.1: The isotropic-equivalent luminosities (displayed on the top) and mean energies (shown at the bottom) are plotted as functions of polar angle for electron neutrinos (indicated by solid lines) and electron antineutrinos (represented by dashed lines). These results are obtained for various grid cell sizes Δx of the uniform Cartesian grid on which the ILEAS neutrino scheme is implemented. Taken from [122].

The neutrino scheme ILEAS, coupled to our SPH hydro solver calculates the source terms associated with neutrino emission and absorption on a uniform Carte-

sian grid. In this Appendix, we conduct a brief study to assess the influence of this grid resolution on basic neutrino quantities, following [122]. Conducting a comprehensive resolution study, especially considering a larger neutrino grid size involving a substantial number of grid cells throughout the entire dynamic evolution, demands extensive computational resources and memory requirements. Due to this limitation, we instead opt to choose a snapshot from our symmetric merger model used in [122] at $t_{\rm postmerger} \approx 5\,{\rm ms}$ and run only the neutrino evolution on it, keeping all hydrodynamic quantities fixed.

For various cases of the grid resolution Δx, Fig. B.1, top panel depicts the resulting polar-angle dependent isotropic-equivalent luminosities of neutrinos and antineutrinos, $L = 4\pi r^2 F_r$ (with radial neutrino flux F_r) measured at $r = 100\,{\rm km}$. The bottom panel depicts the same but the mean energy of neutrinos and antineutrinos, $\langle\epsilon\rangle$, measured at $r = 100\,{\rm km}$. The resolution dependence appears to be relatively gentle, implying that the grid cell size of $\Delta x = 0.738\,{\rm km}$ used in our regular dynamical simulations is adequate. This also guarantees that the discretization errors related to the grid are insignificant and that the results are valid, at least for the initial postmerger stage, lasting up to several tens of milliseconds [122].

C. Inclusion of Muons

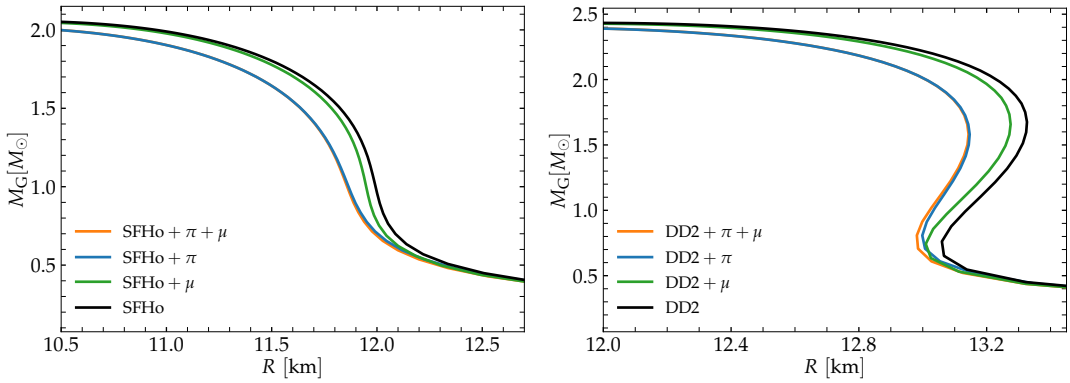

(a) SFHo (b) DD2

Figure C.1: Gravitational mass versus NS radius for the Base, Base+π, Base+μ and Base+π+μ models with SFHo(left) and DD2(right) as base model. Taken from [278].

In chapter 4, we focus on the impact of pions on BNS mergers. However, we do not consider muons, which one should expect to be also present in NS matter despite being neglected in many currently available EOS tables (see [45, 152, 12] for the incorporation of muons in simulations of core-collapse supernovae and neutron star mergers). From Fig. 4.11, one can observe that within a neutron star merger remnant, the chemical potential of electrons can readily reach the rest mass value of muons (i.e., 105.7 MeV) as one moves towards the centre of the remnant. Since muons are the dominant decay products of pions, a reliable modelling in principle should also account for the presence of muons. Given that our primary interest lies in the effects on the GW signal and the collapse behaviour, both of which are primarily determined by the high-density regime of the EOS, we evaluate the influence of muons by examining stellar equilibrium solutions of isolated stars, following [278].

The evaluation of muons in EOS tables is conceptually straightforward, as they can be treated as an ideal Fermi gas similar to electrons. However, adding muons to existing tables necessitates minor adaptations because the base models calculate the contributions of different constituents by assuming charge neutrality between protons, electrons, and positrons. The addition of muons and pions alters the conditions for charge neutrality. To incorporate muons into existing EOS tables,

we begin by removing the contributions from electrons (and positrons for $T > 0$) from the base model, similar to our approach for adding pions. Subsequently, at each point of the EOS table, we recompute the contributions of all considered leptons and pions, taking into account the updated relations for charge neutrality and chemical equilibrium. We analyse stellar configurations under conditions of zero temperature and neutrinoless β-equilibrium. Additionally, we explore stellar models at finite temperatures to simulate the behaviour of merger remnants. For this, we select a finite temperature of 20 MeV and maintain a fixed lepton fraction. At each point of the EOS table corresponding to this temperature, we solve the conditions for charge neutrality, assuming chemical equilibrium among the nucleons, leptons (including electrons, muons, their antiparticles, as well as the respective neutrinos and antineutrinos), and the pions. It is crucial to emphasise that this analysis is intended to estimate the influence on GWs and the bulk properties of NSs and BNS mergers. These properties are primarily determined by the high-density EOS, where the assumed conditions of chemical equilibrium are well justified.

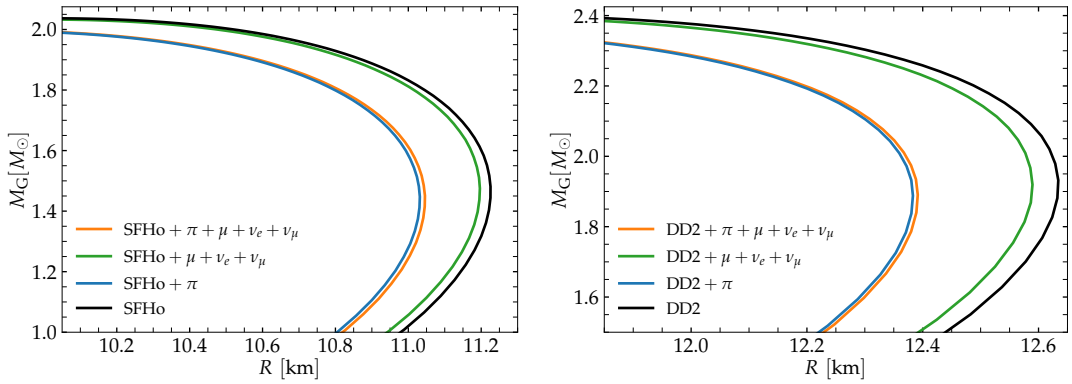

(a) SFHo (b) DD2

Figure C.2: Gravitational mass versus NS radius for the Base, Base + π, Base+μ+ν_e+ν_μ, Base+π+μ+ν_e+ν_μ for a fixed electronic lepton fraction $Y_{\mathrm{lep,e}} = 0.04$, and muonic lepton fraction $Y_{\mathrm{lep},\mu} = 0.015$ (if muon and muon neutrinos are present) at temperature $T = 20\,\mathrm{MeV}$ with SFHo(left) and DD2(right) as base models. For these calculations the surface of the stars is defined at a rest-mass density of $10^{14}\,\mathrm{g/cm^3}$. Taken from [278].

By following the described procedure, we create various versions of the EOS tables at zero temperature, using the SFHo and DD2 base models: the base model with pions only, the base models with muons only, and the base model with muons and pions. For each version, we establish the beta-equilibrium EOS at zero temperature and calculate TOV solutions. These TOV solutions are illustrated in Fig. C.1, with the left panel representing the model based on SFHo EOS and the right panel representing the model based on DD2 EOS.

Incorporating muons without pions results in a subtle softening of the EOS, leading to slightly smaller NS radii. However, the softening effect produced by the presence of pions is comparatively more significant than that produced by muons.

For example, it leads to a more substantial reduction in both the radius and the maximum mass of the NS. Remarkably, the inclusion of muons in an EOS already containing pions has an almost negligible impact. This result is expected because the presence of pions restricts the chemical potential difference $\mu_\mathrm{n} - \mu_\mathrm{p}$ to the mass of the pion. Therefore, in the context of neutrinoless beta-equilibrium, where $\mu_\mathrm{n} - \mu_\mathrm{p} = \mu_\mathrm{e} = \mu_\pi = \mu_\mu$, the production of muons is suppressed, and their impact on the EOS is limited as μ_μ cannot significantly increase. The suppression of muons is more restrictive in models with relatively small effective pion masses, making the neglection of muons a reasonable approximation. Nevertheless in scenarios where higher effective pion masses are considered, this suppression becomes less restrictive and the inclusion of muons in the EOS could become more relevant. In these situations where the inclusion of pions has a relatively minor impact on the EOS (as discussed in Sect. 4.3.1), the modifications introduced by muons might become somewhat more significant. This is evident from the case where only muons are considered in the base model.

In the case of finite-temperature EOS models where neutrinos are also considered (see Fig. C.2), we fix the electronic lepton fraction to $Y_\mathrm{lep,e} = 0.04$ and the muonic lepton fraction to $Y_\mathrm{lep,\mu} = 0.015$ (when muons and muon neutrinos are present). This configuration broadly approximates conditions within BNS merger remnants. In addition, since neutrino are completely trapped at these high-densities, we also assume that the initial electron and muon lepton fractions of the original cold NSs are approximately preserved during the merger. To more accurately evaluate the effect on the stellar structure, we focus exclusively on the NS core and its radius. This is achieved by computing TOV models while disregarding densities below 10^{14} g/cm^3. By doing so, we prevent the stellar models from being inflated by the finite temperature at lower densities.

Once again, we observe that the effect of muons is nearly negligible when pions are included, as is evident from the comparison between the blue and orange lines in Fig. C.2. The comparison between the various versions of EOS also indicates that ignoring neutrinos in our analysis can be justified, as they seem to have only a minor influence on the stellar structure. Therefore, for a first study in the context of evaluating the bulk properties of BNS mergers, such as GWs and the conditions for black-hole formation, it is a reasonable approximation to consider only pions and ignore muons in the simulations discussed in chapter 4.

List of publications

Papers used in this thesis:

[1] **Vimal Vijayan**, Ninoy Rahman, Andreas Bauswein, Gabriel Martínez-Pinedo, and Ignacio L. Arbina, "Impact of pions on binary neutron star mergers", *Phys. Rev. D* 108, 023020, July 2023.

[2] Oliver Just, **Vimal Vijayan**, Z. Xiong, S. Goriely, T. Soultanis, A. Bauswein, J. Guilet, H.-Th. Janka, and G. Martínez-Pinedo, "End-to-end Kilonova Models of Neutron Star Mergers with Delayed Black Hole Formation", *The Astrophysical Journal Letters*, Volume 951, July 2023.

[3] **Vimal Vijayan**, Andreas Bauswein, Gabriel Martinez-Pinedo, "Neutrinos and their impact on the nucleosynthesis in binary neutron star mergers", *PoS* FAIRness2022, 061, DOI: 10.22323/1.419.0061, June 2023.

[4] Christine E. Collins, Andreas Bauswein, Stuart A. Sim, **Vimal Vijayan**, Gabriel Martínez-Pinedo, Oliver Just, Luke J. Shingles, Markus Kromer, "3D radiative transfer kilonova modelling for binary neutron star merger simulations", *Monthly Notices of the Royal Astronomical Society*, Volume 521, Issue 2, May 2023.

Papers not used in this thesis:

[1] Christine E. Collins, Luke J. Shingles, Andreas Bauswein, Stuart A. Sim, Theodoros Soultanis, **Vimal Vijayan**, Andreas Floers, Oliver Just, Gerrit Leck, Gabriel Martínez-Pinedo, Albert Sneppen, Darach Watson, Zewei Xiong, "Towards inferring the geometry of kilonovae", *arXiv e-prints*, arXiv: 2309.05579, September 2023.

[2] Luke J. Shingles, Christine E. Collins, **Vimal Vijayan**, Andreas Flörs, Oliver Just, Gerrit Leck1, Zewei Xiong, Andreas Bauswein, Gabriel Martínez-Pinedo, and Stuart A. Sim, "Self-consistent 3D Radiative Transfer for Kilonovae: Directional Spectra from Merger Simulations", *The Astrophysical*

Journal Letters, Volume 954, September 2023.

[3] Andreas Bauswein, Sebastian Blacker, Georgios Lioutas, Theodoros Soultanis, **Vimal Vijayan**, and Nikolaos Stergioulas, "Systematics of prompt black-hole formation in neutron star mergers", *Phys. Rev. D* 103, 123004, June 2021.

[4] Andreas Bauswein, Sebastian Blacker, **Vimal Vijayan**, Nikolaos Stergioulas, Katerina Chatziioannou, James A. Clark, Niels-Uwe F. Bastian, David B. Blaschke, Mateusz Cierniak, and Tobias Fischer, "Equation of State Constraints from the Threshold Binary Mass for Prompt Collapse of Neutron Star Mergers", *Phys. Rev. Lett.* 125, 141103, September 2020.

Acknowledgments

First and foremost, I am immensely grateful to my supervisor Andreas Bauswein for his unwavering support over the past four years. He has been a constant source of guidance and encouragement, no matter the time or day, whether it be on weekdays, weekends, or holidays. He has always been interested in the progress of my works and provided me with valuable feedback. He never forces someone to do something, but rather allows you to have your own ideas and gives you all the freedom and encouragement to pursue things on your own. I have learnt a great deal from him, both in terms of science and life. I must say that I could not have asked for a better advisor.

I also want to thank Gabriel Martínez-Pinedo, the big boss of our theory group at GSI, and my collaborator in almost all the projects in which I was involved. He is one of the people I admire a lot, who knows so much in physics and still stays late every day than any of his students, and a great inspiration.

In addition, I also would like to express my appreciation to all the individuals with whom I had the opportunity to collaborate with various projects discussed in this thesis: Starting with Ricard Ardevol Pulpillo, Christine Collins, Ninoy Rahman, Oliver Just, Luke Shingles, Andreas Floers, Gerrit Leck, Zewei Xiong, Mario Jakobs, Thomas Neff, and others.

Specifically, I want to thank a few people at GSI who have made my life more enjoyable over the years, since it would be impossible to name them all in a single sentence. I would like to thank: Sebastian, my friend and my first company in the office, without whom I could not have learnt things on SPH as quickly as possible and would never have found all the beautiful hiking spots around Darmstadt to play in the snow. George for all the chaperoning by car, listening to all my stories, late night discussions, and the amazing fun in the office. Ignacio, for being my other hiking company, with whom I had a great time trying out so many physical activities outside of work. Christian, one of the other person who is responsible for all the joy in the office, with whom I have had a lot, both work discussions and completely unrelated discussions. Theodoros, for interesting conversations, pleasant moments, and listening to all my loud music next to my office. Zafar, for the wonderful spicy food. Diana, for being a good friend, my office mate for the past two years, and Aris for proofreading the first chapter.

In addition, I also wish to acknowledge some of the people who provided me with guidance and assistance throughout my studies. In particular Tomás Rodríguez and Luis Robledo for being my advisors during my masters, without whom I would never have found about the position at GSI. Jose Udias, for selecting

me for the Erasmus grant, without which things would have been very different. Sudharsan Ragunathan, Elankumaran Kannan, Gyaneshwaran Gomathinayagam for their guidance during my studies in India. Also, I am grateful for all the friends I made in Darmstadt, the many people I met during my studies in Italy, France, Spain, my childhood friends from Chennai, last but not least, my sister and my parents, for their endless love and support.

Furthermore, I also wish to thank Prof. Cornelis Dullemond for agreeing to be the second referee of this thesis, and, Prof. Manfred Lindner and Prof. Norbert Frank for joining my examination committee.

I would like to acknowledge the financial support by the Deutsche Forschungsgemeinschaft (DFG) - Project-ID 138713538 - SFB 881 ("The Milky Way System", subproject A10), and the European Research Council (ERC) under grant agreement No. 759253. Specifically, being the user with the highest usage, I want to thank GSI Helmholtzzentrum für Schwerionenforschung for providing an excellent workspace and computational resources via the Virgo and Kronos clusters.

Bibliography

[1] Abbott et al. Multi-messenger Observations of a Binary Neutron Star Merger. *Astrophys. J. Lett.*, 848(2):L12, October 2017.

[2] B. P. Abbott et al. A gravitational-wave standard siren measurement of the Hubble constant. , 551(7678):85–88, November 2017.

[3] B. P. Abbott et al. Gravitational Waves and Gamma-Rays from a Binary Neutron Star Merger: GW170817 and GRB 170817A. *Astrophys. J. Lett.*, 848(2):L13, October 2017.

[4] B. P. Abbott et al. GW170817: Observation of Gravitational Waves from a Binary Neutron Star Inspiral. *Phys. Rev. Lett.*, 119(16):161101, October 2017.

[5] B. P. Abbott et al. GW170817: Measurements of Neutron Star Radii and Equation of State. *Phys. Rev. Lett.*, 121(16):161101, October 2018.

[6] B. P. Abbott et al. Properties of the Binary Neutron Star Merger GW170817. *Physical Review X*, 9(1):011001, January 2019.

[7] B. P. Abbott et al. GW190425: Observation of a Compact Binary Coalescence with Total Mass ~ 3.4 $M_\odot$. *Astrophys. J. Lett.*, 892(1):L3, March 2020.

[8] Ernazar Abdikamalov, Adam Burrows, Christian D. Ott, Frank Löffler, Evan O'Connor, Joshua C. Dolence, and Erik Schnetter. A New Monte Carlo Method for Time-dependent Neutrino Radiation Transport. *Astrophys. J.*, 755(2):111, August 2012.

[9] Michalis Agathos, Francesco Zappa, Sebastiano Bernuzzi, Albino Perego, Matteo Breschi, and David Radice. Inferring prompt black-hole formation in neutron star mergers from gravitational-wave data. *Phys. Rev. D*, 101(4):044006, February 2020.

[10] A. Akmal and V. R. Pandharipande. Spin-isospin structure and pion condensation in nucleon matter. *Phys. Rev. C*, 56(4):2261–2279, October 1997.

[11] A. Akmal, V. R. Pandharipande, and D. G. Ravenhall. Equation of state of nucleon matter and neutron star structure. *Phys. Rev. C*, 58(3):1804–1828, September 1998.

[12] Mark Alford, Arus Harutyunyan, and Armen Sedrakian. Bulk Viscosity of Relativistic $npe\mu$ Matter in Neutron-Star Mergers. *Particles*, 5:361–376, September 2022.

[13] John Antoniadis, Paulo C. C. Freire, Norbert Wex, Thomas M. Tauris, Ryan S. Lynch, Marten H. van Kerkwijk, Michael Kramer, Cees Bassa, Vik S. Dhillon, Thomas Driebe, Jason W. T. Hessels, Victoria M. Kaspi, Vladislav I. Kondratiev, Norbert Langer, Thomas R. Marsh, Maura A. McLaughlin, Timothy T. Pennucci, Scott M. Ransom, Ingrid H. Stairs, Joeri van Leeuwen, Joris P. W. Verbiest, and David G. Whelan. A Massive Pulsar in a Compact Relativistic Binary. *Science*, 340(6131):448, April 2013.

[14] Iair Arcavi, Griffin Hosseinzadeh, D. Andrew Howell, Curtis McCully, Dovi Poznanski, Daniel Kasen, Jennifer Barnes, Michael Zaltzman, Sergiy Vasylyev, Dan Maoz, and Stefano Valenti. Optical emission from a kilonova following a gravitational-wave-detected neutron-star merger. , 551(7678):64–66, November 2017.

[15] A. Arcones and F. K. Thielemann. Neutrino-driven wind simulations and nucleosynthesis of heavy elements. *Journal of Physics G Nuclear Physics*, 40(1):013201, January 2013.

[16] R Ardevol-Pulpillo, H-T Janka, O Just, and A Bauswein. Improved leakage-equilibration-absorption scheme (ILEAS) for neutrino physics in compact object mergers. *Mon. Not. Roy. Astron. Soc.*, 485(4):4754–4789, mar 2019.

[17] Ricard Ardevol Pulpillo. *A new scheme to treat neutrino effects in neutron-star mergers: implementation, tests and applications*. PhD thesis, Technische Universität München, 2018.

[18] Richard Arnowitt, Stanley Deser, and Charles W. Misner. Republication of: The dynamics of general relativity. *General Relativity and Gravitation*, 40(9):1997–2027, September 2008.

[19] Zaven Arzoumanian et al. The NANOGrav 11-year Data Set: High-precision Timing of 45 Millisecond Pulsars. *Astrophys. J. Suppl.*, 235(2):37, April 2018.

[20] S. O. Bäckman and W. Weise. Calculation of the threshold for π^- condensation in neutron matter. *Physics Letters B*, 55(1):1–5, January 1975.

[21] Luca Baiotti and Luciano Rezzolla. Binary neutron star mergers: a review of Einstein's richest laboratory. *Rep. Prog. Phys.*, 80(9):096901, September 2017.

[22] Dinshaw S. Balsara. von neumann stability analysis of smoothed particle hydrodynamics—suggestions for optimal algorithms. *Journal of Computational Physics*, 121(2):357–372, 1995.

[23] Jennifer Barnes and Daniel Kasen. Effect of a High Opacity on the Light Curves of Radioactively Powered Transients from Compact Object Mergers. *Astrophys. J.*, 775(1):18, September 2013.

[24] A. Bauswein, T. W. Baumgarte, and H. T. Janka. Prompt Merger Collapse and the Maximum Mass of Neutron Stars. *Phys. Rev. Lett.*, 111(13):131101, September 2013.

[25] A. Bauswein, S. Goriely, and H. T. Janka. Systematics of Dynamical Mass Ejection, Nucleosynthesis, and Radioactively Powered Electromagnetic Signals from Neutron-star Mergers. *Astrophys. J.*, 773(1):78, August 2013.

[26] A. Bauswein and H. T. Janka. Measuring Neutron-Star Properties via Gravitational Waves from Neutron-Star Mergers. *Phys. Rev. Lett.*, 108(1):011101, January 2012.

[27] A. Bauswein, H.-T. Janka, K. Hebeler, and A. Schwenk. Equation-of-state dependence of the gravitational-wave signal from the ring-down phase of neutron-star mergers. *Phys. Rev. D*, 86:063001, Sep 2012.

[28] A. Bauswein, R. Oechslin, and H. T. Janka. Discriminating strange star mergers from neutron star mergers by gravitational-wave measurements. *Phys. Rev. D*, 81(2):024012, January 2010.

[29] A Bauswein and N Stergioulas. Spectral classification of gravitational-wave emission and equation of state constraints in binary neutron star mergers. *J. Phys. G: Nucl. Part. Phys.*, 46(11):113002, Sep 2019.

[30] A. Bauswein, N. Stergioulas, and H. T. Janka. Revealing the high-density equation of state through binary neutron star mergers. *Phys. Rev. D*, 90(2):023002, 2014.

[31] Andreas Bauswein, Niels-Uwe F. Bastian, David B. Blaschke, Katerina Chatziioannou, James A. Clark, Tobias Fischer, and Micaela Oertel. Identifying a First-Order Phase Transition in Neutron-Star Mergers through Gravitational Waves. *Phys. Rev. Lett.*, 122(6):061102, February 2019.

[32] Andreas Bauswein, Niels-Uwe Friedrich Bastian, David Blaschke, Katerina Chatziioannou, James Alexander Clark, Tobias Fischer, Hans-Thomas Janka, Oliver Just, Micaela Oertel, and Nikolaos Stergioulas. Equation-of-state constraints and the QCD phase transition in the era of gravitational-wave astronomy. *AIP Conference Proceedings*, 2127(1):020013, 2019.

[33] Andreas Bauswein, Sebastian Blacker, Georgios Lioutas, Theodoros Soultanis, Vimal Vijayan, and Nikolaos Stergioulas. Systematics of prompt black-hole formation in neutron star mergers. *Phys. Rev. D*, 103(12):123004, June 2021.

[34] Andreas Bauswein, Sebastian Blacker, Vimal Vijayan, Nikolaos Stergioulas, Katerina Chatziioannou, James A. Clark, Niels-Uwe F. Bastian, David B. Blaschke, Mateusz Cierniak, and Tobias Fischer. Equation of State Constraints from the Threshold Binary Mass for Prompt Collapse of Neutron Star Mergers. *Phys. Rev. Lett.*, 125:141103, Sep 2020.

[35] Andreas Bauswein, Oliver Just, Hans-Thomas Janka, and Nikolaos Stergioulas. Neutron-star Radius Constraints from GW170817 and Future Detections. *Astrophys. J. Lett.*, 850(2):L34, December 2017.

[36] Gordon Baym and Elliott Flowers. Pion condensation in neutron star matter: Equilibrium conditions and model calculations. *Nucl. Phys. A*, 222(1):29–64, April 1974.

[37] Gordon Baym, Tetsuo Hatsuda, Toru Kojo, Philip D. Powell, Yifan Song, and Tatsuyuki Takatsuka. From hadrons to quarks in neutron stars: a review. *Rep. Prog. Phys.*, 81(5):056902, May 2018.

[38] Edo Berger. Short-Duration Gamma-Ray Bursts. , 52:43–105, August 2014.

[39] Sebastiano Bernuzzi. Neutron star merger remnants. *General Relativity and Gravitation*, 52(11):108, November 2020.

[40] Sebastiano Bernuzzi, Matteo Breschi, Boris Daszuta, Andrea Endrizzi, Domenico Logoteta, Vsevolod Nedora, Albino Perego, David Radice, Federico Schianchi, Francesco Zappa, Ignazio Bombaci, and Nestor Ortiz. Accretion-induced prompt black hole formation in asymmetric neutron star mergers, dynamical ejecta, and kilonova signals. *Mon. Not. R. Astron. Soc.*, 497(2):1488–1507, September 2020.

[41] Sebastiano Bernuzzi, Tim Dietrich, and Alessandro Nagar. Modeling the Complete Gravitational Wave Spectrum of Neutron Star Mergers. *Phys. Rev. Lett.*, 115(9):091101, August 2015.

[42] Sebastiano Bernuzzi, David Radice, Christian D. Ott, Luke F. Roberts, Philipp Mösta, and Filippo Galeazzi. How loud are neutron star mergers? *Phys. Rev. D*, 94:024023, Jul 2016.

[43] Sebastian Blacker, Niels-Uwe F. Bastian, Andreas Bauswein, David B. Blaschke, Tobias Fischer, Micaela Oertel, Theodoros Soultanis, and Stefan Typel. Constraining the onset density of the hadron-quark phase transition with gravitational-wave observations. *Phys. Rev. D*, 102:123023, Dec 2020.

[44] S. A. Bludman and K. A. van Riper. Diffusion approximation to neutrino transport in dense matter. *Astrophys. J.*, 224:631–642, September 1978.

[45] R. Bollig, H.-T. Janka, A. Lohs, G. Martínez-Pinedo, C. J. Horowitz, and T. Melson. Muon creation in supernova matter facilitates neutrino-driven explosions. *Phys. Rev. Lett.*, 119(24):242702, dec 2017.

[46] Matteo Breschi, Sebastiano Bernuzzi, Francesco Zappa, Michalis Agathos, Albino Perego, David Radice, and Alessandro Nagar. Kilohertz gravitational waves from binary neutron star remnants: Time-domain model and constraints on extreme matter. *Phys. Rev. D*, 100(10):104029, November 2019.

[47] S. W. Bruenn. Stellar core collapse - Numerical model and infall epoch. *Astrophys. J. Suppl.*, 58:771–841, August 1985.

[48] S. W. Bruenn, J. R. Buchler, and W. R. Yueh. Neutrino Transport in Supernova Models: A Multigroup, Flux Limited Diffusion Scheme. , 59(2):261–284, December 1978.

[49] E. Margaret Burbidge, G. R. Burbidge, William A. Fowler, and F. Hoyle. Synthesis of the elements in stars. *Rev. Mod. Phys.*, 29:547–650, Oct 1957.

[50] Rubén M. Cabezón, Kuo-Chuan Pan, Matthias Liebendörfer, Takami Kuroda, Kevin Ebinger, Oliver Heinimann, Albino Perego, and Friedrich-Karl Thielemann. Core-collapse supernovae in the hall of mirrors. A three-dimensional code-comparison project. , 619:A118, November 2018.

[51] A. G. W. Cameron. A Revised Table of Abundances of the Elements. *Astrophys. J.*, 129:676, May 1959.

[52] Katerina Chatziioannou. Neutron-star tidal deformability and equation-of-state constraints. *Gen. Relativ. Gravit.*, 52(11):109, November 2020.

[53] Katerina Chatziioannou, James Alexander Clark, Andreas Bauswein, Margaret Millhouse, Tyson B. Littenberg, and Neil Cornish. Inferring the post-merger gravitational wave emission from binary neutron star coalescences. *Phys. Rev. D*, 96(12):124035, December 2017.

[54] Riccardo Ciolfi. Binary neutron star mergers after GW170817. *Frontiers in Astronomy and Space Sciences*, 7:27, 2020.

[55] Christine E. Collins, Andreas Bauswein, Stuart A. Sim, Vimal Vijayan, Gabriel Martínez-Pinedo, Oliver Just, Luke J. Shingles, and Markus Kromer. 3D radiative transfer kilonova modelling for binary neutron star merger simulations. *Mon. Not. R. Astron. Soc.*, 521(2):1858–1870, May 2023.

[56] Christine E. Collins, Luke J. Shingles, Andreas Bauswein, Stuart A. Sim, Theodoros Soultanis, Vimal Vijayan, Andreas Floers, Oliver Just, Gerrit Leck, Gabriel Martínez-Pinedo, Albert Sneppen, Darach Watson, and Zewei Xiong. Towards inferring the geometry of kilonovae. *arXiv e-prints*, page arXiv:2309.05579, September 2023.

[57] Michael W Coughlin, Tim Dietrich, Zoheyr Doctor, Daniel Kasen, Scott Coughlin, Anders Jerkstrand, Giorgos Leloudas, Owen McBrien, Brian D Metzger, Richard O'Shaughnessy, and Stephen J Smartt. Constraints on the neutron star equation of state from AT2017gfo using radiative transfer simulations. *Mon. Not. Roy. Astron. Soc.*, 480(3):3871–3878, aug 2018.

[58] Michael W. Coughlin et al. GROWTH on S190425z: Searching Thousands of Square Degrees to Identify an Optical or Infrared Counterpart to a Binary Neutron Star Merger with the Zwicky Transient Facility and Palomar Gattini-IR. *Astrophys. J. Lett.*, 885(1):L19, November 2019.

[59] D. A. Coulter, R. J. Foley, C. D. Kilpatrick, M. R. Drout, A. L. Piro, B. J. Shappee, M. R. Siebert, J. D. Simon, N. Ulloa, D. Kasen, B. F. Madore, A. Murguia-Berthier, Y. C. Pan, J. X. Prochaska, E. Ramirez-Ruiz, A. Rest, and C. Rojas-Bravo. Swope Supernova Survey 2017a (SSS17a), the optical counterpart to a gravitational wave source. *Science*, 358(6370):1556–1558, December 2017.

[60] John J. Cowan, Christopher Sneden, James E. Lawler, Ani Aprahamian, Michael Wiescher, Karlheinz Langanke, Gabriel Martínez-Pinedo, and Friedrich-Karl Thielemann. Origin of the heaviest elements: The rapid neutron-capture process. *Rev. Mod. Phys.*, 93(1):015002, January 2021.

[61] P. S. Cowperthwaite, E. Berger, V. A. Villar, B. D. Metzger, M. Nicholl, R. Chornock, P. K. Blanchard, W. Fong, R. Margutti, M. Soares-Santos, et al. The Electromagnetic Counterpart of the Binary Neutron Star Merger LIGO/Virgo GW170817. II. UV, Optical, and Near-infrared Light Curves and Comparison to Kilonova Models. *Astrophys. J. Lett.*, 848(2):L17, October 2017.

[62] H. T. Cromartie et al. Relativistic Shapiro delay measurements of an extremely massive millisecond pulsar. *Nature Astronomy*, 4:72–76, January 2020.

[63] Sanjana Curtis, Philipp Mösta, Zhenyu Wu, David Radice, Luke Roberts, Giacomo Ricigliano, and Albino Perego. r-process nucleosynthesis and kilonovae from hypermassive neutron star post-merger remnants. *Mon. Not. R. Astron. Soc.*, 518(4):5313–5322, February 2023.

[64] Leonardo Dagum and Ramesh Menon. Openmp: An industry-standard api for shared-memory programming. *IEEE Comput. Sci. Eng.*, 5(1):46–55, jan 1998.

[65] Soumi De, Daniel Finstad, James M. Lattimer, Duncan A. Brown, Edo Berger, and Christopher M. Biwer. Tidal Deformabilities and Radii of Neutron Stars from the Observation of GW170817. *Phys. Rev. Lett.*, 121(9):091102, August 2018.

[66] M. Brett Deaton, Matthew D. Duez, Francois Foucart, Evan O'Connor, Christian D. Ott, Lawrence E. Kidder, Curran D. Muhlberger, Mark A. Scheel, and Bela Szilagyi. Black Hole-Neutron Star Mergers with a Hot Nuclear Equation of State: Outflow and Neutrino-cooled Disk for a Low-mass, High-spin Case. *Astrophys. J.*, 776(1):47, October 2013.

[67] P. B. Demorest, T. Pennucci, S. M. Ransom, M. S. E. Roberts, and J. W. T. Hessels. A two-solar-mass neutron star measured using Shapiro delay. , 467(7319):1081–1083, October 2010.

[68] Tim Dietrich, Michael W. Coughlin, Peter T. H. Pang, Mattia Bulla, Jack Heinzel, Lina Issa, Ingo Tews, and Sarah Antier. Multimessenger constraints on the neutron-star equation of state and the Hubble constant. *Science*, 370(6523):1450–1453, December 2020.

[69] Tim Dietrich, Tanja Hinderer, and Anuradha Samajdar. Interpreting binary neutron star mergers: describing the binary neutron star dynamics, modelling gravitational waveforms, and analyzing detections. *Gen. Relativ. Gravit.*, 53(3):27, March 2021.

[70] Tim Dietrich and Maximiliano Ujevic. Modeling dynamical ejecta from binary neutron star mergers and implications for electromagnetic counterparts. *Class. Quantum Grav.*, 34(10):105014, apr 2017.

[71] Tiekuang Dong and Zhongzhou Ren. New calculations of α-decay half-lives by the Viola-Seaborg formula. *European Physical Journal A*, 26(1):69–72, October 2005.

[72] M. R. Drout, A. L. Piro, B. J. Shappee, C. D. Kilpatrick, J. D. Simon, C. Contreras, D. A. Coulter, R. J. Foley, M. R. Siebert, N. Morrell, K. Boutsia, et al. Light curves of the neutron star merger GW170817/SSS17a: Implications for r-process nucleosynthesis. *Science*, 358(6370):1570–1574, December 2017.

[73] M. Durante et al. All the fun of the FAIR: fundamental physics at the facility for antiproton and ion research. *Phys. Scripta*, 94(3):033001, 2019.

[74] David Eichler, Mario Livio, Tsvi Piran, and David N. Schramm. Nucleosynthesis, neutrino bursts and γ-rays from coalescing neutron stars. , 340(6229):126–128, 1989.

[75] Torleif Ericson and Wolfram Weise. *Pions and nuclei*. Number 74 in The International series of monographs on physics. Oxford University Press, New York, 1988.

[76] F. J. Fattoyev, J. Piekarewicz, and C. J. Horowitz. Neutron skins and neutron stars in the multimessenger era. *Phys. Rev. Lett.*, 120:172702, Apr 2018.

[77] Rodrigo Fernández and Brian D. Metzger. Delayed outflows from black hole accretion tori following neutron star binary coalescence. *Mon. Not. R. Astron. Soc.*, 435(1):502–517, October 2013.

[78] Rodrigo Fernández and Brian D. Metzger. Electromagnetic Signatures of Neutron Star Mergers in the Advanced LIGO Era. *Annu. Rev. Nucl. Part. Sci.*, 66(1):23–45, October 2016.

[79] Éanna É. Flanagan and Tanja Hinderer. Constraining neutron-star tidal Love numbers with gravitational-wave detectors. *Phys. Rev. D*, 77(2):021502, January 2008.

[80] Bryce Fore, Norbert Kaiser, Sanjay Reddy, and Neill C. Warrington. The mass of charged pions in neutron star matter. *arXiv e-prints*, January 2023.

[81] Bryce Fore and Sanjay Reddy. Pions in hot dense matter and their astrophysical implications. *Phys. Rev. C*, 101:035809, Mar 2020.

[82] Bryce Fore and Sanjay Reddy. Pions in hot dense matter and their astrophysical implications. *Phys. Rev. C*, 101(3):035809, March 2020.

[83] F. Foucart, D. Desai, W. Brege, M. D. Duez, D. Kasen, D. A. Hemberger, L. E. Kidder, H. P. Pfeiffer, and M. A. Scheel. Dynamical ejecta from precessing neutron star-black hole mergers with a hot, nuclear-theory based equation of state. *Classical and Quantum Gravity*, 34(4):044002, February 2017.

[84] F. Foucart, M. D. Duez, L. E. Kidder, R. Nguyen, H. P. Pfeiffer, and M. A. Scheel. Evaluating radiation transport errors in merger simulations using a monte carlo algorithm. *Phys. Rev. D*, 98:063007, Sep 2018.

[85] Francois Foucart. Neutrino transport in general relativistic neutron star merger simulations. *Living Reviews in Computational Astrophysics*, 9(1):1, December 2023.

[86] Francois Foucart, M. Brett Deaton, Matthew D. Duez, Evan O'Connor, Christian D. Ott, Roland Haas, Lawrence E. Kidder, Harald P. Pfeiffer, Mark A. Scheel, and Bela Szilagyi. Neutron star-black hole mergers with a nuclear equation of state and neutrino cooling: Dependence in the binary parameters. *Phys. Rev. D*, 90:024026, Jul 2014.

[87] Francois Foucart, Matthew D. Duez, Francois Hebert, Lawrence E. Kidder, Harald P. Pfeiffer, and Mark A. Scheel. Monte-Carlo Neutrino Transport in Neutron Star Merger Simulations. *Astrophys. J. Lett.*, 902(1):L27, October 2020.

[88] Francois Foucart, Roland Haas, Matthew D. Duez, Evan O'Connor, Christian D. Ott, Luke Roberts, Lawrence E. Kidder, Jonas Lippuner, Harald P. Pfeiffer, and Mark A. Scheel. Low mass binary neutron star mergers: Gravitational waves and neutrino emission. *Phys. Rev. D*, 93(4):044019, February 2016.

[89] Francois Foucart, Evan O'Connor, Luke Roberts, Matthew D. Duez, Roland Haas, Lawrence E. Kidder, Christian D. Ott, Harald P. Pfeiffer, Mark A. Scheel, and Bela Szilagyi. Post-merger evolution of a neutron star-black hole binary with neutrino transport. *Phys. Rev. D*, 91:124021, Jun 2015.

[90] Bengt Friman, Claudia Hohne, Jorn Knoll, Stefan Leupold, Jorgen Randrup, Ralf Rapp, and Peter Senger, editors. *The CBM physics book: Compressed baryonic matter in laboratory experiments*, volume 814. 2011.

[91] Sho Fujibayashi, Kenta Kiuchi, Nobuya Nishimura, Yuichiro Sekiguchi, and Masaru Shibata. Mass Ejection from the Remnant of a Binary Neutron Star Merger: Viscous-radiation Hydrodynamics Study. *Astrophys. J.*, 860(1):64, 2018.

[92] Sho Fujibayashi, Kenta Kiuchi, Shinya Wanajo, Koutarou Kyutoku, Yuichiro Sekiguchi, and Masaru Shibata. Comprehensive Study of Mass Ejection and Nucleosynthesis in Binary Neutron Star Mergers Leaving Short-lived Massive Neutron Stars. *Astrophys. J.*, 942(1):39, January 2023.

[93] Sho Fujibayashi, Yuichiro Sekiguchi, Kenta Kiuchi, and Masaru Shibata. Properties of Neutrino-driven Ejecta from the Remnant of a Binary Neutron Star Merger: Pure Radiation Hydrodynamics Case. *Astrophys. J.*, 846(2):114, September 2017.

[94] Edgar Gabriel, Graham E. Fagg, George Bosilca, Thara Angskun, Jack J. Dongarra, Jeffrey M. Squyres, Vishal Sahay, Prabhanjan Kambadur, Brian Barrett, Andrew Lumsdaine, Ralph H. Castain, David J. Daniel, Richard L. Graham, and Timothy S. Woodall. Open MPI: Goals, concept, and design of a next generation MPI implementation. In *Proceedings, 11th European PVM/MPI Users' Group Meeting*, pages 97–104, Budapest, Hungary, September 2004.

[95] R. A. Gingold and J. J. Monaghan. Smoothed particle hydrodynamics: theory and application to non-spherical stars. *Monthly Notices of the Royal Astronomical Society*, 181(3):375–389, 12 1977.

[96] D. Gizzi, C. Lundman, E. O'Connor, S. Rosswog, and A. Perego. Calibration of the Advanced Spectral Leakage scheme for neutron star merger simulations, and extension to smoothed-particle hydrodynamics. *Mon. Not. R. Astron. Soc.*, 505(2):2575–2593, August 2021.

[97] Davide Gizzi. *The Advanced Spectral Leakage (ASL) scheme for simulations of merging neutron stars*. PhD thesis, Stockholm University, Department of Astronomy, 2021.

[98] A. Goldstein et al. An Ordinary Short Gamma-Ray Burst with Extraordinary Implications: Fermi-GBM Detection of GRB 170817A. *Astrophys. J. Lett.*, 848(2):L14, October 2017.

[99] S. Goriely. Uncertainties in the solar system r-abundance distribution. , 342:881–891, February 1999.

[100] Stephane Goriely, Andreas Bauswein, and Hans-Thomas Janka. r-process Nucleosynthesis in Dynamically Ejected Matter of Neutron Star Mergers. *Astrophys. J. Lett.*, 738(2):L32, September 2011.

[101] P. Haensel, A. Y. Potekhin, and D. G. Yakovlev, editors. *Neutron Stars 1: Equation of State and Structure*, volume 326 of *Astrophysics and Space Science Library*. Springer, New York, 2007.

[102] Daryl Haggard, Melania Nynka, John J. Ruan, Vicky Kalogera, S. Bradley Cenko, Phil Evans, and Jamie A. Kennea. A Deep Chandra X-Ray Study of Neutron Star Coalescence GW170817. *Astrophys. J. Lett.*, 848(2):L25, October 2017.

[103] G. Hallinan et al. A radio counterpart to a neutron star merger. *Science*, 358(6370):1579–1583, December 2017.

[104] M. Hempel, T. Fischer, J. Schaffner-Bielich, and M. Liebendörfer. New Equations of State in Simulations of Core-collapse Supernovae. *Astrophys. J.*, 748:70, March 2012.

[105] Matthias Hempel and Jürgen Schaffner-Bielich. A statistical model for a complete supernova equation of state. *Nuclear Physics A*, 837(3-4):210–254, 2010.

[106] Tanja Hinderer. Tidal Love Numbers of Neutron Stars. *Astrophys. J.*, 677(2):1216–1220, apr 2008.

[107] Tanja Hinderer, Benjamin D. Lackey, Ryan N. Lang, and Jocelyn S. Read. Tidal deformability of neutron stars with realistic equations of state and their gravitational wave signatures in binary inspiral. *Phys. Rev. D*, 81:123016, Jun 2010.

[108] Kenta Hotokezaka, Kenta Kiuchi, Koutarou Kyutoku, Takayuki Muranushi, Yu-ichiro Sekiguchi, Masaru Shibata, and Keisuke Taniguchi. Remnant massive neutron stars of binary neutron star mergers: Evolution process and gravitational waveform. *Phys. Rev. D*, 88(4):044026, August 2013.

[109] Kenta Hotokezaka, Kenta Kiuchi, Koutarou Kyutoku, Hirotada Okawa, Yu-ichiro Sekiguchi, Masaru Shibata, and Keisuke Taniguchi. Mass ejection from the merger of binary neutron stars. *Phys. Rev. D*, 87(2):024001, January 2013.

[110] J. Isenberg and J. Nester. Canonical Gravity. In *General Relativity and Gravitation. Vol. 1. One hundred years after the birth of Albert Einstein. Edited by A. Held. New York*, volume 1, page 23, January 1980.

[111] Chikako Ishizuka, Akira Ohnishi, Kohsuke Tsubakihara, Kohsuke Sumiyoshi, and Shoichi Yamada. Tables of hyperonic matter equation of state for core-collapse supernovae. *J. Phys. G: Nucl. Part. Phys.*, 35(8):085201, August 2008.

[112] H. T. Janka and W. Hillebrandt. Monte Carlo simulations of neutrino transport in type II supernovae. , 78:375–397, 1989.

[113] H. T. Janka and W. Hillebrandt. Neutrino emission from type II supernovae : an analysis of the spectra. , 224:49–56, October 1989.

[114] H. Th. Janka. Flux-limited neutrino diffusion versus Monte Carlo neutrino transport. , 256(2):452–458, March 1992.

[115] H. Th. Janka. Conditions for shock revival by neutrino heating in core-collapse supernovae. , 368:527–560, March 2001.

[116] H. Thomas Janka and Andreas Bauswein. Dynamics and Equation of State Dependencies of Relevance for Nucleosynthesis in Supernovae and Neutron Star Mergers. *arXiv e-prints*, December 2022.

[117] Christopher Jung, Fabian Rennecke, Ralf-Arno Tripolt, Lorenz von Smekal, and Jochen Wambach. In-medium spectral functions of vector- and axial-vector mesons from the functional renormalization group. *Phys. Rev. D*, 95(3):036020, February 2017.

[118] O. Just, A. Bauswein, R. Ardevol Pulpillo, S. Goriely, and H. T. Janka. Comprehensive nucleosynthesis analysis for ejecta of compact binary mergers. *Mon. Not. R. Astron. Soc.*, 448(1):541–567, March 2015.

[119] O. Just, S. Goriely, H. Th Janka, S. Nagataki, and A. Bauswein. Neutrino absorption and other physics dependencies in neutrino-cooled black hole accretion discs. *Mon. Not. R. Astron. Soc.*, 509(1):1377–1412, January 2022.

[120] O Just, I Kullmann, S Goriely, A Bauswein, H-T Janka, and C E Collins. Dynamical ejecta of neutron star mergers with nucleonic weak processes – II: kilonova emission. *Mon. Not. Roy. Astron. Soc.*, 510(2):2820–2840, nov 2021.

[121] O. Just, M. Obergaulinger, and H. T. Janka. A new multidimensional, energy-dependent two-moment transport code for neutrino-hydrodynamics. *Mon. Not. R. Astron. Soc.*, 453(4):3386–3413, November 2015.

[122] O. Just, V. Vijayan, Z. Xiong, S. Goriely, T. Soultanis, A. Bauswein, J. Guilet, H. Th. Janka, and G. Martínez-Pinedo. End-to-end Kilonova Models of Neutron Star Mergers with Delayed Black Hole Formation. *Astrophys. J. Lett.*, 951(1):L12, 2023.

[123] Daniel Kasen, N. R. Badnell, and Jennifer Barnes. Opacities and Spectra of the r-process Ejecta from Neutron Star Mergers. *Astrophys. J.*, 774(1):25, September 2013.

[124] Daniel Kasen, Brian Metzger, Jennifer Barnes, Eliot Quataert, and Enrico Ramirez-Ruiz. Origin of the heavy elements in binary neutron-star mergers from a gravitational-wave event. , 551(7678):80–84, November 2017.

[125] Rahul Kashyap, Abhishek Das, David Radice, Surendra Padamata, Aviral Prakash, Domenico Logoteta, Albino Perego, Daniel A. Godzieba, Sebastiano Bernuzzi, Ignazio Bombaci, Farrukh J. Fattoyev, Brendan T. Reed, and André da Silva Schneider. Numerical relativity simulations of prompt collapse mergers: Threshold mass and phenomenological constraints on neutron star properties after GW170817. *Phys. Rev. D*, 105(10):103022, May 2022.

[126] M. M. Kasliwal et al. Illuminating gravitational waves: A concordant picture of photons from a neutron star merger. *Science*, 358(6370):1559–1565, December 2017.

[127] Timothy L. Kay and James T. Kajiya. Ray tracing complex scenes. *SIGGRAPH Comput. Graph.*, 20(4):269–278, Aug 1986.

[128] Mathias Th. Keil, Georg G. Raffelt, and Hans-Thomas Janka. Monte Carlo Study of Supernova Neutrino Spectra Formation. *Astrophys. J.*, 590(2):971–991, 2003.

[129] J. Keller, K. Hebeler, and A. Schwenk. Nuclear equation of state for arbitrary proton fraction and temperature based on chiral effective field theory and a Gaussian process emulator. *arXiv e-prints*, April 2022.

[130] Kenta Kiuchi, Koutarou Kyutoku, Masaru Shibata, and Keisuke Taniguchi. Revisiting the Lower Bound on Tidal Deformability Derived by AT 2017gfo. *Astrophys. J. Lett.*, 876(2):L31, May 2019.

[131] Kenta Kiuchi, Yuichiro Sekiguchi, Koutarou Kyutoku, and Masaru Shibata. Gravitational waves, neutrino emissions and effects of hyperons in binary neutron star mergers. *Classical and Quantum Gravity*, 29(12):124003, 2012.

[132] Maximilian Kölsch, Tim Dietrich, Maximiliano Ujevic, and Bernd Brügmann. Investigating the mass-ratio dependence of the prompt-collapse threshold with numerical-relativity simulations. *Phys. Rev. D*, 106(4):044026, August 2022.

[133] Sven Köppel, Luke Bovard, and Luciano Rezzolla. A General-relativistic Determination of the Threshold Mass to Prompt Collapse in Binary Neutron Star Mergers. *Astrophys. J. Lett.*, 872(1):L16, February 2019.

[134] O. Korobkin, S. Rosswog, A. Arcones, and C. Winteler. On the astrophysical robustness of the neutron star merger r-process. *Mon. Not. R. Astron. Soc.*, 426(3):1940–1949, November 2012.

[135] Christian J. Krüger and Francois Foucart. Estimates for disk and ejecta masses produced in compact binary mergers. *Phys. Rev. D*, 101:103002, May 2020.

[136] I Kullmann, S Goriely, O Just, R Ardevol-Pulpillo, A Bauswein, and H-T Janka. Dynamical ejecta of neutron star mergers with nucleonic weak processes – I: nucleosynthesis. *Mon. Not. Roy. Astron. Soc.*, 510(2):2804–2819, nov 2021.

[137] Koutarou Kyutoku, Kenta Kiuchi, Yuichiro Sekiguchi, Masaru Shibata, and Keisuke Taniguchi. Neutrino transport in black hole-neutron star binaries: Neutrino emission and dynamical mass ejection. *Phys. Rev. D*, 97:023009, Jan 2018.

[138] J. M. Lattimer and D. N. Schramm. Black-Hole-Neutron-Star Collisions. *Astrophys. J. Lett.*, 192:L145, September 1974.

[139] J. M. Lattimer and D. N. Schramm. The tidal disruption of neutron stars by black holes in close binaries. *Astrophys. J.*, 210:549–567, December 1976.

[140] James M. Lattimer. The Nuclear Equation of State and Neutron Star Masses. *Annu. Rev. Nucl. Part. Sci.*, 62(1):485–515, November 2012.

[141] James M. Lattimer. Constraints on nuclear symmetry energy parameters. *Particles*, 6(1):30–56, 2023.

[142] Luis Lehner, Steven L. Liebling, Carlos Palenzuela, O. L. Caballero, Evan O'Connor, Matthew Anderson, and David Neilsen. Unequal mass binary neutron star mergers and multimessenger signals. *Classical and Quantum Gravity*, 33(18):184002, September 2016.

[143] Luis Lehner, Steven L. Liebling, Carlos Palenzuela, O. L. Caballero, Evan O'Connor, Matthew Anderson, and David Neilsen. Unequal mass binary neutron star mergers and multimessenger signals. *Class. Quantum Grav.*, 33(18):184002, September 2016.

[144] Luis Lehner, Steven L. Liebling, Carlos Palenzuela, and Patrick M. Motl. $m = 1$ instability and gravitational wave signal in binary neutron star mergers. *Phys. Rev. D*, 94:043003, Aug 2016.

[145] C. D. Levermore and G. C. Pomraning. A flux-limited diffusion theory. *Astrophys. J.*, 248:321–334, August 1981.

[146] Li-Xin Li and Bohdan Paczyński. Transient Events from Neutron Star Mergers. *Astrophys. J. Lett.*, 507(1):L59–L62, November 1998.

[147] Richard W. Lindquist. Relativistic transport theory. *Annals of Physics*, 37(3):487–518, May 1966.

[148] Georgios Lioutas. *Binary neutron star merger simulations on a moving mesh*. Dissertation, Heidelberg University, 2022. Dissertation, Heidelberg University, 2022.

[149] Georgios Lioutas, Andreas Bauswein, and Nikolaos Stergioulas. Frequency deviations in universal relations of isolated neutron stars and postmerger remnants. *Phys. Rev. D*, 104:043011, Aug 2021.

[150] Jonas Lippuner and Luke F. Roberts. r-process Lanthanide Production and Heating Rates in Kilonovae. *Astrophys. J.*, 815(2):82, December 2015.

[151] Pok Man Lo, Bengt Friman, Michał Marczenko, Krzysztof Redlich, and Chihiro Sasaki. Repulsive interactions and their effects on the thermodynamics of a hadron gas. *Phys. Rev. C*, 96(1):015207, 2017.

[152] Eleonora Loffredo, Albino Perego, Domenico Logoteta, and Marica Branchesi. Muons in the aftermath of Neutron Star Mergers and their impact on Trapped Neutrinos. *arXiv e-prints*, September 2022.

[153] L. B. Lucy. A numerical approach to the testing of the fission hypothesis. , 82:1013–1024, December 1977.

[154] Ben Margalit and Brian D. Metzger. Constraining the Maximum Mass of Neutron Stars from Multi-messenger Observations of GW170817. *Astrophys. J. Lett.*, 850(2):L19, December 2017.

[155] R. Margutti et al. The Electromagnetic Counterpart of the Binary Neutron Star Merger LIGO/Virgo GW170817. V. Rising X-Ray Emission from an Off-axis Jet. *Astrophys. J. Lett.*, 848(2):L20, October 2017.

[156] Ronald W. Mayle, Marco Tavani, and James R. Wilson. Pions, Supernovae, and the Supranuclear Matter Density Equation of State. *Astrophys. J.*, 418:398, November 1993.

[157] Joel de Jesús Mendoza-Temis, Meng-Ru Wu, Karlheinz Langanke, Gabriel Martínez-Pinedo, Andreas Bauswein, and Hans-Thomas Janka. Nuclear robustness of the r process in neutron-star mergers. *Phys. Rev. C*, 92:055805, Nov 2015.

[158] B. D. Metzger, G. Martínez-Pinedo, S. Darbha, E. Quataert, A. Arcones, D. Kasen, R. Thomas, P. Nugent, I. V. Panov, and N. T. Zinner. Electromagnetic counterparts of compact object mergers powered by the radioactive decay of r-process nuclei. *Mon. Not. R. Astron. Soc.*, 406(4):2650–2662, August 2010.

[159] Brian D. Metzger. Kilonovae. *Living Reviews in Relativity*, 20(1):3, May 2017.

[160] Brian D. Metzger. Kilonovae. *Living Reviews in Relativity*, 23(1):1, December 2019.

[161] Brian D. Metzger, Andreas Bauswein, Stephane Goriely, and Daniel Kasen. Neutron-powered precursors of kilonovae. *Mon. Not. R. Astron. Soc.*, 446(1):1115–1120, January 2015.

[162] Brian D. Metzger and Rodrigo Fernández. Red or blue? A potential kilonova imprint of the delay until black hole formation following a neutron star merger. *Mon. Not. R. Astron. Soc.*, 441(4):3444–3453, 2014.

[163] A. Mezzacappa and O. E. B. Messer. Neutrino transport in core collapse supernovae. *Journal of Computational and Applied Mathematics*, 109(1):281–319, September 1999.

[164] A. B. Migdal. Phase transitions (π-condensation) in nuclei and neutron stars. *Physics Letters B*, 45(5):448–450, August 1973.

[165] A. B. Migdal. Pion fields in nuclear matter. *Rev. Mod. Phys.*, 50(1):107–172, January 1978.

[166] A. B. Migdal, E. E. Saperstein, M. A. Troitsky, and D. N. Voskresensky. Pion degrees of freedom in nuclear matter. *Phys. Rep.*, 192(4-6):179–437, September 1990.

[167] D. Mihalas and B. W. Mihalas. *Foundations of radiation hydrodynamics*. 1984.

[168] M. C. Miller, F. K. Lamb, A. J. Dittmann, S. Bogdanov, Z. Arzoumanian, K. C. Gendreau, S. Guillot, W. C. G. Ho, J. M. Lattimer, M. Loewenstein, S. M. Morsink, P. S. Ray, M. T. Wolff, C. L. Baker, T. Cazeau, S. Manthripragada, C. B. Markwardt, T. Okajima, S. Pollard, I. Cognard, H. T. Cromartie, E. Fonseca, L. Guillemot, M. Kerr, A. Parthasarathy, T. T. Pennucci, S. Ransom, and I. Stairs. The Radius of PSR J0740+6620 from NICER and XMM-Newton Data. *Astrophys. J. Lett.*, 918(2):L28, September 2021.

[169] G. N. Minerbo. Maximum entropy Eddington factors. , 20(6):541–545, January 1978.

[170] P. Moller, J.R. Nix, W.D. Myers, and W.J. Swiatecki. Nuclear ground-state masses and deformations. *Atomic Data and Nuclear Data Tables*, 59(2):185–381, 1995.

[171] Peter Möller, Bernd Pfeiffer, and Karl-Ludwig Kratz. New calculations of gross β-decay properties for astrophysical applications: Speeding-up the classical r process. *Phys. Rev. C*, 67:055802, May 2003.

[172] J. J. Monaghan. Smoothed particle hydrodynamics. , 30:543–574, January 1992.

[173] J.J. Monaghan. Sph and riemann solvers. *Journal of Computational Physics*, 136(2):298–307, 1997.

[174] K. P. Mooley, A. T. Deller, O. Gottlieb, E. Nakar, G. Hallinan, S. Bourke, D. A. Frail, A. Horesh, A. Corsi, and K. Hotokezaka. Superluminal motion of a relativistic jet in the neutron-star merger GW170817. , 561(7723):355–359, September 2018.

[175] W. D. Myers and W. J. Świątecki. Thomas-fermi fission barriers. *Phys. Rev. C*, 60:014606, Jun 1999.

[176] Ehud Nakar. Short-hard gamma-ray bursts. , 442(1-6):166–236, April 2007.

[177] Ehud Nakar. The electromagnetic counterparts of compact binary mergers. *Phys. Rep.*, 886:1–84, November 2020.

[178] Ehud Nakar, Ore Gottlieb, Tsvi Piran, Mansi. M. Kasliwal, and Gregg Hallinan. From γ to Radio: The Electromagnetic Counterpart of GW170817. *Astrophys. J.*, 867(1):18, November 2018.

[179] Ken'Ichiro Nakazato, Kohsuke Sumiyoshi, and Shoichi Yamada. Astrophysical implications of equation of state for hadron-quark mixed phase: Compact stars and stellar collapses. *Phys. Rev. D*, 77(10):103006, May 2008.

[180] Ken'ichiro Nakazato, Kohsuke Sumiyoshi, and Shoichi Yamada. Impact of Quarks and Pions on Dynamics and Neutrino Signal of Black Hole Formation in Non-rotating Stellar Core Collapse. *Astrophys. J.*, 721(2):1284–1294, October 2010.

[181] Ramesh Narayan, Bohdan Paczynski, and Tsvi Piran. Gamma-Ray Bursts as the Death Throes of Massive Binary Stars. *Astrophys. J. Lett.*, 395:L83, August 1992.

[182] Vsevolod Nedora, Sebastiano Bernuzzi, David Radice, Boris Daszuta, Andrea Endrizzi, Albino Perego, Aviral Prakash, Mohammadtaher Safarzadeh, Federico Schianchi, and Domenico Logoteta. Numerical Relativity Simulations of the Neutron Star Merger GW170817: Long-term Remnant Evolutions, Winds, Remnant Disks, and Nucleosynthesis. *Astrophys. J.*, 906(2):98, January 2021.

[183] Vsevolod Nedora, Federico Schianchi, Sebastiano Bernuzzi, David Radice, Boris Daszuta, Andrea Endrizzi, Albino Perego, Aviral Prakash, and Francesco Zappa. Mapping dynamical ejecta and disk masses from numerical relativity simulations of neutron star mergers. *Class. Quantum Grav.*, 39(1):015008, dec 2021.

[184] David Neilsen, Steven L. Liebling, Matthew Anderson, Luis Lehner, Evan O'Connor, and Carlos Palenzuela. Magnetized neutron stars with realistic equations of state and neutrino cooling. *Phys. Rev. D*, 89:104029, May 2014.

[185] M. Nicholl et al. The electromagnetic counterpart of the binary neutron star merger ligo/virgo gw170817. iii. optical and uv spectra of a blue kilonova from fast polar ejecta. *The Astrophysical Journal Letters*, 848(2):L18, oct 2017.

[186] Hiroki Nishihara and Masayasu Harada. Equation of state in the pion condensation phase in asymmetric nuclear matter using a holographic QCD model. *Phys. Rev. D*, 90(11):115027, December 2014.

[187] M. Obergaulinger, H. Th. Janka, and M. A. Aloy. Magnetic field amplification and magnetically supported explosions of collapsing, non-rotating stellar cores. *Mon. Not. R. Astron. Soc.*, 445(3):3169–3199, December 2014.

[188] Evan O'Connor. An Open-source Neutrino Radiation Hydrodynamics Code for Core-collapse Supernovae. *Astrophys. J. Suppl.*, 219(2):24, August 2015.

[189] Evan O'Connor, Robert Bollig, Adam Burrows, Sean Couch, Tobias Fischer, Hans-Thomas Janka, Kei Kotake, Eric J. Lentz, Matthias Liebendörfer, O. E. Bronson Messer, Anthony Mezzacappa, Tomoya Takiwaki, and David Vartanyan. Global comparison of core-collapse supernova simulations in spherical symmetry. *Journal of Physics G Nuclear Physics*, 45(10):104001, October 2018.

[190] Evan O'Connor and Christian D. Ott. A new open-source code for spherically symmetric stellar collapse to neutron stars and black holes. *Classical and Quantum Gravity*, 27(11):114103, 2010.

[191] Evan O'Connor and Christian D. Ott. The Progenitor Dependence of the Pre-explosion Neutrino Emission in Core-collapse Supernovae. *Astrophys. J.*, 762(2):126, January 2013.

[192] Evan P. O'Connor and Sean M. Couch. Two-dimensional Core-collapse Supernova Explosions Aided by General Relativity with Multidimensional Neutrino Transport. *Astrophys. J.*, 854(1):63, February 2018.

[193] R. Oechslin, H.-T. Janka, and A. Marek. Relativistic neutron star merger simulations with non-zero temperature equations of state. *Astron. & Astrophys.*, 467(2):395–409, mar 2007.

[194] Roland Oechslin, Stephan Rosswog, and Friedrich-Karl Thielemann. Conformally flat smoothed particle hydrodynamics application to neutron star mergers. *Phys. Rev. D*, 65:103005, May 2002.

[195] M. Oertel, A. F. Fantina, and J. Novak. Extended equation of state for core-collapse simulations. *Phys. Rev. C*, 85(5):055806, May 2012.

[196] M. Oertel, M. Hempel, T. Klähn, and S. Typel. Equations of state for supernovae and compact stars. *Rev. Mod. Phys.*, 89(1):015007, January 2017.

[197] J. R. Oppenheimer and G. M. Volkoff. On massive neutron cores. *Phys. Rev.*, 55:374–381, Feb 1939.

[198] J. R. Oppenheimer and G. M. Volkoff. On Massive Neutron Cores. *Phys. Rev.*, 55(4):374–381, February 1939.

[199] Feryal Özel and Paulo Freire. Masses, Radii, and the Equation of State of Neutron Stars. , 54:401–440, September 2016.

[200] P.A. Zyla, et al. (Particle Data Group). Review of Particle Physics. *Progress of Theoretical and Experimental Physics*, 2020(8):083C01, August 2020.

[201] Carlos Palenzuela, Steven L. Liebling, David Neilsen, Luis Lehner, O. L. Caballero, Evan O'Connor, and Matthew Anderson. Effects of the microphysical equation of state in the mergers of magnetized neutron stars with neutrino cooling. *Phys. Rev. D*, 92(4):044045, August 2015.

[202] Kuo-Chuan Pan, Carlos Mattes, Evan P. O'Connor, Sean M. Couch, Albino Perego, and Almudena Arcones. The impact of different neutrino transport methods on multidimensional core-collapse supernova simulations. *Journal of Physics G Nuclear Physics*, 46(1):014001, January 2019.

[203] Panov, I. V., Korneev, I. Yu., Rauscher, T., Martínez-Pinedo, G., Keli´c-Heil, A., Zinner, N. T., and Thielemann, F.-K. Neutron-induced astrophysical reaction rates for translead nuclei*. *A&A*, 513:A61, 2010.

[204] A. Perego, R. M. Cabezón, and R. Käppeli. An Advanced Leakage Scheme for Neutrino Treatment in Astrophysical Simulations. *Astrophys. J. Suppl.*, 223(2):22, April 2016.

[205] A. Perego, S. Rosswog, R. M. Cabezón, O. Korobkin, R. Käppeli, A. Arcones, and M. Liebendörfer. Neutrino-driven winds from neutron star merger remnants. *Mon. Not. R. Astron. Soc.*, 443(4):3134–3156, October 2014.

[206] A. Perego, F. K. Thielemann, and G. Cescutti. r-Process Nucleosynthesis from Compact Binary Mergers. In *Handbook of Gravitational Wave Astronomy*, page 13. 2021.

[207] Albino Perego, Sebastiano Bernuzzi, and David Radice. Thermodynamics conditions of matter in neutron star mergers. *Eur. Phys. J. A*, 55(8):124, August 2019.

[208] Bruno Peres, Micaela Oertel, and Jérôme Novak. Influence of pions and hyperons on stellar black hole formation. *Phys. Rev. D*, 87(4):043006, February 2013.

[209] J. Piekarewicz. The Nuclear Physics of Neutron Stars. *arXiv e-prints*, September 2022.

[210] J. A. Pons, J. M. Ibáñez, and J. A. Miralles. Hyperbolic character of the angular moment equations of radiative transfer and numerical methods. *Mon. Not. R. Astron. Soc.*, 317(3):550–562, September 2000.

[211] Y. Z. Qian and S. E. Woosley. Nucleosynthesis in Neutrino-driven Winds. I. The Physical Conditions. *Astrophys. J.*, 471:331, November 1996.

[212] David Radice. General-relativistic Large-eddy Simulations of Binary Neutron Star Mergers. *Astrophys. J. Lett.*, 838(1):L2, March 2017.

[213] David Radice, Sebastiano Bernuzzi, Walter Del Pozzo, Luke F. Roberts, and Christian D. Ott. Probing Extreme-density Matter with Gravitational-wave Observations of Binary Neutron Star Merger Remnants. *Astrophys. J. Lett.*, 842(2):L10, 2017.

[214] David Radice, Sebastiano Bernuzzi, and Albino Perego. The Dynamics of Binary Neutron Star Mergers and GW170817. *Annu. Rev. Nucl. Part. Sci.*, 70:95–119, October 2020.

[215] David Radice and Liang Dai. Multimessenger parameter estimation of GW170817. *European Physical Journal A*, 55(4):50, April 2019.

[216] David Radice, Filippo Galeazzi, Jonas Lippuner, Luke F. Roberts, Christian D. Ott, and Luciano Rezzolla. Dynamical mass ejection from binary neutron star mergers. *Mon. Not. R. Astron. Soc.*, 460(3):3255–3271, August 2016.

[217] David Radice, Albino Perego, Kenta Hotokezaka, Steven A. Fromm, Sebastiano Bernuzzi, and Luke F. Roberts. Binary Neutron Star Mergers: Mass Ejection, Electromagnetic Counterparts, and Nucleosynthesis. *Astrophys. J.*, 869(2):130, December 2018.

[218] David Radice, Albino Perego, Francesco Zappa, and Sebastiano Bernuzzi. GW170817: Joint Constraint on the Neutron Star Equation of State from Multimessenger Observations. *Astrophys. J. Lett.*, 852(2):L29, January 2018.

[219] Adriana R. Raduta. Equations of state for hot neutron stars-II. The role of exotic particle degrees of freedom. *Eur. Phys. J. A*, 58(6):115, 2022.

[220] Adriana R. Raduta, Flavia Nacu, and Micaela Oertel. Equations of state for hot neutron stars. *Eur. Phys. J. A*, 57(12):329, December 2021.

[221] R. Rapp and J. Wambach. Equation of state of an interacting pion gas with realistic π-π interactions. *Phys. Rev. C*, 53(6):3057–3068, 1996.

[222] Luciano Rezzolla, Elias R. Most, and Lukas R. Weih. Using Gravitational-wave Observations and Quasi-universal Relations to Constrain the Maximum Mass of Neutron Stars. *Astrophys. J. Lett.*, 852(2):L25, January 2018.

[223] Luciano Rezzolla and Kentaro Takami. Gravitational-wave signal from binary neutron stars: A systematic analysis of the spectral properties. *Phys. Rev. D*, 93(12):124051, 2016.

[224] Sherwood Richers, Daniel Kasen, Evan O'Connor, Rodrigo Fernández, and Christian D. Ott. Monte Carlo Neutrino Transport through Remnant Disks from Neutron Star Mergers. *Astrophys. J.*, 813(1):38, November 2015.

[225] T. E. Riley, A. L. Watts, S. Bogdanov, P. S. Ray, R. M. Ludlam, S. Guillot, Z. Arzoumanian, C. L. Baker, A. V. Bilous, D. Chakrabarty, K. C. Gendreau, A. K. Harding, W. C. G. Ho, J. M. Lattimer, S. M. Morsink, and

T. E. Strohmayer. A NICER View of PSR J0030+0451: Millisecond Pulsar Parameter Estimation. *Astrophys. J. Lett.*, 887(1):L21, December 2019.

[226] Roger W. Romani, D. Kandel, Alexei V. Filippenko, Thomas G. Brink, and WeiKang Zheng. PSR J1810+1744: Companion Darkening and a Precise High Neutron Star Mass. *Astrophys. J. Lett.*, 908(2):L46, February 2021.

[227] Roger W. Romani, D. Kandel, Alexei V. Filippenko, Thomas G. Brink, and WeiKang Zheng. PSR J0952-0607: The Fastest and Heaviest Known Galactic Neutron Star. *Astrophys. J. Lett.*, 934(2):L17, August 2022.

[228] S. Rosswog. The dynamic ejecta of compact object mergers and eccentric collisions. *Philosophical Transactions of the Royal Society of London Series A*, 371(1992):20120272–20120272, April 2013.

[229] S. Rosswog and M. Liebendörfer. High-resolution calculations of merging neutron stars - II. Neutrino emission. *Mon. Not. R. Astron. Soc.*, 342(3):673–689, 2003.

[230] S. Rosswog, M. Liebendörfer, F. K. Thielemann, M. B. Davies, W. Benz, and T. Piran. Mass ejection in neutron star mergers. , 341:499–526, January 1999.

[231] S. Rosswog, T. Piran, and E. Nakar. The multimessenger picture of compact object encounters: binary mergers versus dynamical collisions. *Mon. Not. R. Astron. Soc.*, 430(4):2585–2604, April 2013.

[232] Stephan Rosswog. Astrophysical smooth particle hydrodynamics. , 53(4-6):78–104, April 2009.

[233] Stephan Rosswog. Conservative, special-relativistic smoothed particle hydrodynamics. *Journal of Computational Physics*, 229(22):8591–8612, 2010.

[234] Stephan Rosswog and Oleg Korobkin. Heavy elements and electromagnetic transients from neutron star mergers. *Annalen der Physik*, n/a(n/a):2200306.

[235] Stephan Rosswog, Enrico Ramirez-Ruiz, and Melvyn B. Davies. High-resolution calculations of merging neutron stars - III. Gamma-ray bursts. *Mon. Not. R. Astron. Soc.*, 345(4):1077–1090, November 2003.

[236] M. Ruffert, H. T. Janka, and G. Schaefer. Coalescing neutron stars - a step towards physical models. I. Hydrodynamic evolution and gravitational-wave emission. , 311:532–566, 1996.

[237] M. Ruffert, H. T. Janka, K. Takahashi, and G. Schaefer. Coalescing neutron stars - a step towards physical models. II. Neutrino emission, neutron tori, and gamma-ray bursts. , 319:122–153, March 1997.

[238] M. Ruffert and H. Th. Janka. Gamma-ray bursts from accreting black holes in neutron star mergers. , 344:573–606, April 1999.

[239] M. Ruffert and H. Th. Janka. Coalescing neutron stars - A step towards physical models. III. Improved numerics and different neutron star masses and spins. , 380:544–577, December 2001.

[240] Milton Ruiz, Stuart L. Shapiro, and Antonios Tsokaros. Gw170817, general relativistic magnetohydrodynamic simulations, and the neutron star maximum mass. *Phys. Rev. D*, 97:021501, Jan 2018.

[241] V. Savchenko et al. INTEGRAL Detection of the First Prompt Gamma-Ray Signal Coincident with the Gravitational-wave Event GW170817. *Astrophys. J. Lett.*, 848(2):L15, October 2017.

[242] R. F. Sawyer. Condensed π^- Phase in Neutron-Star Matter. *Phys. Rev. Lett.*, 29(6):382–385, August 1972.

[243] A. S. Schneider, C. Constantinou, B. Muccioli, and M. Prakash. Akmal-Pandharipande-Ravenhall equation of state for simulations of supernovae, neutron stars, and binary mergers. *Phys. Rev. C*, 100(2):025803, August 2019.

[244] Yuichiro Sekiguchi, Kenta Kiuchi, Koutarou Kyutoku, and Masaru Shibata. Effects of hyperons in binary neutron star mergers. *Phys. Rev. Lett.*, 107:211101, Nov 2011.

[245] Yuichiro Sekiguchi, Kenta Kiuchi, Koutarou Kyutoku, and Masaru Shibata. Gravitational waves and neutrino emission from the merger of binary neutron stars. *Phys. Rev. Lett.*, 107:051102, Jul 2011.

[246] Yuichiro Sekiguchi, Kenta Kiuchi, Koutarou Kyutoku, and Masaru Shibata. Current status of numerical-relativity simulations in Kyoto. *Progress of Theoretical and Experimental Physics*, 2012(1):01A304, October 2012.

[247] Yuichiro Sekiguchi, Kenta Kiuchi, Koutarou Kyutoku, and Masaru Shibata. Dynamical mass ejection from binary neutron star mergers: Radiation-hydrodynamics study in general relativity. *Phys. Rev. D*, 91(6):064059, March 2015.

[248] Yuichiro Sekiguchi, Kenta Kiuchi, Koutarou Kyutoku, Masaru Shibata, and Keisuke Taniguchi. Dynamical mass ejection from the merger of asymmetric binary neutron stars: Radiation-hydrodynamics study in general relativity. *Phys. Rev. D*, 93:124046, Jun 2016.

[249] Yuichiro Sekiguchi, Kenta Kiuchi, Koutarou Kyutoku, Masaru Shibata, and Keisuke Taniguchi. Dynamical mass ejection from the merger of asymmetric binary neutron stars: Radiation-hydrodynamics study in general relativity. *Phys. Rev. D*, 93(12):124046, 2016.

[250] Peter Senger. Probing Dense Nuclear Matter in the Laboratory: Experiments at FAIR and NICA. *Universe*, 7(6):171, 2021.

[251] Masaru Shibata, Sho Fujibayashi, Kenta Hotokezaka, Kenta Kiuchi, Koutarou Kyutoku, Yuichiro Sekiguchi, and Masaomi Tanaka. Modeling gw170817 based on numerical relativity and its implications. *Phys. Rev. D*, 96:123012, Dec 2017.

[252] Masaru Shibata and Kenta Hotokezaka. Merger and Mass Ejection of Neutron Star Binaries. *Annu. Rev. Nucl. Part. Sci.*, 69:41–64, October 2019.

[253] Masaru Shibata, Kenta Kiuchi, Yu-ichiro Sekiguchi, and Yudai Suwa. Truncated Moment Formalism for Radiation Hydrodynamics in Numerical Relativity. *Progress of Theoretical Physics*, 125(6):1255–1287, 06 2011.

[254] Luke J. Shingles, Christine E. Collins, Vimal Vijayan, Andreas Flörs, Oliver Just, Gerrit Leck, Zewei Xiong, Andreas Bauswein, Gabriel Martínez-Pinedo, and Stuart A. Sim. Self-consistent 3D Radiative Transfer for Kilonovae: Directional Spectra from Merger Simulations. *Astrophys. J. Lett.*, 954(2):L41, September 2023.

[255] Daniel M. Siegel. GW170817 -the first observed neutron star merger and its kilonova: Implications for the astrophysical site of the r-process. *European Physical Journal A*, 55(11):203, November 2019.

[256] Daniel M. Siegel and Brian D. Metzger. Three-dimensional GRMHD Simulations of Neutrino-cooled Accretion Disks from Neutron Star Mergers. *Astrophys. J.*, 858(1):52, May 2018.

[257] M. Aaron Skinner, Joshua C. Dolence, Adam Burrows, David Radice, and David Vartanyan. FORNAX: A Flexible Code for Multiphysics Astrophysical Simulations. *Astrophys. J. Suppl.*, 241(1):7, March 2019.

[258] S. J. Smartt et al. A kilonova as the electromagnetic counterpart to a gravitational-wave source. , 551(7678):75–79, November 2017.

[259] J. M. Smit, J. Cernohorsky, and C. P. Dullemond. Hyperbolicity and critical points in two-moment approximate radiative transfer. , 325:203–211, September 1997.

[260] C. Sneden, J. J. Cowan, and R. Gallino. Neutron-capture elements in the early galaxy. , 46:241–288, September 2008.

[261] M. Soares-Santos et al. The Electromagnetic Counterpart of the Binary Neutron Star Merger LIGO/Virgo GW170817. I. Discovery of the Optical Counterpart Using the Dark Energy Camera. *Astrophys. J. Lett.*, 848(2):L16, October 2017.

[262] A. W. Steiner, M. Hempel, and T. Fischer. Core-collapse Supernova Equations of State Based on Neutron Star Observations. *Astrophys. J.*, 774:17, September 2013.

[263] K. Takahashi, M. F. El Eid, and W. Hillebrandt. Beta transition rates in hot and dense matter. , 67(2):185–197, 1978.

[264] Kentaro Takami, Luciano Rezzolla, and Luca Baiotti. Spectral properties of the post-merger gravitational-wave signal from binary neutron stars. *Phys. Rev. D*, 91(6):064001, March 2015.

[265] Masaomi Tanaka et al. Kilonova from post-merger ejecta as an optical and near-Infrared counterpart of GW170817. , 69(6):102, December 2017.

[266] Masaomi Tanaka and Kenta Hotokezaka. Radiative Transfer Simulations of Neutron Star Merger Ejecta. *Astrophys. J.*, 775(2):113, October 2013.

[267] N. R. Tanvir, A. J. Levan, C. González-Fernández, O. Korobkin, I. Mandel, S. Rosswog, et al. The Emergence of a Lanthanide-rich Kilonova Following the Merger of Two Neutron Stars. *Astrophys. J. Lett.*, 848(2):L27, October 2017.

[268] K. S. Thorne. Relativistic radiative transfer - Moment formalisms. *Mon. Not. R. Astron. Soc.*, 194:439–473, February 1981.

[269] Richard C. Tolman. Static solutions of einstein's field equations for spheres of fluid. *Phys. Rev.*, 55:364–373, Feb 1939.

[270] Richard C. Tolman. Static Solutions of Einstein's Field Equations for Spheres of Fluid. *Phys. Rev.*, 55(4):364–373, February 1939.

[271] Samuel D. Tootle, L. Jens Papenfort, Elias R. Most, and Luciano Rezzolla. Quasi-universal Behavior of the Threshold Mass in Unequal-mass, Spinning Binary Neutron Star Mergers. *Astrophys. J. Lett.*, 922(1):L19, November 2021.

[272] Ralf-Arno Tripolt, Christopher Jung, Lorenz von Smekal, and Jochen Wambach. Vector and axial-vector mesons in nuclear matter. *Phys. Rev. D*, 104(5):054005, September 2021.

[273] E. Troja et al. The X-ray counterpart to the gravitational-wave event GW170817. , 551(7678):71–74, November 2017.

[274] Ka Wa Tsang, Tim Dietrich, and Chris Van Den Broeck. Modeling the postmerger gravitational wave signal and extracting binary properties from future binary neutron star detections. *Phys. Rev. D*, 100(4):044047, August 2019.

[275] S. Typel. Relativistic model for nuclear matter and atomic nuclei with momentum-dependent self-energies. *Phys. Rev. C*, 71(6):064301, 2005.

[276] S. Typel, G. Röpke, T. Klähn, D. Blaschke, and H. H. Wolter. Composition and thermodynamics of nuclear matter with light clusters. *Phys. Rev. C*, 81(1):015803, January 2010.

[277] Vimal Vijayan, Andreas Bauswein, and Gabriel Martinez-Pinedo. Neutrinos and their impact on the nucleosynthesis in binary neutron star mergers. *PoS*, FAIRness2022:061, 2023.

[278] Vimal Vijayan, Ninoy Rahman, Andreas Bauswein, Gabriel Martínez-Pinedo, and Ignacio L. Arbina. Impact of pions on binary neutron star mergers. *Phys. Rev. D*, 108:023020, Jul 2023.

[279] V. A. Villar, J. Guillochon, E. Berger, B. D. Metzger, P. S. Cowperthwaite, M. Nicholl, K. D. Alexander, P. K. Blanchard, R. Chornock, T. Eftekhari, W. Fong, R. Margutti, and P. K. G. Williams. The Combined Ultraviolet, Optical, and Near-infrared Light Curves of the Kilonova Associated with the Binary Neutron Star Merger GW170817: Unified Data Set, Analytic Models, and Physical Implications. *Astrophys. J. Lett.*, 851(1):L21, December 2017.

[280] Stamatis Vretinaris, Nikolaos Stergioulas, and Andreas Bauswein. Empirical relations for gravitational-wave asteroseismology of binary neutron star mergers. *Phys. Rev. D*, 101:084039, Apr 2020.

[281] Shinya Wanajo, Yuichiro Sekiguchi, Nobuya Nishimura, Kenta Kiuchi, Koutarou Kyutoku, and Masaru Shibata. Production of All the r-process Nuclides in the Dynamical Ejecta of Neutron Star Mergers. *Astrophys. J. Lett.*, 789(2):L39, 2014.

[282] Darach Watson, Camilla J. Hansen, Jonatan Selsing, Andreas Koch, Daniele B. Malesani, Anja C. Andersen, Johan P. U. Fynbo, Almudena Arcones, Andreas Bauswein, Stefano Covino, Aniello Grado, Kasper E. Heintz, Leslie Hunt, Chryssa Kouveliotou, Giorgos Leloudas, Andrew J. Levan, Paolo Mazzali, and Elena Pian. Identification of strontium in the merger of two neutron stars. , 574(7779):497–500, October 2019.

[283] Eli Waxman, Eran O. Ofek, Doron Kushnir, and Avishay Gal-Yam. Constraints on the ejecta of the GW170817 neutron star merger from its electromagnetic emission. *Mon. Not. R. Astron. Soc.*, 481(3):3423–3441, December 2018.

[284] K. Way and E. P. Wigner. The rate of decay of fission products. *Phys. Rev.*, 73:1318–1330, Jun 1948.

[285] W. Weise and G. E. Brown. Equation of state for neutron matter in the presence of a pion condensate. *Physics Letters B*, 58(3):300–303, September 1975.

[286] J. R. Wilson, G. J. Mathews, and P. Marronetti. Relativistic numerical model for close neutron-star binaries. *Phys. Rev. D*, 54(2):1317–1331, July 1996.

[287] James R. Wilson, R. Couch, S. Cochran, J. Le Blanc, and Z. Barkat. Neutrino flow and the collapse of stellar coresfn1. *Annals of the New York Academy of Sciences*, 262(1):54–64, 1975.

[288] Francesco Zappa, Sebastiano Bernuzzi, David Radice, Albino Perego, and Tim Dietrich. Gravitational-wave luminosity of binary neutron stars mergers. *Phys. Rev. Lett.*, 120:111101, Mar 2018.